

AIAA 2021 Undergraduate Team Aircraft Design Competition

Light Attack Aircraft – Spyro

Final Design Report

Team Dragon



Jiayi Guo, Ryan Hansen, Daniel Jacobson, Ari Jain, Alan Rice, Ian Salamon, Wanzheng Zheng

Faculty Advisor: Dr. Jason Merret

University of Illinois at Urbana-Champaign

Aerospace Engineering 443: Aerospace Systems Engineering II

April 29, 2021

Team Dragon



Arihant Jain
Team Lead
Systems
Certification
593587



Jason Merret
Faculty Advisor
155270



Ryan Hansen
Propulsion
Stability/Control
Acoustics
1180317



Daniel Jacobson
Performance
Configuration
Ordnance
1229735



Wanzheng Zheng
Loads &
Dynamics
Landing Gear
1230799



Alan Rice
Structures
Interior
905446



Jiayi Guo
Mass Properties
Cost
1180025



Ian Salamon
Aerodynamics
Avionics
1230795

Executive Summary

This report presents Spyro, a CAS aircraft designed in response to the AIAA 2021 Undergraduate Team Aircraft Design RFP. Spyro satisfies all requirements given by the RFP [1]. Primary constraints concern the completion of a design and ferry mission, which have range requirements of approximately 300 and 1,000 nautical miles respectively. Further, the aircraft must be capable of takeoff and landing at altitudes of up to 6,000 feet, in under 4,000 feet of austere field runway. A 3,000 lb payload requirement with an integrated gun, and zero-zero injection seats are also outlined.

Existing aircraft that fit this role include the Embraer Super Tucano, Fairchild Republic A-10 Thunderbolt, the Aero L-159 ALCA, etc. The Spyro aims to take redeeming qualities of current aircraft and develop a more efficient and affordable vehicle. The presented design features a low-wing, single engine turbofan configuration with a maximum takeoff weight of 13,362 pounds. A balanced field length of 3,836 feet and service ceiling of 30,646 feet exceed the RFP requirements. Further, the design includes a M-61A Vulcan integrated gun and Martin Baker Mk16 ejection seats. Both the design and ferry mission are readily satisfied and the aircraft has a unit cost of \$25.2 million.

List of Acronyms and Initialisms

Name	Definition
AIAA	American Institute of Aeronautics and Astronautics
AR	Aspect Ratio
CAD	Computer-Aided Design
CAS	Close Air Support
CBR	California Bearing Ratio
ECS	Environmental Control System
ECU	Engine Control Unit
EEC	Electronic Engine Controller
EICAS	Engine Indicated and Crew Alerting System
EMEDS	Electro-Mechanical Expulsion Deicing
EWIS	Electrical Wiring Interconnect System
EW	Empty Weight
FADEC	Full Authority Digital Engine Control
FAR	Federal Acquisition Regulation
FEA	Finite Element Analysis
FLIR	Foreword Looking Infrared
FWB	Fly-by-wire
GPS	Global Positioning System
GPU	Ground Power Unit
IRSS	Infrared Suppression System
LAAR	Light Attack/Armed Reconnaissance
LE	Leading Edge
LFL	Landing Field Length
LTG	Laser Target Designator
MAC	Mean Aerodynamic Chord
MFD	Multi-function display
MTOW	Maximum Takeoff Weight
NASA	National Aeronautics and Space Administration
NH	Rotary Shaft Speed
OBOGS	On-board Oxygen Generation System
PW	Payload Weight
RFP	Request for Proposal
RHAG	Rotary Hydraulic Arrestor Gear
ROC	Rate of Climb
SFC	Specific Fuel Consumption
TA	Thrust Available
TFL	Take-off Field Length
TGT	Turbin Gas Temperature

List of Acronyms and Initialisms

Name	Definition
TSFC	Thrust Specific Fuel Consumption
UHF	Ultra High Frequency
VHF	Very High Frequency
VLM	Vortex Lattice Method
WAAS	Wide Area Augmentation System

Nomenclature

Name	Definition
b	Span
c_{root}	Root Chord
c_{tip}	Tip Chord
C_D	Airplane Drag
C_{D_0}	Drag at Zero Lift
C_L	Airplane Lift
$C_{L_{\max}}$	Maximum Lift
$C_{L_{\alpha}}$	Lift Curve Slope
C_{l_r}	Roll Derivative w.r.t. r
$C_{l_{\beta}}$	Roll Derivative w.r.t. β
C_{n_r}	Yaw Derivative w.r.t. r
$C_{n_{\beta}}$	Yaw Derivative w.r.t. β
$C_{M_{\alpha}}$	Pitching Moment Derivative w.r.t. α
$C_{M_{\delta_e}}$	Pitching Moment Sensitivity to δ_e
r	yaw rate
S	Area
S_H/S_W	Tail Surface Coefficient
S_{ref}	Wing area
T_2	Doubling Time
V_{LOF}	Lift off velocity
V_{stall}	Stall speed
V_R	Rotation speed
α	Angle of Attack
β	Sideslip Angle
δ_e	Elevator Deflection Angle
δ_r	Rudder Deflection Angle
ϵ_{α}	Downwash Angle Derivative
ζ	Damping Coefficient
$\Lambda_{c/4}$	Quarter-Chord Sweep
μ_g	Rolling Ground Coefficient
μ_B	Braking Ground Coefficient
τ_r	Roll Time Constant
ω_n	Natural Frequency

Contents

I	Introduction	1
II	Concept of Operations	2
II.A	Overview	2
II.B	Mission Profiles	2
III	Sizing Analysis	4
III.A	Similarity Analysis	4
III.B	Constraint Diagram	5
III.C	Trade Studies	6
IV	Configuration	8
IV.A	Design Morphology	8
IV.A.1	Fuselage	9
IV.A.2	Multi-View Drawing	9
IV.B	Landing Gear	10
IV.C	Interior	13
IV.C.1	Cockpit Viewing Angles	14
V	Propulsion	14
V.A	Engine Type Selection	14
V.B	Number of Engines & Engine Location	16
V.C	Engine Selection	16
V.D	Engine Performance & Operation	17
V.E	Inlet and Exhaust Design	19
V.F	Propulsion & Fuel System	20
VI	Aerodynamics	21
VI.A	Desired Characteristics	21
VI.B	Airfoil Selection	21
VI.C	Wing Design	23
VI.D	Drag Buildup	24
VI.E	Aerodynamic Data	25
VI.F	High Lift System	27
VI.G	Computational Fluid Dynamics	29
VII	Performance	29
VII.A	Performance Requirements	29
VII.B	Takeoff Performance	30
VII.C	Landing Performance	31
VII.D	Performance Coefficients	32
VII.E	Service and Absolute Ceiling	33
VII.F	Specific Excess Power	33
VII.G	Flight Envelope	34
VII.H	Drag For Each Segment	35
VII.I	Payload Investigation	36
VII.J	Fuel Requirements	38
VII.J.1	Ferry Mission	38
VII.J.2	Design Mission	38
VII.K	Trade Studies	39
VII.K.1	Optimizing Cruise Altitude and Velocity for Fuel Burn	39
VII.K.2	Rate of Climb Analysis	41

VIII Stability and Control	42
VIII.A Stabilizer Design	42
VIII.B Control Surfaces	44
VIII.C Trim Analysis	45
VIII.D Longitudinal Static Stability	46
VIII.E Lateral-Directional Static Stability	46
VIII.F Stick-Free Stability	47
VIII.G Dynamic Stability	47
IX Structures and Loads	48
IX.A Aircraft Loads Analysis	48
IX.A.1 V-n Diagram	48
IX.A.2 Maneuverability and Load	50
IX.A.3 Load Cases and Load Paths	52
IX.B Structural Arrangement	54
IX.C Material Selection	55
IX.D Structural Component Sizing	57
IX.D.1 Wing	57
IX.D.2 Empennage	60
IX.D.3 Fuselage Forces	61
IX.E Wing Internal Structure	62
IX.F Finite Element Analysis	63
IX.G Pressurization Loads	65
X Mass Properties	66
X.A Weights	66
X.B Center of Gravity and Balance	67
XI Auxiliary Systems	70
XI.A Flight Controls	70
XI.B Engine Controls	70
XI.C Fuel System (RH)	71
XI.D Hydraulic System	72
XI.E Electric System	73
XI.F Pneumatic and Environmental Control System	74
XI.G Emergency Systems	75
XI.H Systems Integration and Inboard Profile	76
XI.I Avionics	77
XII Ordnance	78
XII.A Desired Characteristics	78
XII.B Ordnance Selection	79
XII.C Gun Selection	80
XII.D Ordnance Load Out	81
XII.E Safety Considerations	82
XIII Acoustics, Observability, Emissions	82
XIII.A Survivability Aspects	82
XIII.B Acoustics & Emissions	84
XIV Cost Analysis	84
XIV.A Life Cycle Cost Estimation	84
XIV.B Cost Savings	87
XV Conclusion	88

List of Figures

1	Spyro	2
2	Design mission	3
3	Ferry mission	3
4	Constraint diagram	6
5	Empty Weight vs AR and S_{ref}	7
6	Fuel Weight vs AR and S_{ref}	7
7	Single engine high wing consideration	9
8	Single engine low wing consideration	9
9	Twin engine high wing consideration	9
10	Twin engine low engine consideration	9
11	Clearance with Landing Gear Placement	10
12	Three-view Drawing of Spyro	11
13	Passes on Airfield with CBR = 5 versus Tire Pressure	12
14	Nose Landing Gear, Extended	13
15	Nose Landing Gear, Retracted	13
16	Main Landing Gear, Retracted	13
17	Main Landing Gear, Extended	13
18	Forward-Looking Viewing Angles	14
19	Right-Looking Viewing Angles	14
20	Full Throttle TSFC vs. Mach vs. Altitude	18
21	Full Throttle TSFC vs. TA vs. Altitude	18
22	Engine Throttle & Applied Thrust Throughout Each Mission	19
23	NX Rendering of Y-Duct Inlet	20
24	Airfoil Lift Curves	22
25	Modified NASA Medium Speed Airfoil at Root	23
26	Major Wing Dimensions	23
27	C_L vs Alpha of Plane at Cruise	25
28	CFX simulated Flow at Stall	26
29	C_L vs C_D of Plane at Cruise	27
30	Flap Cutaway at Root	28
31	Simulated High Lift Curves	28
32	Fan Face	29
33	Inlet Face	29
34	Coefficients for Ferry Optimization	32
35	Coefficients for Design Mission Optimization	32
36	Specific Excess Power Diagram	34
37	Flight Envelope at MTOW	35
38	Payload vs Range Diagram	37
39	Payload vs Time On Station	37
40	Fuel Requirement with Time for Ferry Mission	38
41	Fuel Requirement with Time for Design Mission	39
42	Optimization of Cruise Conditions	40
43	Range vs. Mach Curve	41
44	Scissor Plot	43
45	Horizontal Stabilizer Diagram	44
46	Vertical Stabilizer Diagram	44
47	Trim Diagram for Landing	45
48	Trim Diagram for Takeoff	45
49	Trim Diagram for Cruise	45
50	Combined Military and FAR-25 V-N Diagram at Fight Design Gross Weight	49
51	Combined Military and FAR-25 V-N Diagram at Maximum Design Gross Weight	50
52	Energy Maneuverability of Spyro, Aero-L39, and EMB-314	51

53	Energy Maneuverability of Spyro at MTOW, Loiter Condition	51
54	Load Paths of Aircraft in Static Condition	52
55	Block Diagram of Load Transfer	53
56	Problem Setup of Investigation of Stress Concentration Along Fuselage	54
57	Stress Concentration Along Fuselage	54
58	View of the internal structures of Spyro, with skin transparency	55
59	Visualization of the calculated lift distribution at maximum total load	58
60	Lift-per-unit-span along the wing	58
61	Shear forces inside the wing structure	59
62	Bending moments inside the wing structure	59
63	Horizontal tail downloading in a max-load turn	61
64	Equilibrium 120°/s Roll-rate	61
65	Equilibrium roll with reversed controls	61
66	Wing Spar Locations	62
67	Innermost Rib Outline with Tank Cutouts	63
68	Detailed Wing Structural Arrangement	63
69	Load Case used in the stress analysis	64
70	Stress developed in the structure [psi]	64
71	Maximum Vertical Wingtip Displacement [in]	65
72	Wing Placed at 17.35 ft	67
73	Wing Placed at 17.75 ft	67
74	Wing Placed at 17.55 ft	67
75	Longitudinal CG Travel	68
76	Lateral CG Travel	69
77	Fuel Weight and CG Travel During Mission	69
78	Engine Control Architecture	71
79	Fuel System Block Diagram	72
80	Hydraulic System Architecture	73
81	EMEDS system	74
82	Pneumatic and ECS architecture	75
83	Inboard profile	76
84	Avionics Layout	77
85	Cockpit Layout	78
86	Ordnance Load Out Chart	81
87	Figures for Choosing a Paint for Spyro	83
88	Armor Plate Locations	84
89	LCC Break Down	87
90	Cost per Unit Flight Hour [USD]	87

List of Tables

1	General requirements	3
2	Mission outline by segment	4
3	Similarity Data	5
4	Key parameters based on sizing	7
5	Notable Configuration Parameters	10
6	Landing Gear Sizing and Positioning Summary	13
7	Comparison of Different Turbine Engine Types	15
8	Engine Type Selection Figures of Merit	16
9	Trade Study of Different Engines	17
10	Airfoil Similarity Data	21
11	Wing Geometry Tabulated	23
12	Drag Buildup	24
13	Aerodynamic Parameters During Mission	26

14	Similar Aircraft High Lift Devices	27
15	Takeoff Distance at Different Friction Coefficients	30
16	Takeoff Length by Individual Segment	31
17	Landing Length by Individual Segment	31
18	Performance Coefficients Tabulated	32
19	Drag Buildup for Individual Segments	36
20	Various Aircraft and Rate of Climb	41
21	Trade Study on Tail Airfoil Selection	42
22	Horizontal and Vertical Tail Parameters	44
23	Control Surface Parameters	45
24	Longitudinal Stability Control Derivatives	46
25	Center of Gravity, Neutral Point, and Static Margin	46
26	Lateral-Directional Stability Control Derivatives	47
27	Hinge Moments	47
28	Rudder Trim	48
29	Longitudinal Dynamic Stability Analysis	48
30	Lateral-Directional Dynamic Stability Analysis	48
31	List of Aluminum Alloys Considered	56
32	Metal Selection Figures of Merit	56
33	Material Selection Figures of Merit	57
34	Weight Breakdown	66
35	Ordnance Trade Study	79
36	Gun Selection	80
37	Material Properties of Armor	84
38	Research Test Development Engineering Cost	85
39	RFP Requirement Summary	88

I. Introduction

Close air support (CAS) is defined in the military as air action against hostile targets that are in close proximity and contact with friendly forces, which therefore requires a coordinated integration between air and friendly ground forces [2]. In 2009, the United States launched the Light Attack/Armed Reconnaissance (LAAR) program to develop a CAS aircraft that would suit combat after the 2003 invasions of Iraq and Afghanistan. Unfortunately, the Light Attack/Armed Reconnaissance program was effectively canceled by the Pentagon in 2020 despite U.S. Special Operations Command leadership testifying to the need of further exploration of such a program [3–5]. The requirements outlined by the 2021 AIAA light attack aircraft RFP [1] align closely to the original request for information of the LAAR program [1]. As such, target markets for this aircraft include armed forces of various nations including the United States, United Kingdom, etc.

The AIAA RFP [1] gives specific requirements that the aircraft must satisfy that are described in detail in Section II. Key requirements include a 3,000 lb payload with integrated gun, zero-zero ejection seats for two crew, and provisions for carrying a variety of ordnance. Further, the aircraft must satisfy a design and ferry mission with ranges of 300 and 1,000 nmi respectively, while also being capable of takeoff and landing in austere fields in under 4,000 feet. Similar aircraft that have been developed for this role include the Embraer EMB 314 Super Tucano, Beechcraft T-6 Texan II, and A-10 Thunderbolt. The presented aircraft - Spyro - aims to take redeeming qualities of the existing aircraft, improve upon them, and present a more affordable and efficient design that appeals to the target market while satisfying and exceeding the prescribed requirements.

Indeed, Spyro does satisfy or exceed all requirements given by the RFP [1]. The presented design features a low-wing, single engine turbofan configuration with a maximum takeoff weight of 13,362 pounds. A balanced field length of 3,939 feet ($\mu_g = 0.1$) and service ceiling of 30,646 feet exceed the RFP requirements. Further, the design includes a M-61A Vulcan integrated gun and Martin Baker Mk16 ejection seats. The vehicle has a unit cost of \$26.5 million, and an operating cost that is highly competitive with existing aircraft in its class (Section XIV). The engine chosen for Spyro is the Honeywell TFE731-40, which provides a maximum of 4,250 lb of thrust that give desired performance characteristics. Finally, the aircraft has a length of 37 feet, height of 15.08 feet, wingspan of 36.9 feet, and wing area of 206.25 ft². An image of the design is given below.



Fig. 1 Spyro

II. Concept of Operations

A. Overview

A majority of driving design requirements are outlined by the AIAA RFP [1]. A required design mission and ferry mission are given. In addition, there are independent requirements and objectives listed in Table 1 that must be satisfied. Considerations taken outside of the explicit requirements include designing Spyro such that it can complete missions that helicopters are commonly used for. It will be assumed that the vehicle will enter service in 2025 and is certified according to military standards described in MIL-STD-516C (MILSPEC) [6]. All systems on the vehicle are at Technology Ready Level 8 or higher. Joint Service Specification Guides (JSSGs) and Federal Aviation Regulations (FARs) will also be taken into account when making design decisions.

B. Mission Profiles

The design mission must be carried out by the proposed vehicle with a full payload. It is described in Table 2 and visualized in Figure 2. The numbered segments on the Figure correspond to those listed in the Table. Further, segments 11.1, 11.2, and 11.3 are used to represent reserve mission climb, loiter, and descent respectively. There is no range that is explicitly given for the design mission. However, based on the segments that the RFP says should receive range credit, 300 nmi was approximated for calculations and is used as the standard throughout the report.

In addition to the design mission, Spyro must satisfy the requirements of the long-range ferry mission in Table 2 with full crew and 60% payload. Figure 3 visualizes the mission profile with segments 7.1, 7.2, and 7.3 representing reserve mission climb, loiter, and descent respectively. Similar to the design mission, climb and descent are given range credit but not explicitly assigned a numerical requirement. As such, it was assumed that a total ferry range of 1,000 nmi

should be achievable by Spyro. For any mission, the goal is for the pilots to be able to fly the outlined profile with zero to minimal mechanical difficulties, and return to base after having accomplished their objective. The RFP outlines a service life of 15,000 hours over 25 years [1].

Table 1 General requirements

Requirement	Description
Mandatory	Takeoff and landing over a 50 ft obstacle in \leq 4,000 ft when operating from austere fields at density altitude up to 6,000 ft with semi-prepared runways such as grass or dirt surfaces with California Bearing Ratio of 5
Mandatory	3,000 pounds of armament as payload
Mandatory	Integrated gun for ground target engagement
Mandatory	Zero-zero ejection seats for two crew
Mandatory	Service life of 15,000 hours over 25 years
Mandatory	Service ceiling of at least 30,000 feet
Objective/Goal	Provisions for carrying/deploying a variety of weapons, including rail-launched missiles, rockets, and 500 pound (maximum) bombs
Objective/Goal	Considerations for survivability, such as armor for the cockpit and engine, reduced infrared and visual signatures, and countermeasures

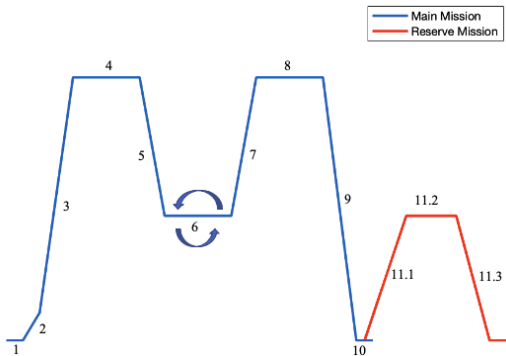


Fig. 2 Design mission

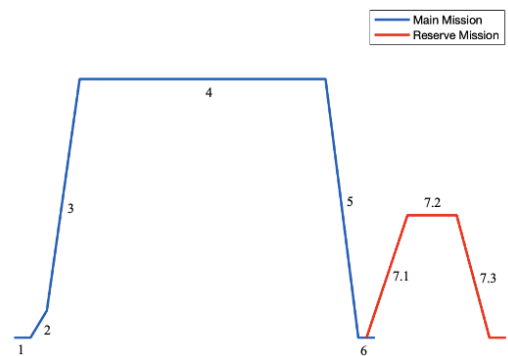


Fig. 3 Ferry mission

The nature of CAS and operating from an austere field implies that the aircraft may have to frequently maintained due to damage. Survivability considerations are taken into place by using armor around the cockpit and engine.

Redundancies are built into all systems to eliminate the risk of single point failures. Finally, parts and materials used for Spyro, such as the engine and aluminum alloys, are widely available. This will reduce acquisition costs for maintenance and also reduce training costs for maintenance crew. The overall goal for the aircraft is to minimize the need for maintenance in the first place. Further, the aim is to ensure that any maintenance that is necessary can occur as efficiently as possible with minimal time wasted on the ground.

Table 2 Mission outline by segment

Segment	Design Mission		Ferry Mission	
	Description	Considerations	Description	Considerations
1	Warm Up/Taxi	5 minutes	Warm Up/Taxi	5 minutes
2	Takeoff	Austere field, 50 feet obstacle, $\leq 4,000$ feet	Takeoff	Austere field, 50 feet obstacle, $\leq 4,000$ feet
3	Climb	To cruise altitude, $\geq 10,000$ feet, with range credit	Climb	To cruise altitude, $\geq 10,000$ feet, with range credit
4	Cruise	100 nautical miles	Cruise	At best range speed/altitude ($\geq 18,000$ ft), 900 nmi
5	Descent	To 3,000 feet, no range credit, completed within 20 minutes of initial climb	Descent/Landing	To austere field over 50 feet obstacle, $\leq 4,000$ feet
6	Loiter	On station, four hours, no stores dropped	Taxi/Shutdown	5 minutes
7	Climb	To cruise altitude, $\geq 10,000$ feet, with range credit	Reserve	Sufficient to climb to 3,000 feet and loiter for 45 mins
8	Cruise	100 nautical miles		
9	Descent/Landing	To austere field over 50 feet obstacle, $\leq 4,000$ feet		
10	Taxi/Shutdown	5 minutes		
11	Reserves	Sufficient to climb to 3,000 feet and loiter for 45 mins		

III. Sizing Analysis

A. Similarity Analysis

To begin sizing, a similarity analysis is conducted by gathering data on similar aircraft. The aircraft are divided into three categories based on their propulsion system: turboprop, turbojet, and turbofan. This broad variety of aircraft ensures that no matter which propulsion system is selected further on in the design process, there are comparable aircraft to build up from. Only the most relevant parameters are presented in Table 3, although far more additional data was gathered based on aircraft drawings and literature [7–9] such as horizontal and vertical tail areas, engine SFC, etc. Note that payload weight and ceiling data show how existing aircraft would compare to one designed as required by the RFP.

Individual aspects of the similarity analysis are taken into consideration during initial sizing outlined in the following section. Sizing itself is conducted with a spreadsheet where initial guesses are made for major weight variables - max takeoff, empty, and fuel - and calculations are conducted using theoretical, empirical, and semi-empirical formulas described throughout Raymer and Roskam [10, 11]. The calculations are then iterated until the various weights converge to within a desired tolerance. The overall process for this build up technique is given by Feagen and Morrison, Jr [12]. For any parameter that an equation was not available for, seed aircraft parameters were taken as inputs.

Table 3 Similarity Data

Variable	Turbojet			Turboprop			Turbofan		
	Cessna A-37	Saab 105	Sukhoi Su-25UB	Embraer EMB314	OV-10 Bronco	Pilatus PC-21	Aero L-39	FMA IA-63	CASA C-101
MTOW [lb]	14,000	14,330	40,785	11,905	14,444	9,370	13,227	11,023	13,890
EW [lb]	6,211	5,535	22,156	5,335	4,707	5,004	7,628	6,219	7,716
PW [lb]	1,600 ↓	4,409 ↑	8,818 ↑↑	3,307 ≈	4,000+ ↑	2,540 ↓	3,307 ↑	4,189 ↑	4,960 ↑↑
S_{ref} [ft 2]	183.9	175.5	323.99	208.8	291	163.84	202.4	168.2	220
b [ft]	35.8	31.17	47.11	36.58	40	29.93	31	31.75	34.75
Length [in]	339.25	425	611.5	414.57	528	442.44	477	430	492
Cruise Mach	0.64	0.76	0.77	0.37	0.32	0.53	0.7	0.8	0.75
Ceiling [ft]	41,765 ↑↑	44,900 ↑↑	23,000 ↓	35,000 ↑	30,000 ≈	37,990 ↑	36,000 ↑	42,300 ↑↑	42,000 ↑↑

B. Constraint Diagram

Per Chapter 3 of Raymer [10], wing loading and T/W are the defining parameters in the aircraft sizing process when assessing performance characteristics. Using equations in Chapter 5 and assuming takeoff at 6,000 ft with the RFP requirements, the constraint diagram shown in Figure 4 can be constructed. Note that the loiter line is the defining boundary of the valid design region. This is attributed to loiter occurring at 3,000 feet, allowing for higher thrust availability. It is also important to note the design point of Sypro, which is shown, is not necessarily at the lowest wing loading or highest T/W . Maneuverability was a key consideration when conducting sizing, however, RFP requirements and engine selection were the ultimate driving factor in the design point decision. The chosen engine, the TFE731-40 (Section V), needed a higher thrust to satisfy takeoff performance requirements (Section VII), which results in the design point shown on Figure 4.

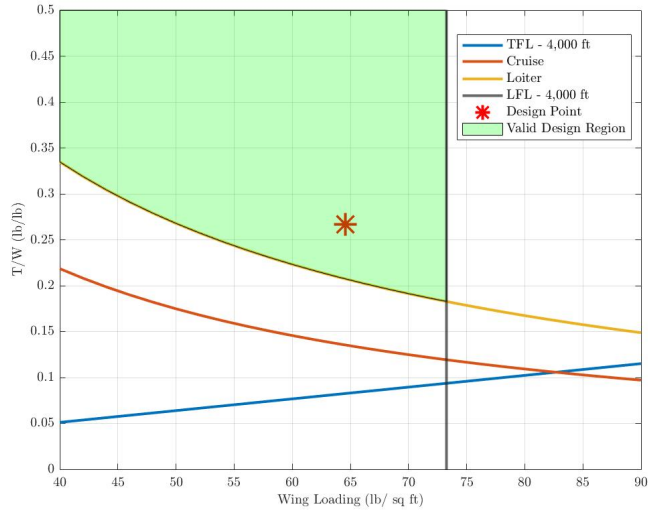


Fig. 4 Constraint diagram

C. Trade Studies

Two trade studies are conducted that study fuel weight and empty weight. Optimizing these variables reduce operating and manufacturing costs respectively. Wing aspect ratio and wing area were varied, and based on the iterative buildup method mentioned in the previous subsection, contour plots for the desired variables were constructed as shown in Figures 5 and 6. Design points chosen for Spyro are marked on the graph with red lines.

The plots confirm intuition and expected qualitative trends, as weight increases for larger wing areas. Similar to the constraint diagram, the chosen parameters for Spyro are not necessarily the lowest values shown on the graph. Restrictions on the plots show LFL and service ceiling, which reduce the viable valid design area to the bottom right areas of the plots. Wing area decisions were also driven by performance requirements, along with aerodynamics discussed in Section VI. After accounting for design and performance constraints, an aspect ratio of 6.5 and a wing area of 200 square feet was determined to be the optimal design point. A design margin of 15% also allows flexibility for future design decision and further pushes the shown design point further from the most optimal possible position. The sizing program also calculated other key aircraft design parameters that are summarized in Table 4 below. Note that these values are not necessarily those that are chosen for the final design. These are purely results from the sizing program that are evaluated in greater detail in subsequent sections. For example, the actual SFC of the propulsion system chosen may differ from that given directly below based on market availability.

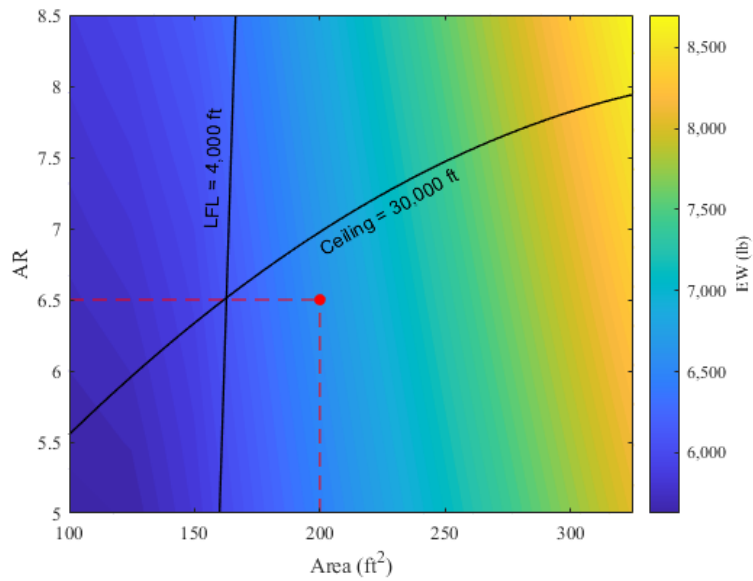


Fig. 5 Empty Weight vs AR and S_{ref}

Table 4 Key parameters based on sizing

Parameter	MTOW	Empty Weight	Fuel Weight	TSFC	L/D	$C_{L_{\max}}$	Take-off Thrust	Wing Loading
Value	13,182 lb	6,624 lb	3,558 lb	0.475 lb/lb/hr	11.92	1.6	3,291 lb	65.4 lb/ft ²

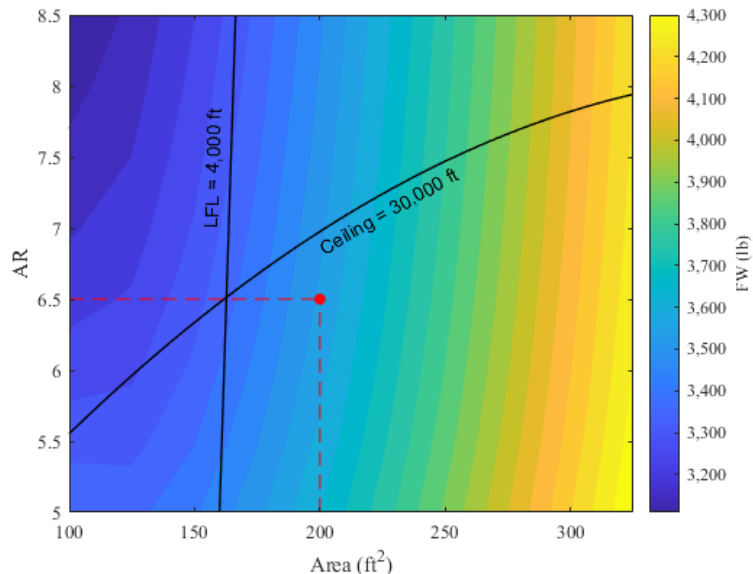


Fig. 6 Fuel Weight vs AR and S_{ref}

IV. Configuration

A. Design Morphology

During the preliminary stages of configuration, a qualitative analysis of different configurations were studied. These standard initial configurations are driven by the requirements in the RFP in terms of takeoff and landing - the demanding components of the design mission - and affordability. The initial trade studies investigate the engine number and engine placement. This decision along with the decision for high, mid, or low wing configuration were modeled in OpenVSP and further analyzed. The choice against a mid wing placement was due to the structure of the wing and similarity analysis. When selecting a wing that runs through the fuselage, such as a mid wing configuration, the wing box will force the attached locations to be reinforced structurally and thus add an increased amount of weight to the aircraft. Similarity analysis confirms this study of specifically low and high wing design due to the great amount of resources in contrast to mid wing. Therefore, high and low wing configurations are studied due to the great amount of successful seed aircraft.

The chosen configuration in Figure 6, bordered in black, represents the single engine, low wing design that was selected. The single engine will provide the aircraft with the necessary thrust while limiting excess empty weight from additional engines. This will also conserve area on the wing for ordnance and fuel tanks to be stored. The drawbacks to this will be the significant amount of space and weight that the turbofan engine will take up on the back end of the aircraft. This will require that the fuselage be widened to allow engine placement in the aft fuselage.

The low wing design was selected due to it providing the greatest amount of visibility to the pilot as well as allowing for high aerobatic performance [10]. For an aircraft like Spyro, the low wing design will provide the greatest amount of visibility during turns and maneuvers, which is desired for the RFP. A low wing design is additionally often chosen on high speed transport aircraft due to better cruise performance. Although this is a light attack aircraft design, the beneficial cruise performance is certainly welcome. Unlike the high wing and mid wing designs, the selected low wing design will produce a smaller profile drag and therefore burn less fuel during this stage. A low wing configuration also allows under wing stores to be more easily attached and removed. First among the drawbacks of selecting the low wing configuration for Spyro is reduced ground clearance. To counter, the wing will be given a 3 degree dihedral to provide the underwing stores 6 inches of clearance with the ground. The chosen wing placement will also vary the placement of the landing gear, which will be discussed in Section IV.B. The chosen configuration is validated by comparing to the similarity in Section III. Aircraft with the similar low wing, single turbofan engine configuration such as the Aero L-39 and CASA C-101 have successfully flown light attack missions since 1968 and 1977 respectively while having an average MTOW of 13,558 lb. This compares well to the preliminary sizing results for Spyro and will prove successful in satisfying the RFP requirements [1].

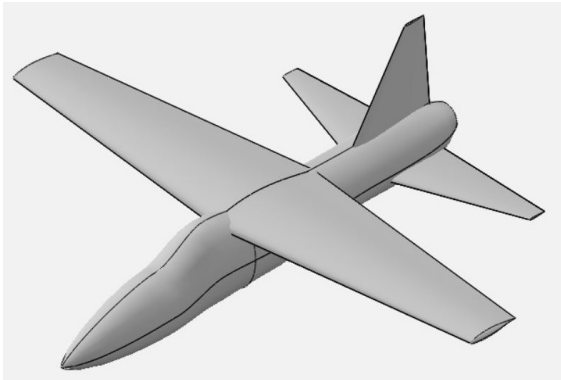


Fig. 7 Single engine high wing consideration

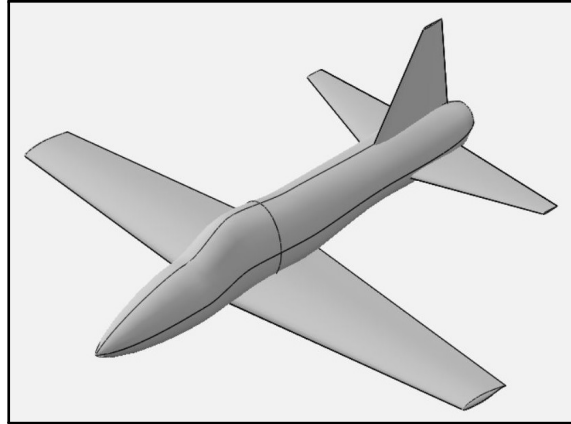


Fig. 8 Single engine low wing consideration

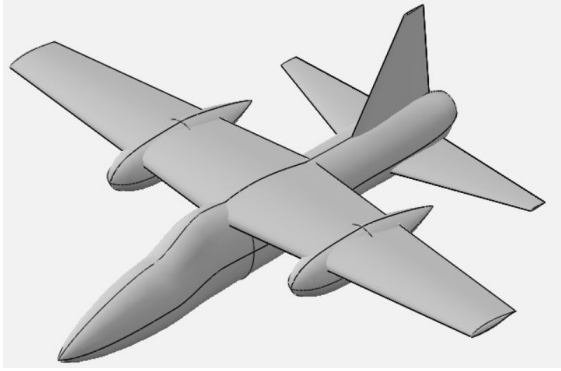


Fig. 9 Twin engine high wing consideration

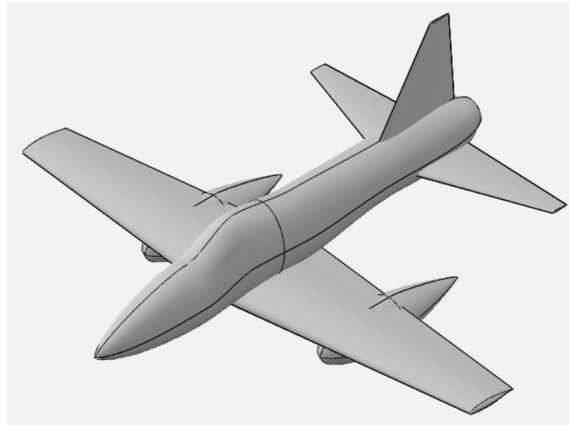


Fig. 10 Twin engine low engine consideration

1. Fuselage

The initial construction of the fuselage in OpenVSP followed a conic lofting process. It was then driven by the need for increased space for the engine and inlets on either side of the fuselage. Further revisions were made after analysis via CFD to smoothen out the fuselage skin so no discontinuities lie in the path of the fuselage externally. The fuselage is kept elliptical in cross sections to minimize the structural weight while remaining tightly wrapped around the cockpit to fit the systems needed. The fuselage as designed has a length of 37 ft and a maximum width of 4 ft. The width was chosen to allow structural room for the chosen engine at the tail end as well as fit the two crew members in the cockpit. The canopy and cockpit itself was modeled in order to maximize the visibility and comfort of the pilot.

2. Multi-View Drawing

The external layout configuration is laid out as shown in Figure 11. This gives the basic configuration of the aircraft regarding the major features of Spyro. The center of gravity and neutral point are also represented on the three view

drawing by red and blue dots respectively. More in-depth features such as the dimensions of the control surfaces on the wings are described in their individual sections like Section VI.C for wing features and Section VIII.A for stabilizer designs.

Table 5 Notable Configuration Parameters

C/4 Sweep	Taper Ratio	Wing Area	Wing MAC	Wetted Area	CG Postion	Neutral Point
0	0.45	206.25 ft ²	5.56 ft	876 ft ² Clean	34.1% MAC	47.5% MAC

B. Landing Gear

Considering the requirement for operation from austere runways, and the lightweight nature of the design, a tricycle landing gear configuration was chosen above other configurations due to its robustness in turning, large crab angle tolerance, good pilot visibility on the ground, desirable take-off and landing clearance, and kinematic stability on the ground. An estimated center of gravity of the design is located 20 ft after the nose, and will be discussed in detail in Section X.B. Landing gear length and main gear position with respect to center line can be simultaneously solved for following guidelines listed in Chapter 11 of Raymer [10]. Solving this system of equations while minimizing landing gear length would yield a height of 2 ft, while being 3.5ft outward from the center line and 1 ft aft of the center of gravity. Landing gear placement, as well as relative clearance for tricycle landing gears, are shown in Figure 11.

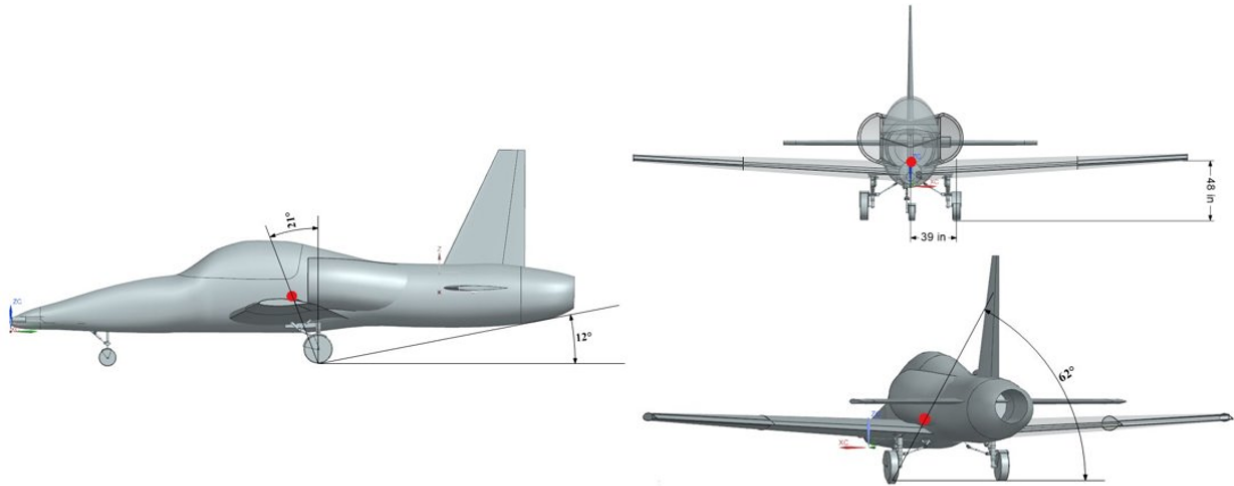


Fig. 11 Clearance with Landing Gear Placement

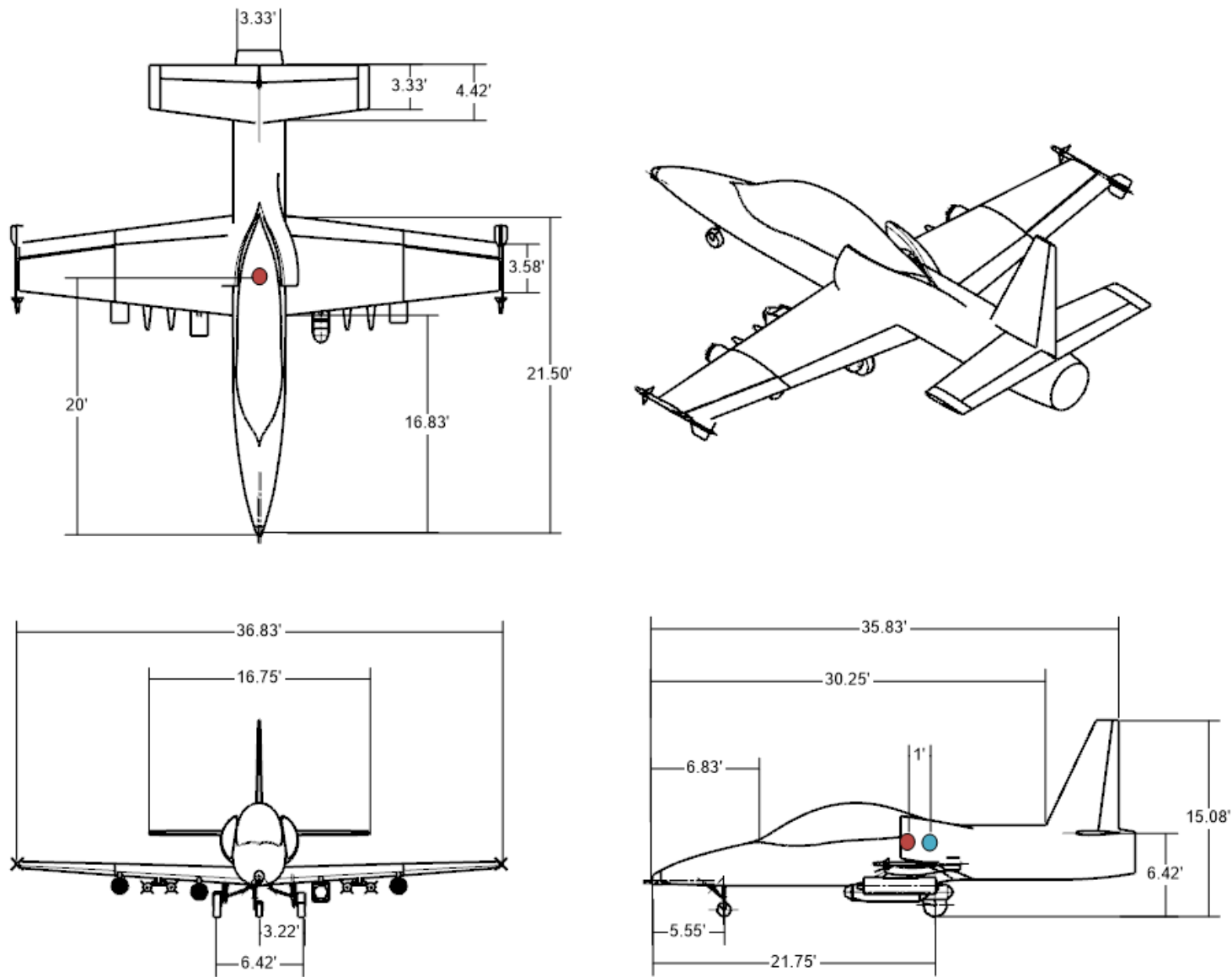


Fig. 12 Three-view Drawing of Spyro

With landing gear placement as mentioned above, tire size and oleo shock absorption system size could be determined using a statistical or empirical approach, as is introduced in Chapter 11 of Raymer [10]. Loads on the auxiliary and main gear are calculated by balancing static load and moment around the CG, yielding 1,226 lb and 6,130 lb, respectively. A summary of the landing gear configuration is presented in Table 6; extended and retracted positions can be found in Figure 14-17. For brevity of the report, only right main landing gear is demonstrated in the figures mentioned above. From the sizing analysis, wheel and tire are chosen from type III tires, assuming a 7% margin of load carried. The selected tires are 6.50-10PL14 and 5.00-5PL810 for main and nose landing gear respectively [13]. A passes number versus tire pressure plot on a field with a California Bearing Ratio of 5 was constructed in Figure 13 using methods mentioned in Chapter 12 of Aircraft Landing Gear Design: Principles and Practices [14], assuming tire deformation is kept within twenty percent of tire radius.

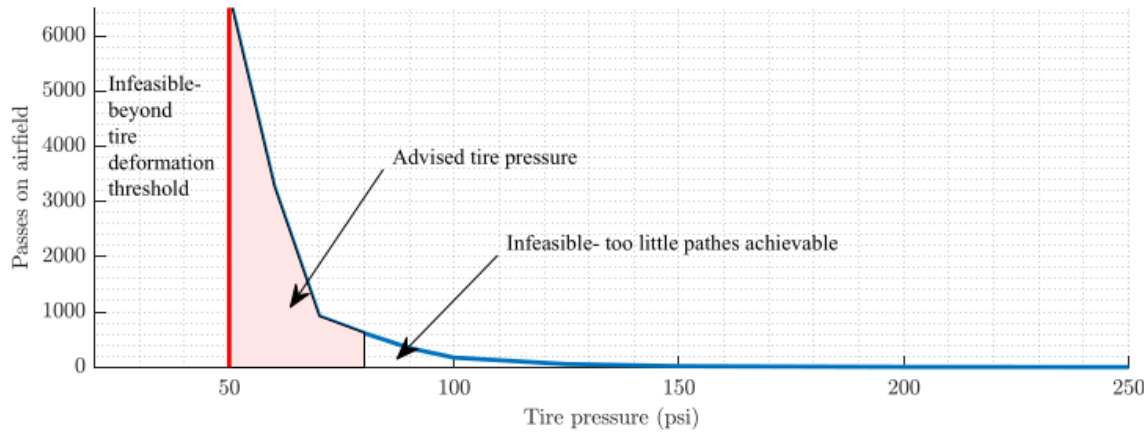


Fig. 13 Passes on Airfield with CBR = 5 versus Tire Pressure

A typical internal pressure of 1,800 psi is used for shock absorber. Main and auxiliary landing gear shock absorber diameters are to be 2.8 and 1.2 in. The designed landing gear dimensions are fully capable of retracting into the fuselage, thus no additional pods to contain landing gears are designed in favor of drag characteristics.

Drag braces are designed such that all landing gears retract forward and extend rearward. Such design increases the chance of success during a crash landing and improves the survivability of the aircraft: In case of hydraulics failure, landing gear doors can be discarded, and landing gears will automatically extend under aerodynamic loads and gravity.

Table 6 Landing Gear Sizing and Positioning Summary

Landing Gear	Nose	Main Left	Main Right
X Position (w.r.t. CG) [ft]	-10.0	1.00	1.00
Y Position (w.r.t. CG) [ft]	0.00	-3.25	3.25
Z Position (w.r.t. CG) [ft]	-3.00	-3.00	-3.00
Tire Size (d/w) [in]	17.80/ 5.00	22.40/ 6.50	22.40/ 6.50
Oleo Diameter [in]	1.20	2.80	2.80
Length [ft]	2.10	1.90	1.90
Load on Wheel (Max) [lb]	1,226	6,130	6,130
Design Load [lb]	1,777.7 (1.45 static load)	6,559.1 (1.07 static load)	6,559.1 (1.07 static load)
Tire type	Type III 5.00-5PL10	Type III 6.50-10PL14	Type III 6.50-10PL14
Tire pressure used/allowed [psi]	70/88	70/164	70/164

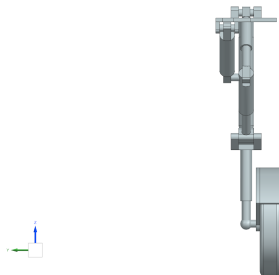


Fig. 14 Nose Landing Gear, Extended

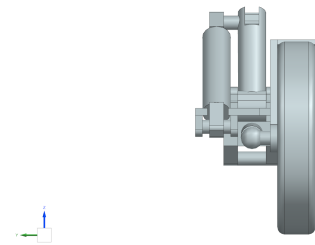


Fig. 15 Nose Landing Gear, Retracted

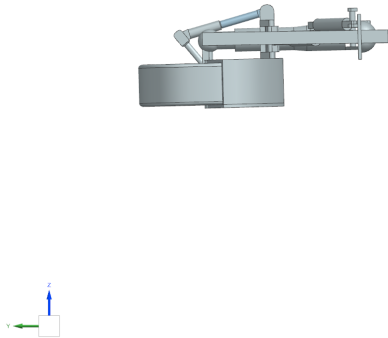


Fig. 16 Main Landing Gear, Retracted

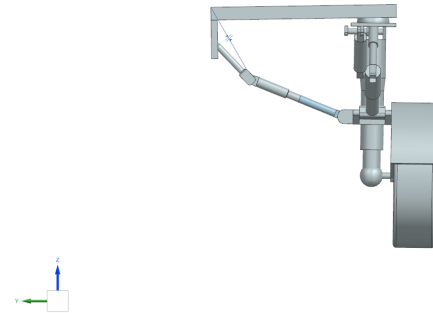


Fig. 17 Main Landing Gear, Extended

C. Interior

As will be later mentioned in Section XI, an avionics bundle and ejection seat have been decided upon for the current design iteration. The Martin Baker Mk16 ejection seat has been selected given its zero-zero capability and use in other aircraft of similar role, such as the T-6 Texan II. Given the geometry of this ejection seat and the current fuselage dimensions, a tandem seating configuration has been selected, allowing for two-pilot operation while maintaining a narrower, more aerodynamic fuselage profile. Cockpit avionics will be selected from among the CMC Electronics

Cockpit 4000 modular glass cockpit system designed for the LAAR role [15].

The majority of the internal systems are located in two primary system bays. The first is located beneath the cockpit for easy ground access. The second is located behind the cockpit in a vertical orientation. Extracting any system component from the lower bay is possible with hand tools alone, whereas extracting a system component from the rear bay requires a crane, due to a downward extraction path being blocked by the carry-through wing structure. Additional discussion of system component placement is found in Section XI.H.

1. Cockpit Viewing Angles

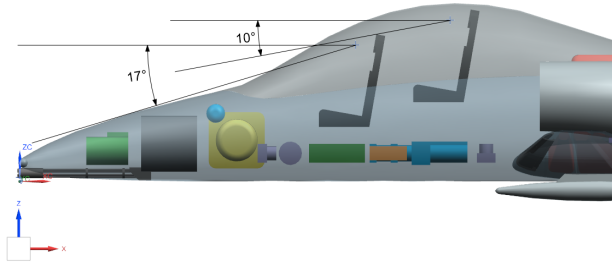


Fig. 18 Forward-Looking Viewing Angles

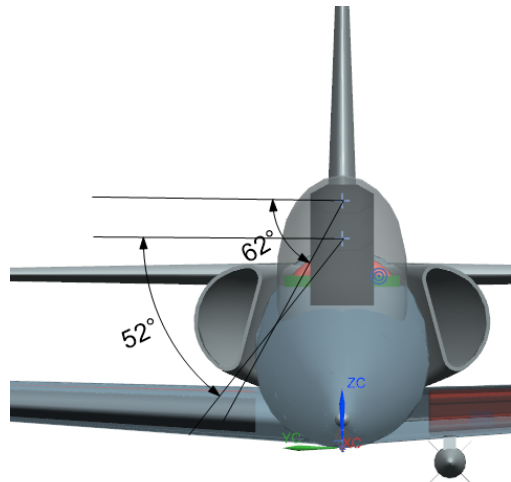


Fig. 19 Right-Looking Viewing Angles

The cockpit canopy contour was designed such that possible seat placements allow for sufficient visibility both forward and sideways. The front seat has a downward viewing angle of 17 degrees, constrained by the seat height and nose contour. The rear seat has a downward viewing angle of 10 degrees, constrained by the back of the front seat. The constraining object for both the front and rear seats sideways views is the canopy base. The rear seat, being positioned higher up, can look rightward up to 62 degrees below the local horizontal, whereas a viewing angle of 52 degrees is possible from the front seat. Viewing angle requirements as defined by MILSPEC standards are satisfied by the current seat arrangement and canopy contour.

V. Propulsion

A. Engine Type Selection

The propulsion systems most commonly used on aircraft are reciprocating engines and turbine engines, producing either shaft power or jet thrust. Reciprocating engines are immediately seen as not feasible because they are unable to produce the amount of thrust needed for this mission with a reasonable engine weight, as will be seen in Section VII.

Therefore only turbine engines were considered for Spyro.

After deciding between reciprocating engines and turbine engine, the next deduction that needed to be made was between a jet engine or prop engine. The two factors that primarily determined this decision were configuration options and operation in austere field conditions. Turboprop engines have two common configurations on aircraft. The first is having a single turboprop engine on the nose of the aircraft. Unfortunately, this configuration eliminates the possibility of placing a gun on the nose of the fuselage. The other possible configuration is a turboprop engine under each wing. This configuration creates multiple issues, including increased drag as well as less availability on the wings for ordnance placement. Jet engines, on the other hand, have a configuration option that places the engine inside the rear of the fuselage. This placement maximizes the available space for ordnance on the wings and it allows the engine to act as a counterweight for the nose gun that can be placed. Analyzing operation in austere fields, turboprops are able to perform best on their own in these conditions. However, with proper inlet configuration, jet engines are also able to perform well in austere fields. With all factors considered, and taking into account the fact that jet engines provide higher thrust output and, as a result, allow the aircraft to travel at higher speeds, jet engines are a better design choice for Spyro.

Finally, the decision between turbojet and turbofan engines can be made. A comparison between average T/W ratios and average thrust specific fuel consumption is presented in Table 7.

Table 7 Comparison of Different Turbine Engine Types

Type	Average T/W	Average TSFC [lbm/lbf-hr]
Turbojet	7.0	0.8-1.0
Turbofan	5.0	0.45-0.6

While turbojet engines have an advantage in T/W ratio, the more important factor in choosing an engine type is TSFC. Having a lower TSFC minimizes fuel weight required as well as the overall fuel cost throughout the aircraft's lifetime. Since less fuel is burned for a given mission, the cost of fuel is minimized for that mission as well. Since the RFP [1] prioritizes the affordability of the designed aircraft, minimizing fuel consumption is essential. Therefore, turbofan engines were chosen over turbojets as the type of engine that would be used for Spyro. A summary of the engine type decision making process is presented below in Table 8.

Table 8 Engine Type Selection Figures of Merit

Attribute	Turbofan	Turbojet	Turboprop	Possible Score
Fuel Consumption	5	1	4	5
Ordnance Placement	4	4	1	4
Austere Field Operation	2	2	3	3
T/W	2	3	1	3
Total Score	13	10	9	15

B. Number of Engines & Engine Location

The most beneficial aspect of electing to use two engines is survivability. In austere field conditions and in combat, is it more likely for an engine to become damaged or experience other possible mishaps. Having two engines allows the aircraft to remain operable if one engine were to be damaged. Two engines also allow for higher thrust capabilities, but this can also be achieved by choosing a single, more powerful engine. Using a single engine lacks redundancy but holds several benefits in configuration and mass distribution. First, having a single engine eliminates the possibility of putting engines on wings, which gives greater wing availability for any ordnance. Also, a commonly-used single-turbofan engine configuration has the engine placed in the rear of the aircraft, as seen on the IA-63 Pampa. This configuration centralizes the center of gravity of the aircraft by acting as a counterweight to a nose cannon placed at the front of the aircraft.

A configuration seen on the A-10 Thunderbolt involves two turbofan engines mounted to the rear of the aircraft. This was considered a possibility but it was decided that, with proper engine selection, a single turbofan engine can provide the same thrust as two turbofan engine with less overall weight. Analyzing both possibilities, it was found that having a single turbofan engine placed at the rear of the aircraft is the most practical decision for this design mission. While having two engines is most beneficial for survivability, having a single engine allows for space for ordnance to be placed and overall, allows for a lighter and cheaper aircraft. Armor has been placed beneath this rear engine, which will be detailed in Section XIII.

C. Engine Selection

Several turbofan engines that have been used on similarly-sized aircraft were analyzed. The engines that most closely fulfilled the requirements of the design and ferry mission detailed in the RFP [1] are presented in Table 9 [16].

Table 9 Trade Study of Different Engines

Engine	Aircraft Application	Max Thrust [lbf]	Sea-level TSFC [lbm/lbf-hr]	T/W
Honeywell TFE731-2	FMA IA-63 Pampa	3,500	0.493	4.7
Honeywell TFE731-40	C-38 Courier	4,250	0.457	5.6
Williams FJ44-1	Aero L-39 Albatros	1,900	0.456	4.13
Honeywell/ITEC F124	Aero L-159 Alca	6,280	0.78	5.98
Ivchenko AI-25	KB SAT SR-10	3,800	0.57	4.94

Comparing these engines, it became apparent that the Honeywell TFE731 variants were the most practical. The Williams engine, while it had a lower specific fuel consumption, did not offer the thrust capabilities of the TFE731 family. The Honeywell/ITEC engine has a specific fuel consumption that is far too great in comparison to the other engines and its thrust is greater than what is required for this mission. The Ivchenko is most comparable to the TFE731, but, with a higher specific fuel consumption. When deciding between the two TFE731 variants, the final decision hinged on the maximum amount of thrust needed for the design mission, which corresponds to the thrust required at takeoff. As seen in Figure 12, it was found that a higher thrust results in a lower required wing area which, in turn, minimizes the empty and maximum takeoff weights of the aircraft. Therefore, it was decided that the Honeywell TFE731-40 engine would be used for Spyro. This variant also has a lower specific fuel consumption in comparison to the TFE731-2 variant. Therefore, with a lower empty weight, fuel weight, and maximum ramp weight, the Honeywell TFE731-40 variant is the better choice for Spyro.

D. Engine Performance & Operation

While analyzing the performance of the TFE731-40 turbofan engine, it became clear that there are common trends between this and other turbofan engines with regards to its performance trends in relation altitude and Mach number. Therefore, the trends presented in Figures 20 and 21 for the TFE731-40 were based on generalized data for all turbofan engines presented in Raymer Appendix A [10]. These figures present how full throttle TSFC varies with altitude and Mach number and the relationship between thrust available, full throttle TSFC, and altitude.

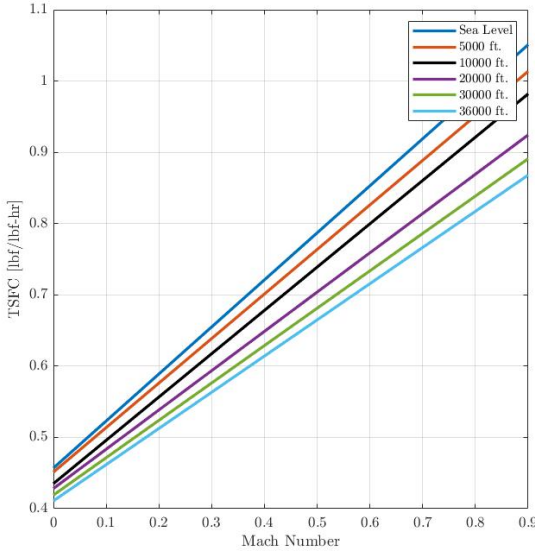


Fig. 20 Full Throttle TSFC vs. Mach vs. Altitude

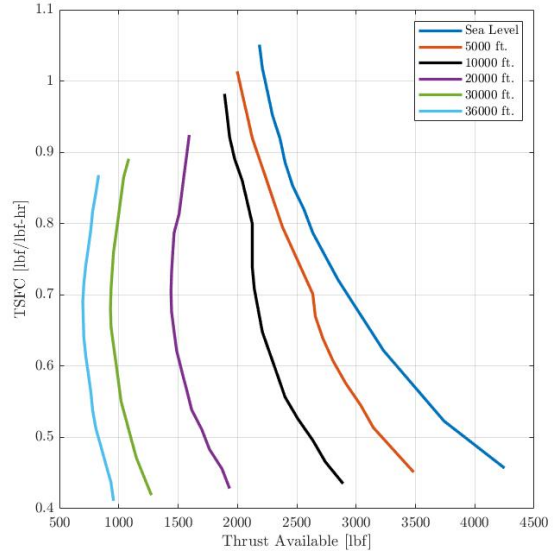
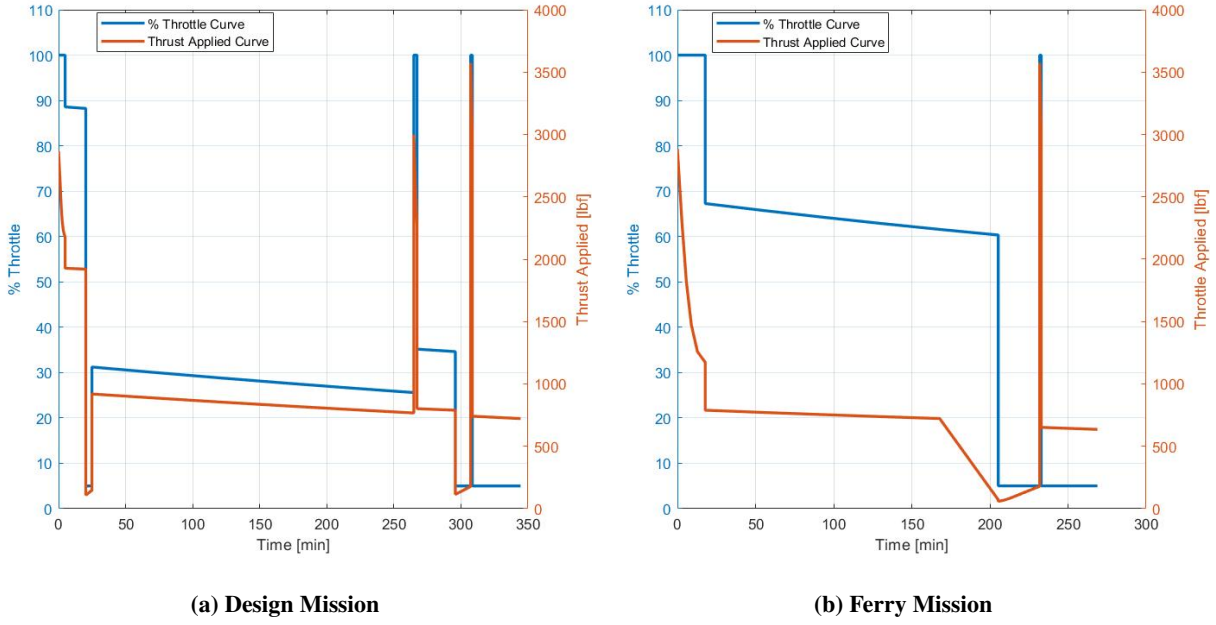


Fig. 21 Full Throttle TSFC vs. TA vs. Altitude

In Figure 20, there is a positive linear relationship in how full throttle TSFC varies with Mach number. Also, it can be observed that TSFC is lower at higher altitudes. In Figure 21, it appears that full throttle TSFC and thrust available have a parabolic relationship. As TSFC increases, thrust available tends to decrease, before eventually coming to a point where thrust available begins to slightly increase with an increase in TSFC. Thrust available also tends to decrease as altitude increases.

To illustrate how the engine operates over the design mission and the ferry mission, plots of the throttle and thrust applied throughout the entirety of each mission are provided in Figures 22a and 22b. For the design mission, Spyro cruises at roughly 88% throttle for the first cruise stage, roughly 35% for the second cruise stage, and loiters at roughly 30% throttle. Loitering at a lower throttle causes the engine to consume less fuel and, due to the loiter mission taking up a large amount of time, consuming less fuel is optimal. For the ferry mission, Spyro cruises at roughly 66% throttle. The applied thrust and throttle do not directly relate due to altitude variation causing the thrust available from the engine to decrease, as illustrated in Figure 21.



(a) Design Mission

(b) Ferry Mission

Fig. 22 Engine Throttle & Applied Thrust Throughout Each Mission

E. Inlet and Exhaust Design

For Spyro, a Y-duct configuration was decided as an inlet duct system. An inlet protrudes from each side of the fuselage behind the cockpit and above the wings, with each converging to feed the turbofan engine at the rear of the fuselage. To operate properly in austere field conditions, these inlets were placed as high as possible on the fuselage to prevent foreign object debris from being picked up and entering the engine. Each of the inlets has a capture area of 4.47 ft^2 . The air converges and enters the engine, combining to create an exit area of 8.95 ft^2 from the duct into the engine. This exit area is also the area of the exhaust. The total length of the duct is 12 ft. According to Raymer [10], this type of inlet design typically has a pressure recovery of 94%, which corresponds to a 7% reduction in installed thrust. Through CFD analysis, it was found that, while the pressure contours at the entrance of the inlet were variable, the pressure contours at the entrance to the engine after air coming from each inlet converges in the Y-duct were constant, proving an optimal pressure recovery. This, and other specifics about the aerodynamics of the inlet will be covered in greater detail in Section VI.

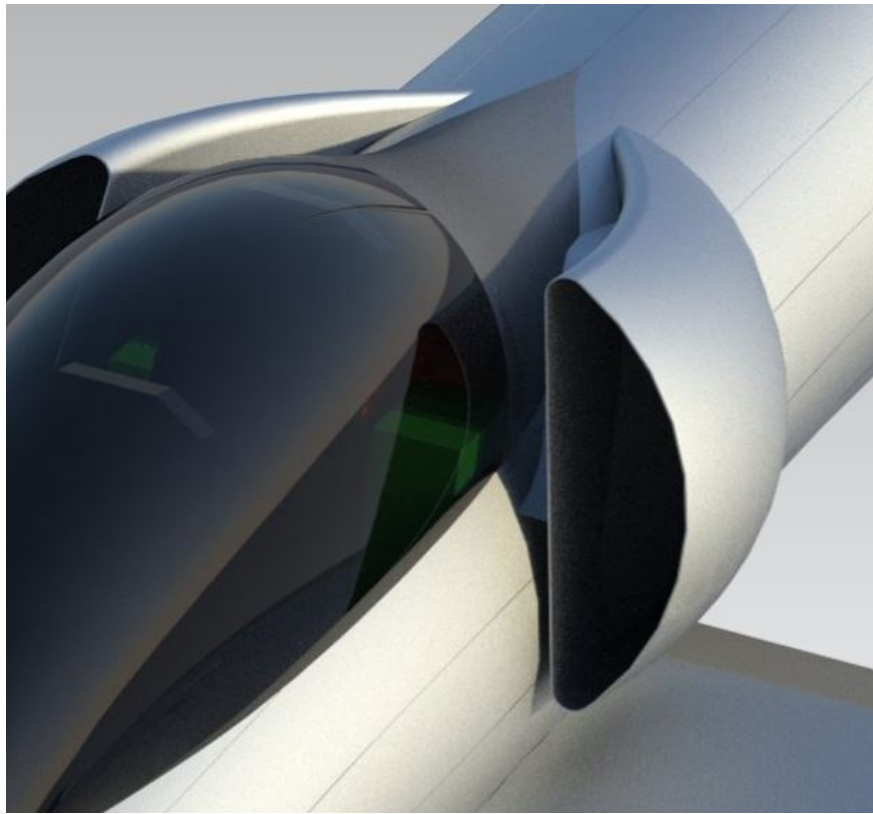


Fig. 23 NX Rendering of Y-Duct Inlet

The exhaust system of a turbofan aircraft is especially important because the exhaust is where most thrust from the engine is generated. From the inlets, air converges, enters the engine, and exits the exhaust, which has an exit area of 8.95 ft^2 . The exhaust also generates extremely high temperatures and therefore, it is essential for the exhaust system to be made of materials that can withstand these conditions. The material most commonly used in aircraft exhaust is stainless steel. Stainless steel is able to withstand the temperatures generated by an exhaust and, therefore, it was sued for Spyro's exhaust design.. From a survivability standpoint, it is also essential for an infrared suppression system to be put into place that can conceal these high temperatures and prevent infrared signatures from being seen. Spyro's exhaust features chevrons which assist in masking thermal signatures. This will be covered in greater detail in Section XIII.

F. Propulsion & Fuel System

For detailed analysis on specific engine system placement and engine controls, see the Engine Controls section (Sec. XI.B). For details about Spyro's fuel tank layout and overall fuel systems, see the Fuel System section (Sec.XI.C).

VI. Aerodynamics

A. Desired Characteristics

When choosing aerodynamic parameters of the aircraft, the RFP should first be analyzed for what may affect the engineering decisions on this aircraft. Take off and landing field length is one of the primary design drivers due to the rough and high resistance field conditions it will have to endure. The next requirement states the amount of armament on the aircraft meaning that the wing may need provisions for mounting some or all of this armament under the wing. Another requirement that affects the aerodynamic design choices is the ceiling requirement of 30,000 ft. Finally, although not a requirement, an effort should be made to make construction and maintenance of the aerodynamic structures as affordable as possible.

Referencing the sizing process done in Section III, an initial estimate can be made for the size and shape of the aerodynamic surfaces. It must be noted that the various seed aircraft referenced during the sizing process each generate a different optimal wing area and aspect ratio. However, after refining these sizing scripts, these optimal parameters became more and more independent of seed aircraft, instilling more confidence in a correct wing area. The different seed aircraft also leads to the refinement from 200 to 206 square feet for wing area.

B. Airfoil Selection

This aircraft will spend a significant amount of time loitering and in cruise, meaning C_L/C_D and $C_L^{\frac{1}{2}}/C_D$ are key performance parameters given the use of a jet propulsion system. An airfoil that can perform these tasks well is needed. Another key airfoil parameter is the takeoff requirement, which means a high $C_{L_{max}}$ will be needed in order to reduce the amount of high lift devices required, both reducing complexity and cost. Finally on the topic of cost, the airfoil must be easily manufactured into a functioning wing. Therefore a spline simple enough where no special manufacturing methods are required is desired.

Several airfoils were selected from similar class aircraft for comparison. The major data about the foils are shown below in Table 10.

Table 10 Airfoil Similarity Data

Aircraft	Root			Tip		
	Profile	Thickness	Camber	Profile	Thickness	Camber
Super Tucano	NACA 63A415	15%	2.2%	NACA 63A212	12%	1.1%
A-10 Thunderbolt	NACA 6716	16%	6%	NACA 6713	13%	6%
Cessna T-37	NACA 2418	18%	2%	NACA 2412	12%	2%

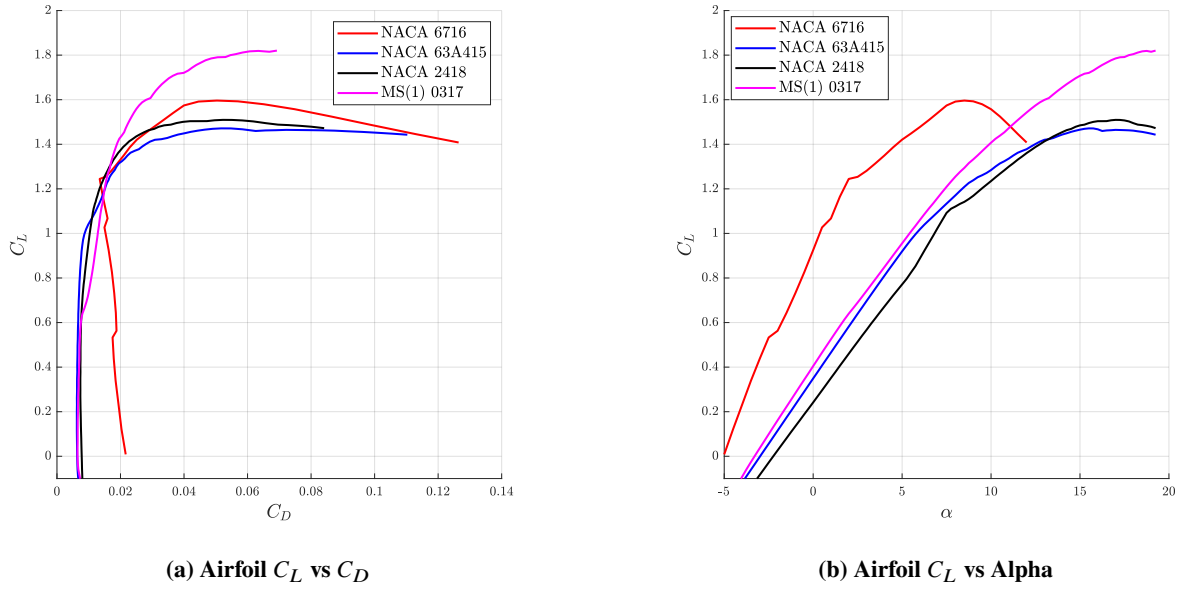


Fig. 24 Airfoil Lift Curves

The comparison of the data is done using the multiple parameters mentioned above as well as the aerodynamic curves in Figure 24a and 24b. These two plots show the high $C_{L_{\max}}$ and the soft stall qualities of the MS(1) which is why it is chosen over any of the 4 series NACA airfoils and even the 6 series airfoil on the Super Tucano. The main advantage that the more basic geometry airfoils have is easier manufacturing and cheaper maintenance due to less overall complexity. This advantage can be mostly overlooked due to the fact that the MS(1) airfoil can still be lofted into wing geometries using similar construction methods to a NACA 4 series airfoil. The MS(1) has been used before on aircraft such as the Saab 2000 and the Aero AE 270 Spirit.

The final airfoil chosen was a modified version of the NASA medium speed airfoil (MS(1)). The airfoil is designed to have a high $C_{L_{\max}}$ while also having reasonable C_L/C_D and $C_L^{\frac{1}{2}}/C_D$ during high speed cruise. This class of airfoils also includes a low speed family, although to improve cruise speed the medium speed (MS) was chosen instead. This slightly decreases the $C_{L_{\max}}$ value but moves drag divergence to higher mach numbers above 0.7 which is significantly above the cruise speed of 0.49 for ferry and 0.61 for the design mission. Using the XFOIL inverse design tool, the airfoil was slightly optimized from the MS(1) class of airfoils to have a higher $\frac{L}{D}$ at cruise. This airfoil will be referred to as MS(c) although most characteristics are similar to the MS(1) class of airfoil.

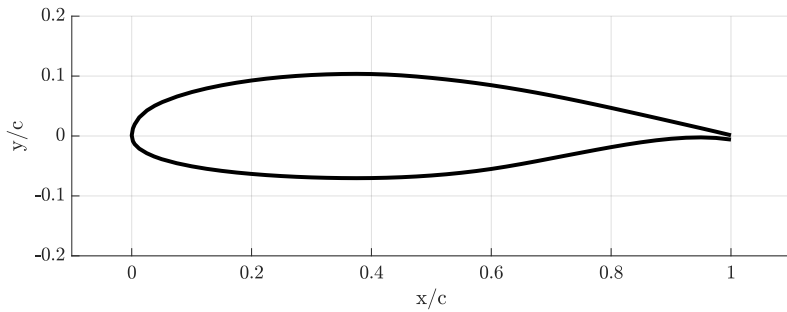


Fig. 25 Modified NASA Medium Speed Airfoil at Root

C. Wing Design

The wing size is based on similar requirements to the airfoil selection process. Due to the selection of the NASA medium speed airfoil family, the aircraft can have a thicker airfoil at higher Mach numbers without experiencing premature drag divergence. Therefore, a larger aspect ratio can be chosen while maintaining the same weight compared to a wing of smaller aspect ratio with a thinner airfoil section. The wing area is justified more in Section III although in short the wing area is a balance between completing the missions as efficiently as possible and successfully performing the take off and landing segments of the mission.

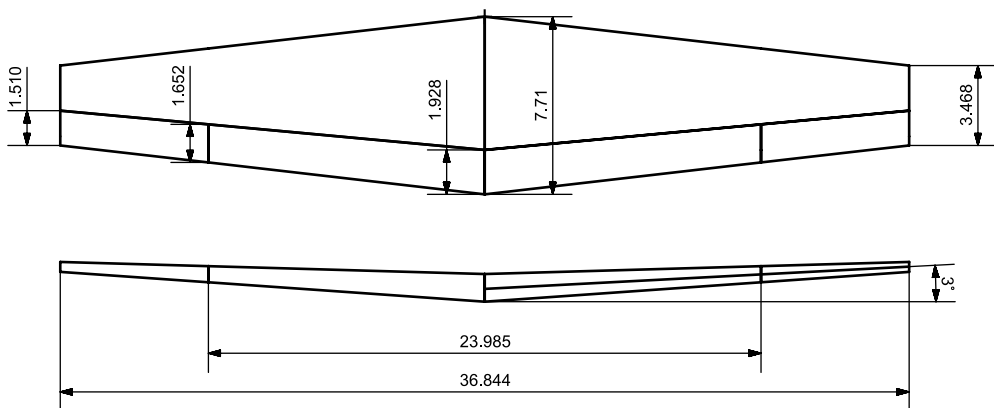


Fig. 26 Major Wing Dimensions

Table 11 Wing Geometry Tabulated

Wing Area	Aspect Ratio	Span	Taper Ratio	Root Airfoil	Tip Airfoil	Dihedral	Twist
206.25 ft ²	6.58	36.9 ft	0.45	MS(c)-0617	MS(c)-0613	3 Degrees	0 Degrees

The wing root and tip airfoil thicknesses were chosen to balance aerodynamic performance with structural considerations, and the wing was tapered in order to get a better elliptical lift distribution which could later be analyzed in programs such as AVL. Due to the design point of the airfoil being changed at different parts of the span, which could have possibly reduced performance of the wing, no geometric twist was included. Additionally no wing sweep was added in order to maximize the useful lift that could be generated by the wing.

D. Drag Buildup

In order to ensure that the drag has been properly estimated, multiple methods can be used to determine and compare C_{D0} values. Currently, the protuberance drag is assumed to be 10% C_{D0} of the aircraft with no ordnance. It is mentioned that common protuberance percentages are 5% to 10% for newer fighters and 10% to 15% for older fighters [10]. The 10% value was chosen because although this is a newer aircraft, some sacrifices will most likely need to be made during detailed design. Allowing for this margin gives the team the ability to make manufacturing easier and therefore produce a more affordable aircraft.

The C_{D0} used for future calculations will be the average value between two methods: VSP calculations and Raymer calculations. These are tabulated in Table 12.

Table 12 Drag Buildup

Surface	$S_{\text{wet}} [\text{ft}^2]$	C_{D0} VSP	C_{D0} Raymer	Difference
Wing	405.73	0.00792	0.00764	3.58%
Fuselage	281.33	0.0032	0.00316	1.22%
Horizontal Tail	104.66	0.00188	0.00200	6.24%
Vertical Tail	60.09	0.00105	0.00114	8.18%
Intake	24.215	0.001	0.00339	35.56%
Perturbation Drag	-	0.0015	0.001542	2.75%
Total	876.02	0.01655	0.01697	2.75%
Single Mk82	60.95	0.00078	0.00097	21.68%
Single Pylon	2.16	0.00021	0.00016	26.04%
Total 60% Ordnance	1125.06	0.0201	0.0210	0.30%
Total 100% Ordnance	1249.59	0.0225	0.0237	1.76%
Average Design	1249.59		0.0231	
Takeoff Flaps	-	0.003	0.00276	8.33%
Landing Flaps	-	0.0031	0.00552	56.14%
Gear	-	0.00363	0.00363	0.00%
Full Ordnance Take Off	1249.59	0.0255	0.0266	4.22%
Full Ordnance Landing	1249.59	0.0256	0.0293	13.4%

Note that the $\frac{S_{\text{wet}}}{S_{\text{ref}}}$ value of the aircraft varies greatly from 4.25 with zero ordnance to 6.06 with 100% armament load out. This number could also change depending on the type of armament added as multiple rail launch rockets mounted

on a single pylon could add even more surface area.

E. Aerodynamic Data

Multiple methods were used to get estimates for C_L and C_D of the aircraft. Each method uses its own assumptions and some are more complex than others. The various methods and their results are shown below in Figure 27 and Figure 29.

The first method to find the aerodynamic properties was empirical methods from Chapter 12 of Raymer, by taking multiple wing parameters such as cruise mach, wing area, and span; a fixed $C_{L\alpha}$ could be determined. Next the VSP method uses the vortex lattice method (VLM) including ordnance and the fuselage. The XFLR5 method did not include any of the lift generated by other surfaces besides the wing and empennage. Finally the CFX model is presented in Figure 28, which is a model of the wing simulated in ANSYS CFX. It should be mentioned that although the C_L values are within range, the C_D values are too large to be plausible. This is likely because the boundary layer mesh must be refined which cannot be done with the current ANSYS student mesh cap. This is also why the CFX method did not make an appearance in the drag polar plot.

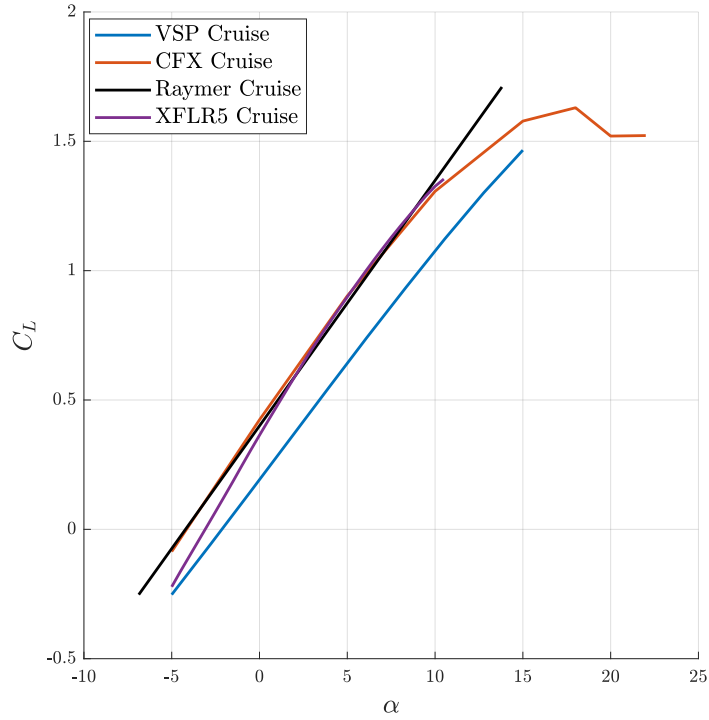


Fig. 27 C_L vs Alpha of Plane at Cruise

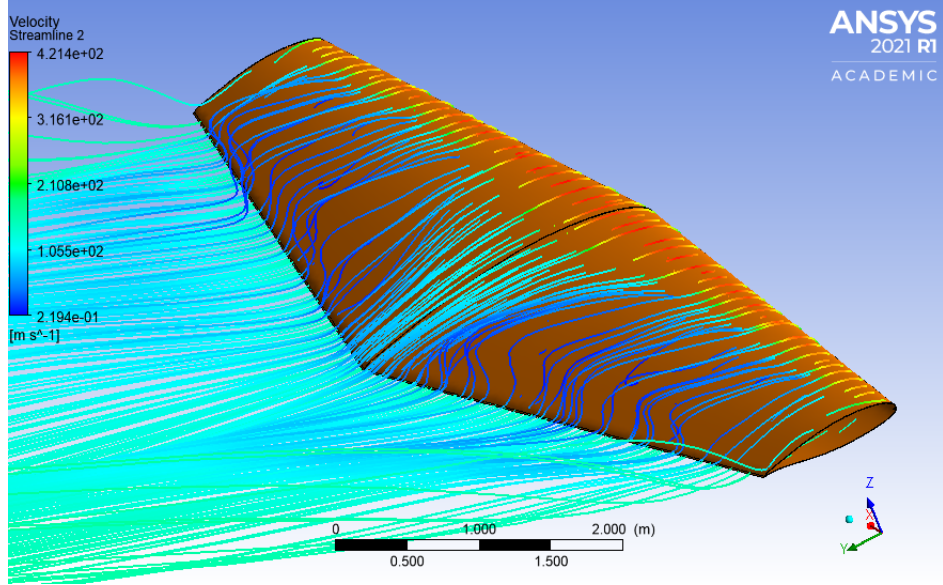


Fig. 28 CFX simulated Flow at Stall

Curves are calculated at cruise velocity with full ordnance, with the exception of the XFLR5 data which had to be run at a lower Reynolds number in order to get proper convergence. The Raymer method uses the estimated span efficiency of 0.856 which was calculated using AVL, then C_L was swept between that which is produced at an angle of attack of -5° and the calculated $C_{L_{max}}$ using empirical relations from Chapter 10 of Raymer[10]. This was added to the C_{D0} calculated in the previous section.

The circle and star represent locations for optimal performance, with the circle representing maximum $\frac{L}{D}$ which is optimal for loiter for a jet aircraft and the star represents maximum $\frac{L^{\frac{1}{2}}}{D}$ which represents optimal cruise for the aircraft (Figure 29). Below are these values at each segment of the design mission. These results were averaged and then given to other teams such as performance for their analysis. Average values during mission segments are shown below in Table 13.

Table 13 Aerodynamic Parameters During Mission

Segment	C_D	C_{D0}	C_L	α
Takeoff (15° Flaps)	0.0392	0.0261	0.507	1.138
Cruise	0.031	0.0226	0.403	0.00
Loiter	0.0367	0.0226	0.524	1.317
Landing (40° Flaps)	0.243	0.0274	2.054	18.156

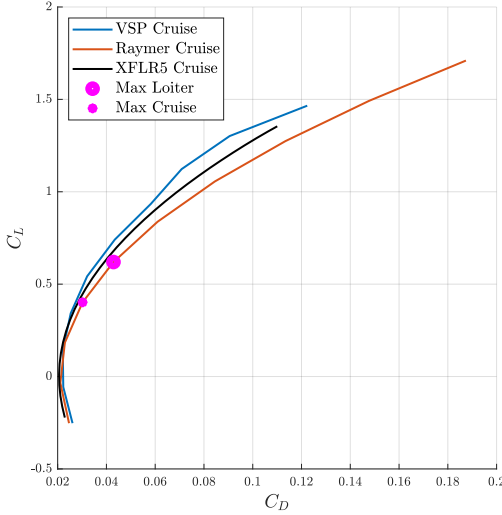


Fig. 29 C_L vs C_D of Plane at Cruise

F. High Lift System

There are many types of high lift systems, and in order to better quantify these options a range of aircraft can be examined at to see what common solutions exist. As shown in Table 14 below, these aircraft all have various high lift devices and each method has its own benefits and drawbacks. The TOP mentioned in the table below is the Chapter 5 Raymer [10] takeoff parameter which is a ratio of all of the relevant parameters for take off and can be used to estimate takeoff field length. In this case, it is used instead to estimate the required $C_{L_{\max}}$ for each system as the take off distance is already defined for these aircraft.

Table 14 Similar Aircraft High Lift Devices

Plane	Device	Span Fraction	Chord Fraction	TOP	Estimated $C_{L_{\max}}$
A-10 Thunderbolt II	TE Flap	44.6%	30.4%	205.8	2.64
KAI T-50 Golden Eagle	LE Flap	69.6%	22.6%	69.6	2.82
	TE Flap	58.6%	20.0%		
Douglas A-4 Skyhawk	LE Slat	26.2%	25.7%	141.8	1.92
	TE Flap	20.8%	18.6%		

From these comparisons, the required take off parameter for the Sypro aircraft would be between 200 and 150, which is reported by Chapter 5 of Raymer [10] and Chapter 6 of Nicolai [17] respectively. Using this take off parameter a $\Delta C_{L_{\max}}$ could be used to find how much extra lift is needed from a high lift device. Based on this number, a slotted flap was originally selected with a span of 65%. This was refined because a slotted flap cannot deflect upwards unlike a simple flap, which allows for greater maneuverability. Using the simple flap as an aileron during high roll can give

this aircraft an edge apart from other similar aircraft in its class. In order to compensate for the decrease $\Delta C_{L_{\max}}$, the ailerons can also deflect to give a new flapped span of 85% where the remaining 15% is taken up by the fuselage and wing fillets. This would give a theoretical $C_{L_{\max}}$ of 2.48 for the aircraft with flaps fully deployed at 40 degrees.

This simple flap currently takes up 25% of the chord and the hinge location is located 76 inches away from the leading edge and 0.5 inches below it. The flapped section of the wing and the rearmost spar of the structure have enough space between them to fit actuators for the flaps and ailerons.



Fig. 30 Flap Cutaway at Root

As shown there is an offset between the C_L vs α in Figure 31 where the prediction for ΔC_L from AVL is consistently higher than the empirical ΔC_L given by Raymer or XFLR5. This could be due to the fact that the VLM does not perform well under higher angles of attack as separated flow cannot correctly be simulated and therefore the basic flap type may not be able to be properly estimated. Therefore an average between the empirical method and XFLR5 will be used to estimate ΔC_L .

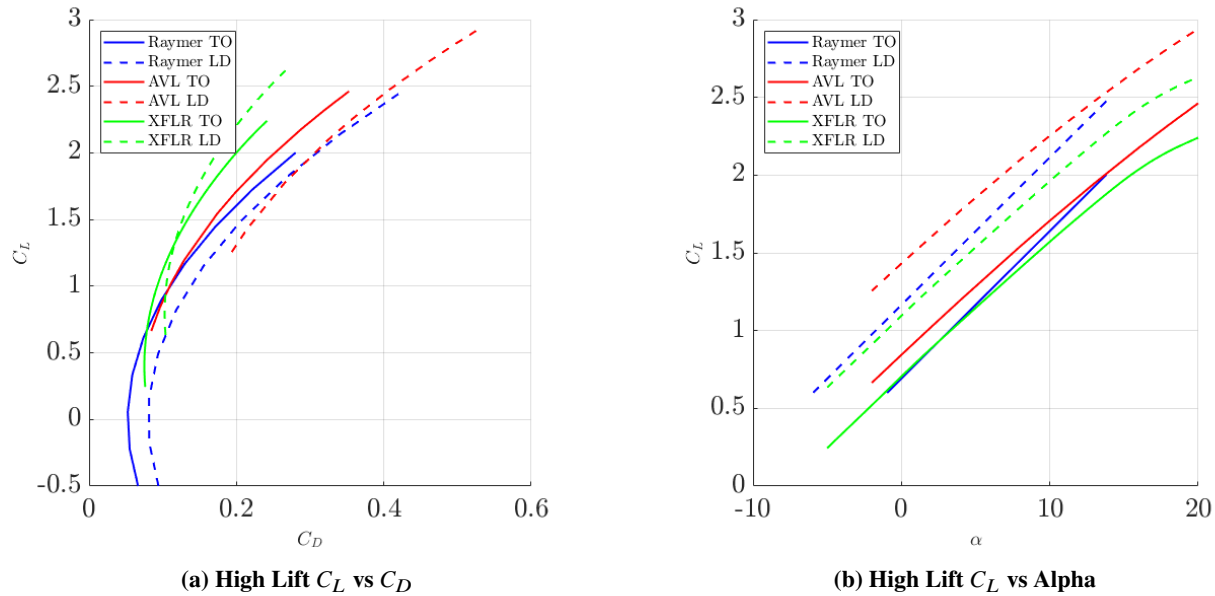


Fig. 31 Simulated High Lift Curves

G. Computational Fluid Dynamics

A CFD simulation was originally performed in ANSYS CFX. However, due to the 500,000 node mesh cap the simulation software was switched to SimScale for the simulation of the entire aircraft. SimScale is a browser based program which takes too long to produce a full lift or drag curve. Hence, rather the base flight case of loiter conditions was chosen for the entire aircraft simulation. SimScale uses a canned version of openFOAM and as such, similar results to an openFOAM simulation with proper boundary conditions and boundary layers meshed are expected.

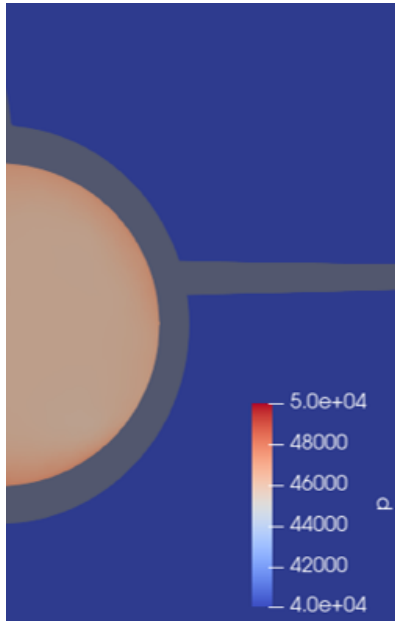


Fig. 32 Fan Face

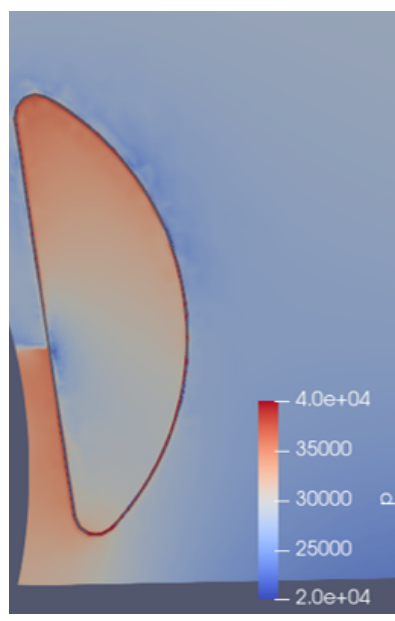


Fig. 33 Inlet Face

One concern for the aircraft aerodynamics is whether the inlet placement will cause trouble for the engine due to inadequate flow into the engine. As can be seen in the contour plots above, the fan face (Figure 32) becomes fairly uniform compared to the inlet contour (Figure 33). From these two Figures, the inlet placement was deemed to be sufficient. Given access to a full license of ANSYS or other CFD softwares, further simulations may be conducted to validate the obtained results.

VII. Performance

A. Performance Requirements

The RFP specifies that Spyro must be capable of satisfying the described ferry and design missions as shown in Section II while carrying the respective required payload for each mission. Also, the aircraft must be able to operate from austere fields at density altitudes up to 6,000 ft while taking off and landing within a 4,000 ft takeoff and landing field length. The performance of Spyro will be simulated and evaluated in order to optimize design parameters such as

weight, thrust, fuel burned, among others to result in the minimal cost and weight. The simulation will be done using a time step method for each mission segment that can provide data used for the accompanying trade studies and figures as well as validate the satisfaction of the RFP requirements. Additionally, trade studies will be provided to determine the optimal cruise conditions along with exploring the rate of climb behavior in comparison to similar light attack aircraft.

B. Takeoff Performance

As listed in the RFP [1], it is necessary to perform takeoff within 4,000 ft of the starting position. In order to verify Spyro's takeoff performance at the most strict conditions, the MTOW configuration will be used as the input weight for the takeoff simulation. Conditions at a 6,000 ft density altitude will also be accounted for as specified in the RFP. This will validate the takeoff performance at less resistant ground surfaces and lower altitudes. When simulating the takeoff performance, the complete takeoff distance is broken into segments that can be summed as described in Roskam [11]. These segments include a ground roll distance, transition distance, and climb distance.

First, the ground roll takeoff distance will be computed by time step integration. The ground roll time step integration accounts for the aircraft acceleration from a stationary start up to rotation speed, V_R . At this speed, Spyro will rotate to the transition position while reaching V_{LOF} in approximately 1.5 seconds [11]. Spyro will enter the transition segment at V_{LOF} and then proceed to the final climb segment, both described in detail in Roskam [11]. Each mentioned velocity is determined in relation to the stall velocity where V_R is equal to $1.1 * V_{Stall}$, and V_{LOF} is equal to $1.2 * V_{Stall}$. In Roskam's method, it is suggested to model the transition radius as a function of wing loading. The aircraft will then propagate the arc trajectory to the obstacle height, which is specified as an obstacle height of 50 ft by the RFP. To analyze the takeoff performance of Spyro, alternate conditions are investigated in the form of rolling ground coefficient, μ_g , listed in Roskam to test the limits of the aircraft. It is important to note that inputted control surface features are retrieved from Section VIII and the braking coefficient, μ_B , is selected as 0.3 as stated in Chapter 11 of Raymer [10].

Table 15 Takeoff Distance at Different Friction Coefficients

Surface Type	Coefficient Value [μ_g]	Takeoff Distance [ft]
Concrete and Macadam	0.025	3,164
Hard Turf/Short Grass	0.05	3,349
Long Grass	0.10	3,836
Soft Ground	0.10-0.30 (0.113 Limit)	4,000

The described method is simulated using varying rolling ground friction coefficients resulting from more resistant takeoff surfaces. From the data presented above, it can be observed that Spyro will satisfy the takeoff requirement for

surface conditions up to a rolling ground coefficient value of 0.113. A surface with a higher friction coefficient would result in a TFL greater than 4,000 feet. A complete breakdown of each segment utilizing the inputs described at Spyro's limit is demonstrated below representing each individual segment's contribution to the total takeoff distance.

Table 16 Takeoff Length by Individual Segment

Segment	Ground Roll	Rotation	Transition	Climb	Total Distance
Length [ft]	2,984	264	556	195	4,000

At the required 6,000 ft altitude, Spyro successfully takes off within the 4,000 ft field length requirement. Spyro satisfies the austere field conditions by investigating takeoff behavior with various rolling ground coefficients increasing to 0.113. Ultimately, Spyro takes off within the specified boundaries while clearing the 50 ft obstacle height and accelerating to a lift off speed of 116 knots.

C. Landing Performance

Similar to the takeoff analysis, the RFP specifies for Spyro to land within a 4,000 ft field length at a 6,000 ft density altitude to confirm the capability of landing under RFP specifications. To also confirm this capability, μ_g and μ_B will correspond to the same limiting conditions at the takeoff performance. As stated in Chapter 11 of Raymer [10], the braking coefficient will be selected as 0.3 and the limit of Spyro for the landing performance will be found by varying the max landing weight. Once again, the landing process is broken up into segments in the form of descent, flare, rotation, and ground roll. The descent and flare segments are empirically calculated with equations described in Roskam in contrast to the time-stepped rotation and ground roll segments [11]. The descent begins from the obstacle clearance height of 50 ft and accounts for the landing flight path angle. The flare distance will transition the approach velocity to the touchdown velocity using the passive aircraft drag along with wing drag devices. The rotation segment accounts for the distance covered while the nose of the aircraft is off the ground and finally the ground roll accounts for braking to zero velocity. The following distances calculated are provided below. When utilizing the same limiting rolling ground coefficient as in the takeoff analysis, the aircraft will reach the landing field requirements at 84% of the MTOW.

Table 17 Landing Length by Individual Segment

Segment	Descent	Flare (Transition)	Rotation to GR	Braking Ground Roll	Total Distance
Length [ft]	641	800	416	2,143	4,000

As observed above, Spyro successfully lands within the landing field requirements of the RFP while compensating for the rolling ground frictions that result from alternate landing surfaces. It should also be noted that the limiting max

landing weight, 84% of the MTOW, falls within a the feasible range of max landing weight as stated in Chapter 11 of Raymer as well. This range is listed as a 80-100% MTOW approximation for max landing weight. Also note that the LFL for long grass where $\mu_g = 0.1$, is 3,939 feet and is used as the reference value in other relevant sections of the report.

D. Performance Coefficients

For the selected geometry and aerodynamics of the aircraft, it is possible to sweep through varying Mach numbers and construct a model of performance coefficients as shown. Using the altitude and weight of the aircraft during the investigated flight segment, the optimal conditions can be studied on the following curves.

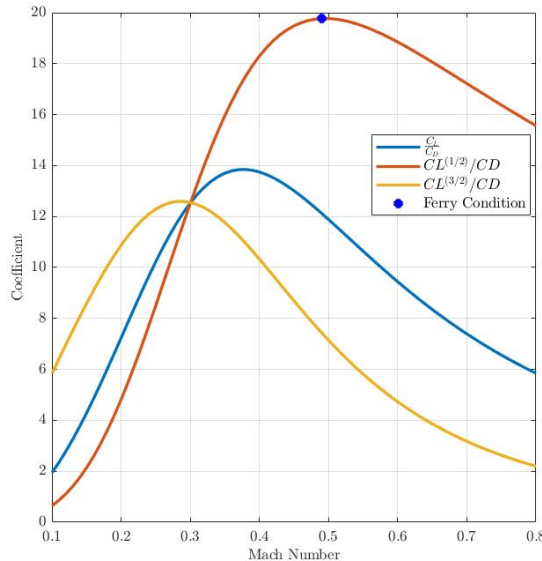


Fig. 34 Coefficients for Ferry Optimization

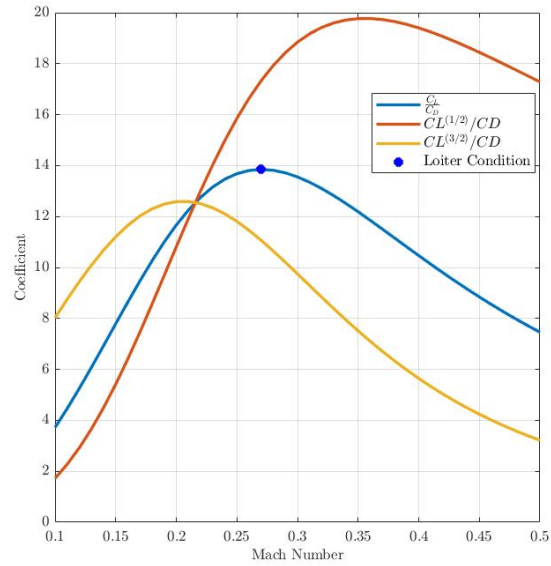


Fig. 35 Coefficients for Design Mission Optimization

Table 18 Performance Coefficients Tabulated

(a) Ferry Mission Coefficients

Coefficient	Value	Mach Number
$\frac{C_L}{C_D}$ max	13.85	0.38
$\frac{C_L^{1/2}}{C_D}$ max	19.77	0.49
$\frac{C_L^{3/2}}{C_D}$ max	12.59	0.28

(b) Design Mission Coefficients

Coefficient	Value	Mach Number
$\frac{C_L}{C_D}$ max	13.85	0.27
$\frac{C_L^{1/2}}{C_D}$ max	19.77	0.35
$\frac{C_L^{3/2}}{C_D}$ max	12.59	0.21

The provided performance coefficients describe the best performance at different conditions during the utilized missions. At the maximum determined value of C_L/C_D , the minimum thrust can be applied and therefore the best

endurance performance during flight is achieved. This will in turn correspond with the greatest performance during loiter. Thus, this condition is selected for the loiter segment to optimize the fuel burn of the design mission. At Mach numbers corresponding to the maximum value of $C_L^{\frac{1}{2}}/C_D$, the best range performance occurs for a turbofan engine. This will be useful when referring to the optimal cruise velocity of the ferry mission cruise segment. Finally, the $\frac{C_L^{\frac{1}{2}}}{C_D \max}$ can be referred to for the minimum sink during gliding flight. As shown on the curves, the maximum $C_L^{\frac{1}{2}}/C_D$ condition will be selected for the ferry mission cruise segment and further studied when discussing the trade study for optimizing cruise conditions. The greatest amount of fuel burned occurs during the loiter segment of the design mission, therefore the condition specified in Figure 37 will represent the main criteria for optimizing the fuel burned over the course of the design mission.

E. Service and Absolute Ceiling

The RFP specifies a service ceiling requirement of at least 30,000 ft. The service ceiling is computed by determining the altitude when the maximum rate of climb (ROC) equals 500 ft/min [10]. For turbofans like the one selected for Spyro, it is known that the maximum rate of climb is a result of the maximum excess thrust. The maximum rate of climb will also occur at the previously shown maximum L/D velocity. Using the Mach number at the maximum L/D value, the rate of climb becomes equal to 500 ft/min at 30,646 ft suggesting Spyro's service ceiling at MTOW. It is also important to note the absolute ceiling of the aircraft, or the altitude that the aircraft will no longer be able to climb. This occurs for Spyro at 35,085 ft altitude. The absolute and service ceiling can be demonstrated further on the specific excess power diagram.

F. Specific Excess Power

The climb performance of Spyro can be studied while investigating the contour plot of specific excess power as shown. This diagram will suggest the climbing capability of Spyro at each provided altitude and Mach number. The key conditions that are of note are the initial climb during takeoff which aligns to approximately 30 ft/s, or 1,800 ft/min. This occurs at an initial climb speed of approximately 193 knots. For Spyro's takeoff simulation, the rate of climb is computed at a maximum of 1,759 ft/min falling within the parameters of the specific excess power constraints. The other condition of note from the studied diagram is at the absolute ceiling previously calculated. It can be observed how at an altitude of 35,085 ft, the specific excess power at this altitude is 0 ft/min. At the absolute ceiling of the aircraft, there is no more capability of climbing altitude and therefore Spyro is limited to altitudes below its absolute ceiling for functioning flight.

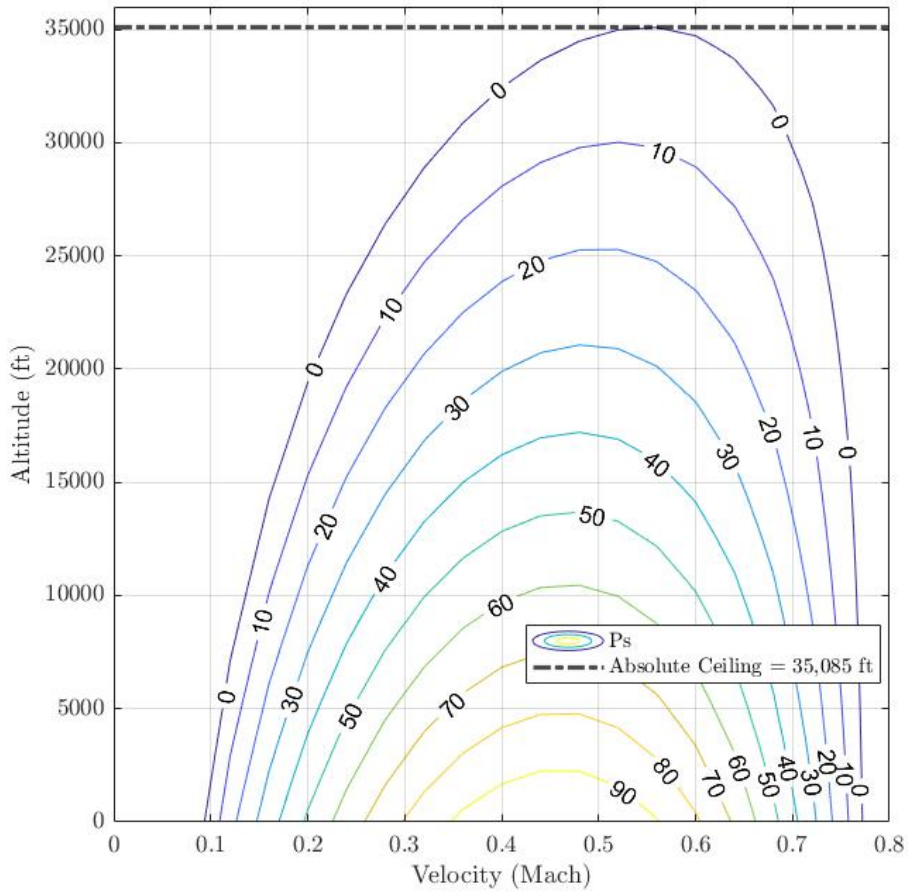


Fig. 36 Specific Excess Power Diagram

G. Flight Envelope

The flight envelope for Spyro is provided below and is constrained by the velocity boundaries calculated. The maximum velocity is limited by both the excess power of the aircraft nearing 0 as well as the contributions from the Mach divergence increasing drag and structural impacts on the aircraft. At sea level, this maximum velocity occurs at Mach 0.77. The high velocity for Spyro is due to the high bypass turbofan engine selected providing the thrust sufficient for high speeds desired for combat and close air support. In contrast, the minimum velocity consists of two segments including the stall boundary at lower altitudes computed at constant MTOW. At approximately 25,000 ft altitude, the minimum velocity boundary becomes a result of excess power similar to the maximum velocity boundary. At sea level, the minimum velocity of Spyro can be observed to be Mach 0.16. The described ceiling parameters are represented as well describing the limits of Spyro in the altitude direction. Ultimately the velocity boundaries are enveloped by the stall boundary lower limit and maximum velocity upper limit in the velocity direction, and the absolute ceiling boundary in

the altitude direction.

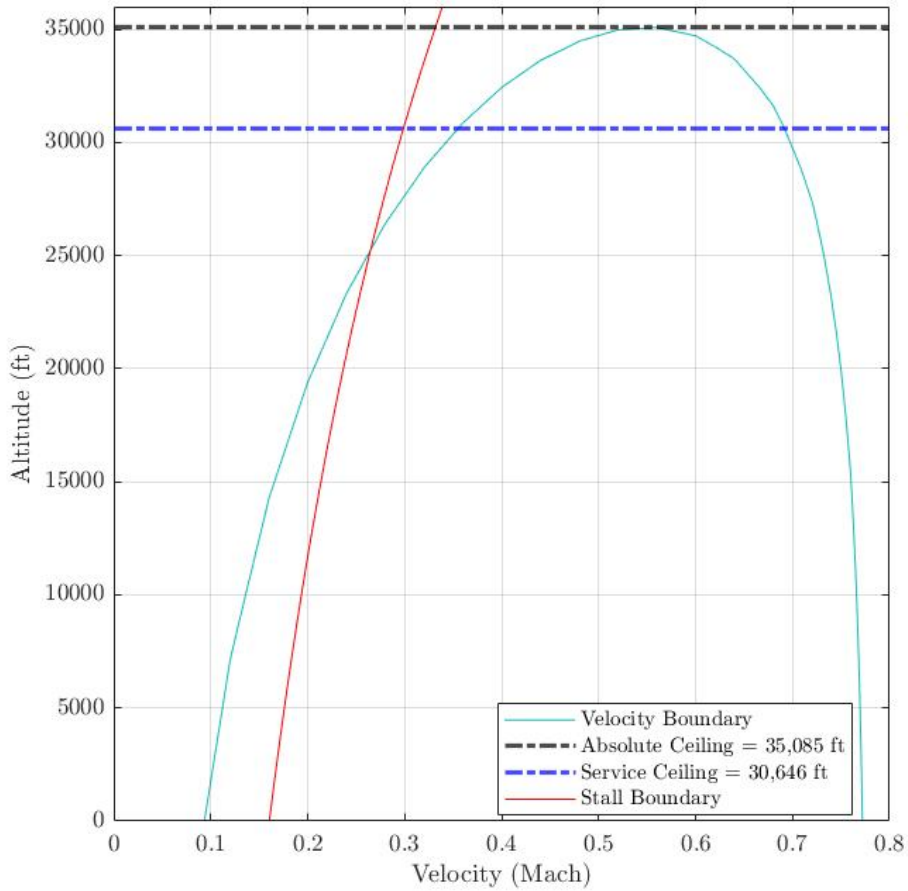


Fig. 37 Flight Envelope at MTOW

H. Drag For Each Segment

The drag break down is provided below for each segment. It is important to note the larger amount of drag faced at the takeoff and landing segments due to the extended slotted flaps. Although the needed lift is generated by the extended flaps, this will ultimately provide a proportionally greater increase in drag as shown. The increased drag is also needed for the landing segment in order to slow Spyro to rest. The provided drag results are the maximum felt by the aircraft during the corresponding segments.

Table 19 Drag Buildup for Individual Segments

Segment	Takeoff	Climb	Cruise	Descent	Loiter	Approach	Landing
C_D	0.054	0.052	0.035	0.042	0.046	1.03	0.26
C_L	1.21	0.837	0.465	0.563	0.637	1.491	1.21
Drag [lbf]	2,007	1,927	746	679	841	7,559	1,933

I. Payload Investigation

From the RFP and initial sizing, the maximum payload for Spyro will be stated as 3,000 lbs. This payload capacity includes the ordinance placed on the aircraft in the form of bombs and missiles. Using the weight at MTOW, the range performance of Spyro can be provided as a relation of payload capacity. The range in this simulation is computed using the Breguet range equation listed in chapter 3 of Raymer [10] and shown for 100%, 60% payload, and 0% payload capacities. The Breguet range equation will serve as an approximation of the more in-depth time step integration done for the fuel requirement investigation. The designed ferry mission range is described as 900 nmi, where the maximum range of Spyro is calculated as 2,424 nmi at empty payload capacity. The computed range shows that Spyro is able to complete the necessary missions in the design and ferry mission profiles. Consequently, the endurance that can be studied for the purposes of the design mission can be found utilizing the Breguet Endurance equation found also in Chapter 3 of Raymer [10]. The maximum endurance, and thus loiter time, for Spyro was found to be 10.9 hours. Although the Breguet equations are accurate within a small tolerance, it is important to note that they are generally used for initial sizing and performance analysis using certain assumptions. The assumptions made in this process involve a constant L/D, specific fuel consumption, and velocity during the investigated segments. The payload range chart and payload vs. time on station diagram are shown in Figure 38 and 39.

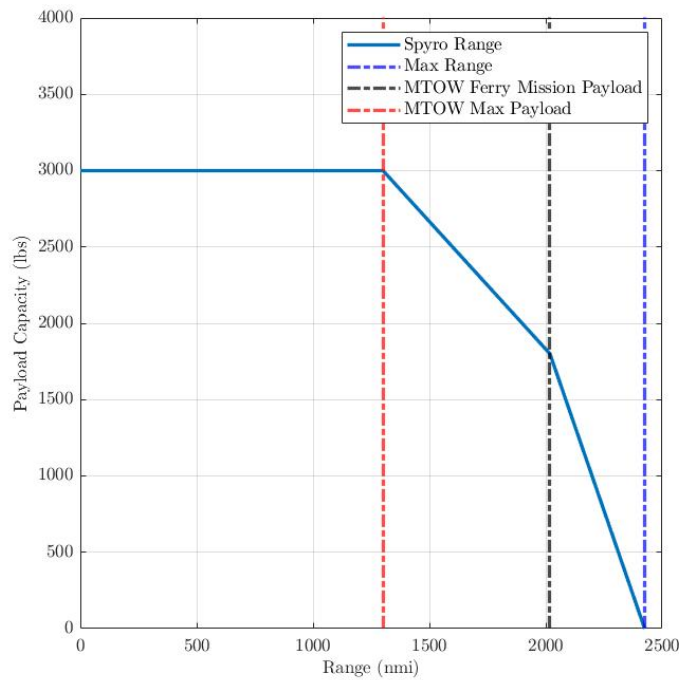


Fig. 38 Payload vs Range Diagram

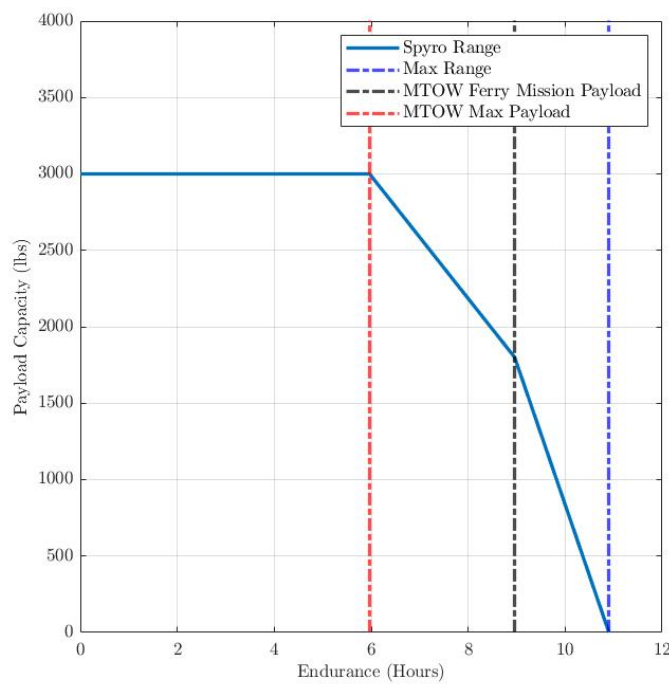


Fig. 39 Payload vs Time On Station

J. Fuel Requirements

1. Ferry Mission

The ferry mission will be conducted in the following simulation at 60% payload capacity. Each segment will be simulated with a time step integration and summed to reach the ultimate fuel requirements. The simulation will be iterated to find the minimum fuel requirement necessary to complete the designed ferry mission with zero fuel remaining after reserves. It is clear from this simulation that Spyro will be capable of satisfying the ferry mission. The cruise segment will be simulated at optimal cruise speed, Mach 0.49. It is important to note the range of 1,043 nmi traveled over the course of the ferry mission. The fuel requirement figure below will follow the mission profile as provided in Section II.B corresponding to the segment numbers.

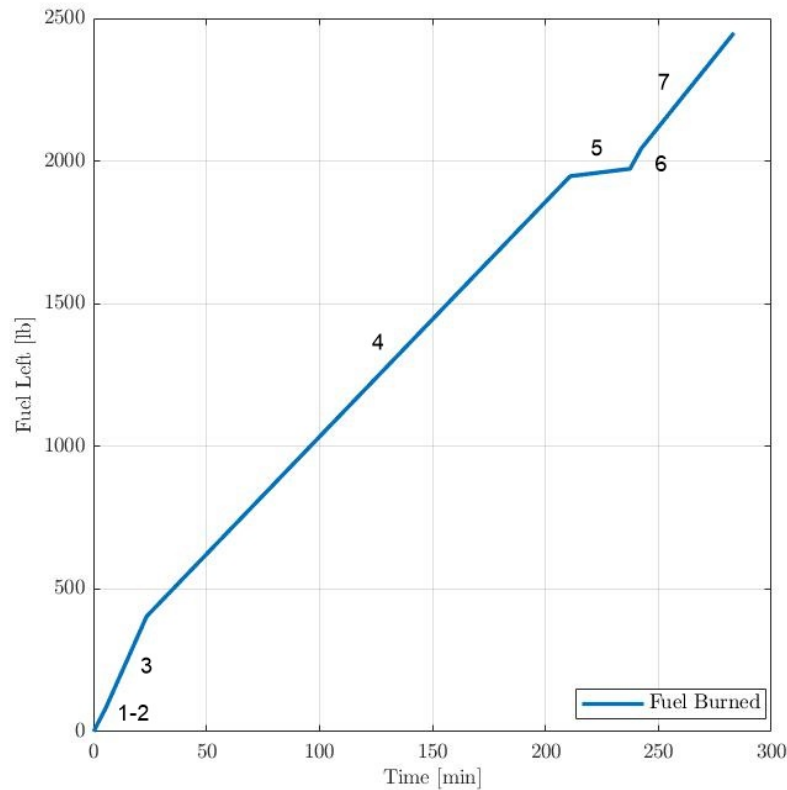


Fig. 40 Fuel Requirement with Time for Ferry Mission

2. Design Mission

For the design mission, it is necessary to complete the following simulation with the full capacity of 3,000 lbs. This will also be simulated in a time step fashion while satisfying the needed specifications for each segment. In contrast to the previous ferry mission, the design mission will be optimized in regard to the fuel burn for the loiter conditions as

described in Section VII.D. The cruise segments will once again be simulated at the most efficient cruise velocity and altitude in terms of fuel burned as well. It is clear that this mission is much more demanding for the aircraft than the initial ferry mission. Ultimately, over the course of all the design mission segments, Spyro uses 3,584 lbs of fuel while traveling a range of 960 nmi.

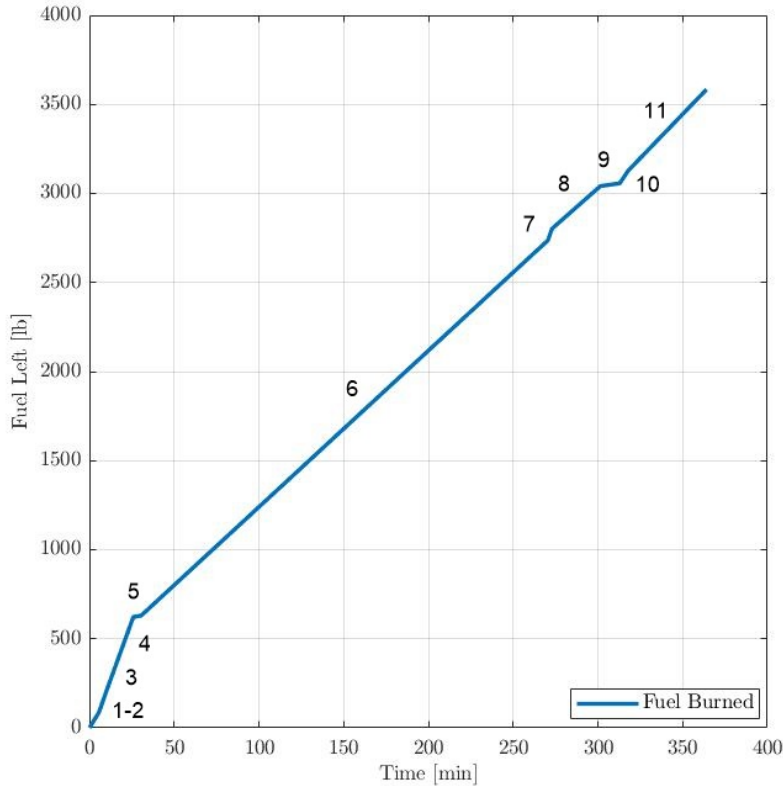


Fig. 41 Fuel Requirement with Time for Design Mission

K. Trade Studies

1. Optimizing Cruise Altitude and Velocity for Fuel Burn

The first trade study that is necessary to continue with the performance parameters includes an analysis of proper speed and altitude during the described mission segments. It is key to select the appropriate cruise altitude and velocity when simulating the mission fuel requirements to minimize the amount of fuel burned and therefore overall cost of the mission. Using the time step previously used to compute fuel requirements, a sweep through a range of altitudes and Mach numbers can suggest the appropriate cruise for each mission segment. This optimization of fuel burn over the ferry mission cruise segment will account for conditions at 60% payload capacity and the 900 nmi mission length for the ferry mission. A contour plot representing the fuel burned for each of the corresponding flight Mach numbers and

altitudes is as follows.

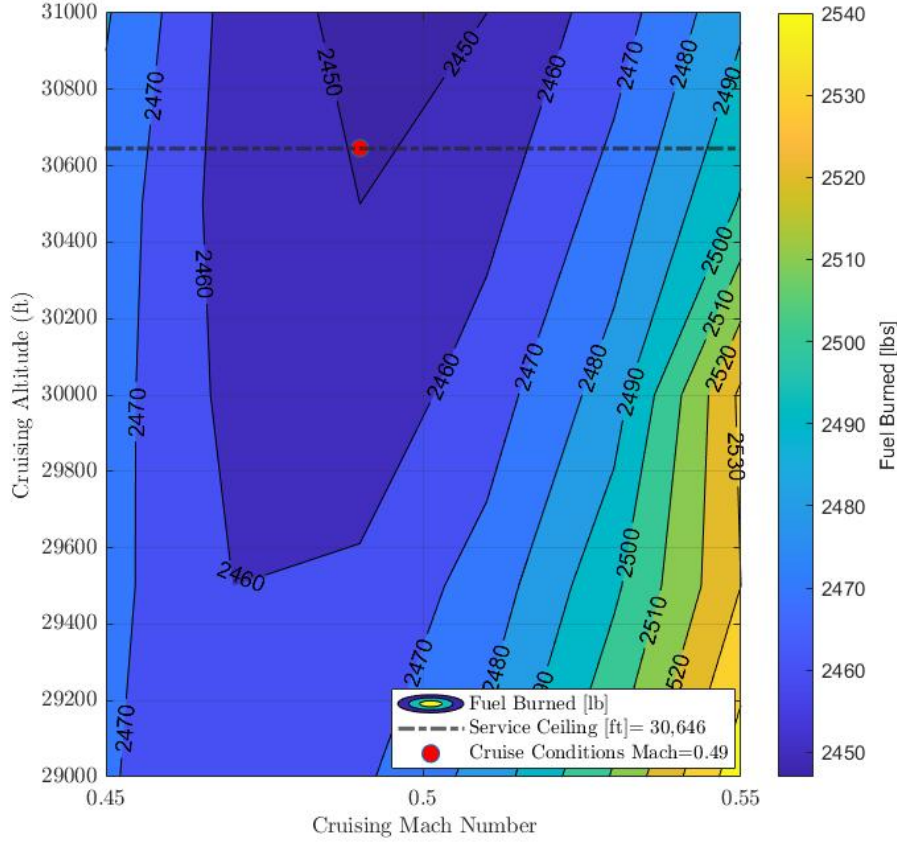


Fig. 42 Optimization of Cruise Conditions

Initially it is known that higher flight altitudes can reduce fuel burn over a given range distance. This is reflected well by the optimization results in Figure 42 as the fuel burned continues to decrease at higher altitudes. Therefore, the service ceiling at 30,646 ft can be chosen as an appropriate altitude to cruise at for the ferry mission. The shown Figure also proves the selection of the desired cruise velocity of Mach 0.49. For simulations done using cruise segments, these conditions will be chosen and used to optimize the fuel requirement of each segment. The non-linearity of the provided contours should be noted as the fuel burned is a result of the many time stepped factors throughout the course of the ferry mission. Around the selected conditions the fuel burned changes by small amounts but rapidly increase as the mach number varies from the optimal point. These cruise conditions can further be proved by the validation of best range speed. A range of Mach numbers can be swept through again at the selected service ceiling altitude to investigate the results of best range.

Additionally, the provided range vs mach diagram proves that the selected cruise conditions will not only optimize fuel burn, but also the range of the aircraft over the course of the 900 nmi ferry mission cruise segment. This trade

study will verify that the process for optimizing the flight conditions for Spyro during the provided missions has been analyzed holistically through various empirical and simulation methods.

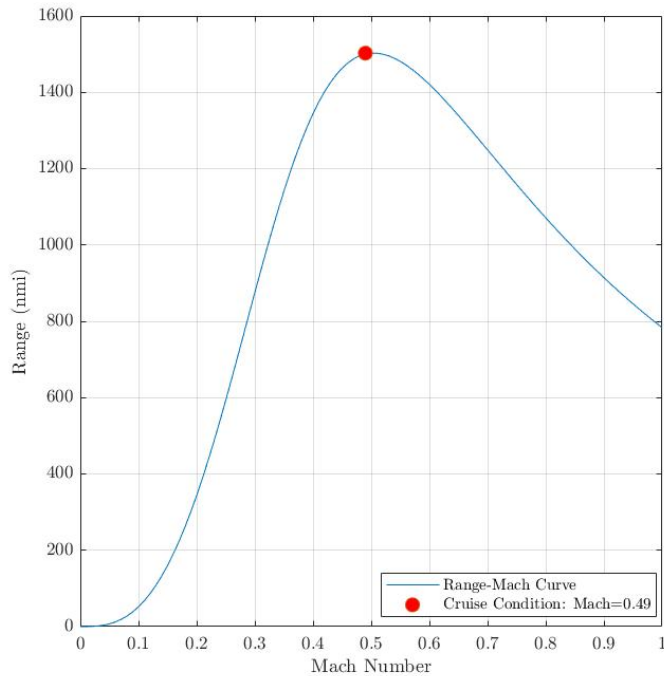


Fig. 43 Range vs. Mach Curve

2. Rate of Climb Analysis

Additional to the selection of cruise and loiter conditions, it is important to investigate the behavior between the main legs of the described missions. This investigation includes research into the rate of climb in comparison to other common seed light attack aircraft and attack helicopters. Initially, the rate of climb for Spyro is computed as a relation of excess power and weight. This method utilizes the well known rate of climb equation while correcting for the acceleration along the direction of the flight path angle. In the simulation for Spyro's design and ferry mission, the maximum rate of climb is generated as 3,266 ft/min while climbing to the cruising altitude in the ferry mission. This can be compared to similar light attack aircraft and attack helicopters to verify the rate of climb method selection.

Table 20 Various Aircraft and Rate of Climb

Aircraft	Super Tucano	OV-10 Bronco	Aero L-39	CASA C-101	Cessna A-37	Apache
ROC [ft/min]	3,230	3,020	4,100	4,900	6,990	2,800

After performing a trade study of various solutions to the light attack aircraft, it can be seen that the computed

3,266 ft/min rate of climb in the time step simulation will fall well within the range of rate of climbs of accepted aircraft. It should be noted that Spyro will climb at larger rates than the studied turboprop aircraft (Super Tucano and OV-10 Bronco), and similar to the turbo fan aircraft (Aero L-39 and CASA C-101) with the capability of climbing at a maximum rate just below the Cessna A-37 turbojet aircraft. The maximum rate of climb of Spyro at low altitudes can be seen from the specific excess power chart, Figure 31, as 5,400 ft/s. The large rate of climbs available from turbofan engines as represented in Spyro's capability provide a maneuverability that is very favorable in combat situations like the light attack mission calls for.

VIII. Stability and Control

A. Stabilizer Design

For this design, it was decided that a conventional tail configuration would be used. This configuration is the most common tail arrangement on any aircraft and is predictably stable. Other tail configurations such a cruciform, V, Y, and T tail were also considered, but due to the high weight of these tails, higher manufacturing cost, and the added weight near the tail of the aircraft due to the aft engine configuration, it was decided that using the lighter conventional tail would be optimal for Spyro in terms of stability and weight distribution.

Traditionally, symmetric airfoils are used on aircraft tails so the stabilizers have the same behavior for both positive and negative angles of attack. At zero angle of attack, symmetric airfoils also exhibit no lift, which is useful at cruise. The following trade study was conducted comparing the drag of symmetric airfoils of varying thickness to determine which is best suited for the design missions. C_{D0} was calculated using the methods outlined in Section VI.

Table 21 Trade Study on Tail Airfoil Selection

Airfoil	C_{D0}
NACA 0009	0.02
NACA 0012	0.03
NACA 0015	0.03
NACA 0018	0.04

Based on the trade study above, it was decided that the NACA 0009 symmetric airfoil would be used for both the horizontal and vertical tail. A thinner airfoil was selected to decrease aerodynamic drag, which overcame the effects of increased structural weight.

One trade study concerning both stability/ control and mass property is the tail sizing. In order to size the tail properly, a scissor plot is obtained from two conditions: take off rotation which yields the forward CG limit and cruise

stability which determines the aft CG limit. The generated scissor plot is presented in Figure 44. The given stabilizer size allows certain CG travel between two boundary conditions defined between the two slopes representing conditions mentioned above. Currently, the wing placement lands the CG fore and aft limits at 20.5% and 34.1% MAC. The aft CG limit at an S_H/S_W of 0.36. Spyro is equipped with a horizontal stabilizer that is sufficient at ensuring the longitude stability at most situation.

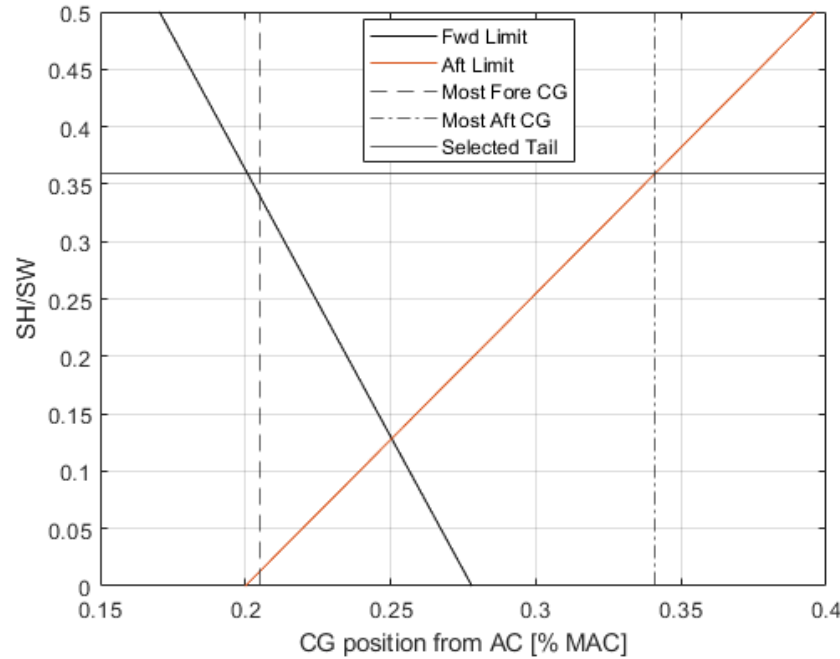


Fig. 44 Scissor Plot

The tail sizing parameters are presented in Table 22 and presented in Figures 45 and 46. It is worth noting that, typically, a horizontal tail's incidence angle is between 2 and 3 degrees [10], so the upper margin of this range was selected to aid stability of the aircraft.

Table 22 Horizontal and Vertical Tail Parameters

Parameter	Horizontal Tail	Vertical Tail
b	20.26 ft	8.48 ft
S	65.05 ft ²	31.97 ft ²
c_{root}	4.46 ft	5.83 ft
c_{tip}	3.34 ft	1.74 ft
$\Lambda_{c/4}$	8 deg	26 deg
LE Location	31.44 ft	30.07 ft
Volume coefficient	0.70	0.06
Incidence Angle	3 deg	2.5 deg

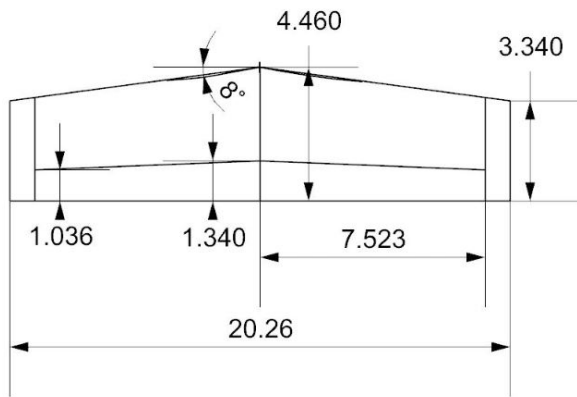


Fig. 45 Horizontal Stabilizer Diagram

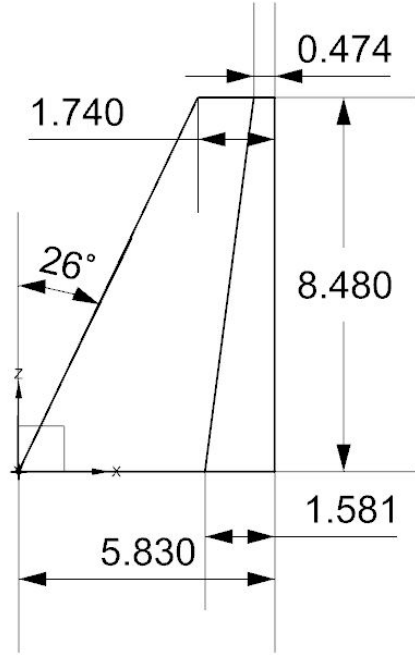


Fig. 46 Vertical Stabilizer Diagram

B. Control Surfaces

Control surfaces for Spyro were sized based on historical relationships between wing and tail size as well as historical values presented in Raymer [10]. Sizing data for the flaps ailerons, rudder, and elevators are presented in Table 23. Spans are presented as the span of a single control surface. Dimensions for the flaps and ailerons are presented visually in Figure 26 in Section VI while the dimensions of the elevators and rudder are presented in the Figures 45 and 46, respectively.

Table 23 Control Surface Parameters

Parameter	Elevator	Rudder	Aileron	Flap
Chord Ratio	0.33	0.33	0.25	0.25
Span Ratio	0.9	1.0	0.35	0.65
MAC	4.052 ft	2.045 ft	4.338 ft	6.284 ft
Span	7.524 ft	8.48 ft	6.64 ft	11.04 ft
Deflection Range	$\pm 20^\circ$	$\pm 20^\circ$	$\pm 25^\circ$	$-15^\circ, +40^\circ$

C. Trim Analysis

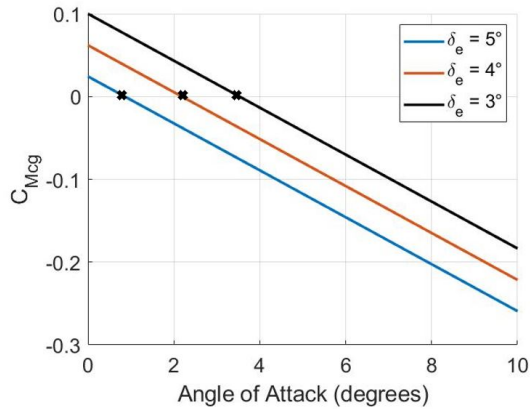


Fig. 47 Trim Diagram for Landing

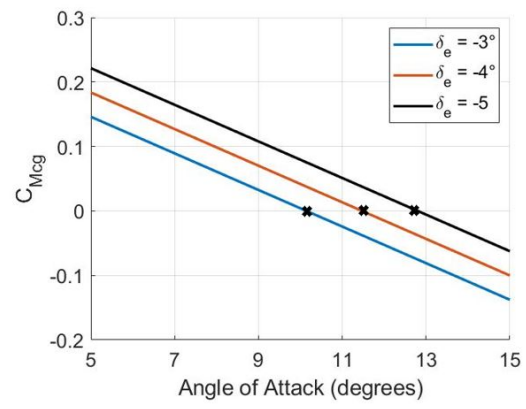


Fig. 48 Trim Diagram for Takeoff

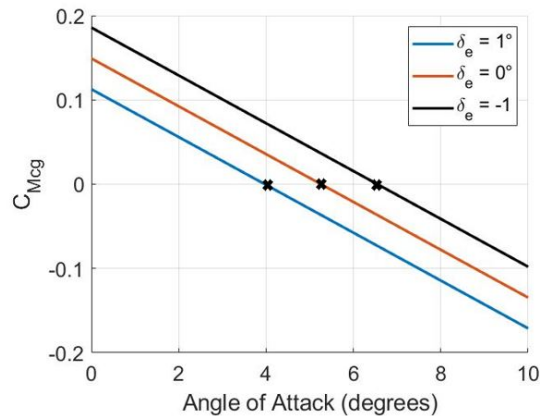


Fig. 49 Trim Diagram for Cruise

Trim analysis is performed to find the points of equilibrium where the moment of inertia about the center of gravity is zero. This analysis was done using a simulation in AVL, a vortex lattice method. The aircraft was trimmed by constraining the angle of attack to an angle corresponding to a pitching moment equal to zero. These angles of attack correspond to the trim points marked on each trim diagram. An important note from this trim diagram is that the slope of each line is negative, which corresponds to a negative $C_{M\alpha}$. The implications of this negative value will be expanded upon in the next section.

D. Longitudinal Static Stability

For any aircraft to have longitudinal static stability, it must have a negative $C_{M\alpha}$. In other words, an aircraft must be able to produce a negative pitching moment that opposes changes in angle of attack. Using methods outlined in Raymer [10] and Roskam [11], as well as using the developed simulation in AVL, longitudinal stability control derivatives were found and are presented in Table 24.

Table 24 Longitudinal Stability Control Derivatives

Derivative	$C_{L\alpha}$	$C_{M\alpha}$	$C_{M,\delta e}$	ϵ_α
Value	6.1669	-1.6261	-1.9992	0.3526

In its current configuration, since $C_{M\alpha} < 0$, Spyro is longitudinally statically stable. The aircraft is able to maintain control with changes in angle of attack. Also worth noting is the negative value of $C_{M\delta e}$. This negative value suggests that a positive deflection of the elevator results in a counterbalancing pitching moment, further aiding stability.

Using equations and information presented in Raymer [10], the static margin and neutral point as well as the fore and aft center of gravity were calculated. The results of these calculations are presented below in Table 25, with each value presented as a percentage of the MAC. With the fore and aft CG's being ahead of the neutral point, this further confirms that Spyro is longitudinally statically stable.

Table 25 Center of Gravity, Neutral Point, and Static Margin

Parameter	Fore CG	Aft CG	Neutral Point	Static Margin
Value	20.5%	34.1%	47.5%	13.4%

E. Lateral-Directional Static Stability

Analyzing the static stability of Spyro also requires a look at lateral-directional static stability. Using the developed AVL simulation, the necessary stability derivatives to determine lateral-directional stability are presented in Table 26.

These values were confirmed using methods outlined in Roskam [11].

Table 26 Lateral-Directional Stability Control Derivatives

Derivative	$C_{l\beta}$	$C_{n\beta}$	C_{lr}	C_{nr}
Value	-0.0689	0.1704	0.0692	-0.1524

With $C_{l\beta}$ being negative, this suggests that there is a naturally restoring roll moment with changes in side-slip angle. Similarly, the positive $C_{n\beta}$ value suggests there is a naturally counteracting yaw moment with changes in side-slip angle. These derivatives, along with the signs of the other derivatives presented, prove Spyro to be lateral-directionally statically stable.

F. Stick-Free Stability

As will be described in Section XI.A, Spyro uses a fly-by-wire system to control each of the control surfaces. However, there is a possibility that, during combat, these systems could be damaged, and the aircraft will be required to rely on the control of the pilot, alone. Therefore, another important factor to look at in terms of the stability of Spyro is whether the aircraft remains stable while the pilot is not in direct control of the flight stick. To prove this, the hinge moments of each control surface must be analyzed. The hinge moments of Spyro are presented in Table 27. These values were found through AVL simulation. According to Roskam [11], since all four of these hinge moments are small numbers, this means that all four control surfaces hold steadily and stably in position without the pilot holding the stick. Therefore, Spyro exhibits stick-free stability. Another consequence of small hinge moments is the actuators in the hydraulic systems that move the control surfaces have minimal size since there is only a very small load being applied to them by the control surfaces.

Table 27 Hinge Moments

Control Surface	Flap	Aileron	Elevator	Rudder
Hinge Moment	-8.37×10^{-4}	-2.03×10^{-12}	3.59×10^{-4}	-3.45×10^{-12}

G. Dynamic Stability

Now that Spyro has proven to be statically stable, it is necessary to see whether it is dynamically stable. This analysis can begin by taking a look at the roll time for Spyro to roll from an angle of -45° to 45° . According to Raymer [10], this maneuver must be completed by fighter aircraft in under 1.4 seconds. Using equations presented in Roskam [11], it was determined that Spyro has a roll time of 1.23 seconds, which is under the maximum time of 1.4 seconds.

Since Spyro is a single-engine aircraft, there is no "one-engine inoperative" condition. However, directional stability

can still be analyzed by calculating rudder trim for takeoff and landing conditions with a side-slip angle of 11.5° , a 20% speed crosswind, and at maximum takeoff weight. Rudder trim was found using the developed AVL simulation. The results of this analysis are presented in Table 28. Since both rudder deflection angles are within the specified deflection range of 20° , Spyro is directionally stable.

Table 28 Rudder Trim

Segment	δr
Takeoff	14.93°
Landing	14.91°

Additionally, further analysis on longitudinal and lateral-directional dynamic stability could be completed. Using the developed AVL simulation as well as methods outlined in Roskam [11], the data presented in Tables 29 and 30 was found. Based on all of the parameters following the requirements set forth my Roskam [11] for fighter aircraft, along with adequate roll time and rudder trim angles, Spyro is confirmed to be dynamically stable.

Table 29 Longitudinal Dynamic Stability Analysis

Mode	Required ω_n	ω_n	Required ζ	ζ
Short Period	$0.35 < \omega_n < 0.7$	0.482 rad/s	$0.3 < \zeta < 2.0$	0.528
Phugoid	N/A	0.0887 rad/s	$\zeta > 0.04$	0.604

Table 30 Lateral-Directional Dynamic Stability Analysis

	Dutch Roll ω_n	Dutch Roll ζ	Roll τ_R	Spiral T_2
Requirement	$\omega_n > 1$	$\zeta > 0.19$	$\tau_R < 1.4$	$T_2 > 12$
Parameters	3.354 rad/s	0.239	0.603 s	16.89 s

IX. Structures and Loads

A. Aircraft Loads Analysis

1. V-n Diagram

To understand the aircraft maneuver envelope and structural limits of the design, a V-n maneuver diagram and a V-n gust diagram were plotted using methods and constraints outlined in Chapter 12 of Roskam [18]. The analysis helps to determine the maximum load factor, given in multiples of the standard gravity, experienced by the design during

maneuvering and cruising in both clear and gusty air, as is shown in Figure 50. Military V-n diagram complies with MIL-A-8860B [19] and MIL-A-8861B [20] which specifies aircraft weight with normal payload and 40% fuel. An additional V-n diagram with maximum ramp weight is drawn in Figure 51

It is observed that gusts do not have any significant impacts to the performance of proposed design, and all designed cruise and maneuver conditions fall within a viable maneuver envelope, further suggesting validity of the proposed design. Maximum positive and negative load limits are chosen to be 7.33g and -3g respectively, as stated in Roskam Table 12.1 [18].

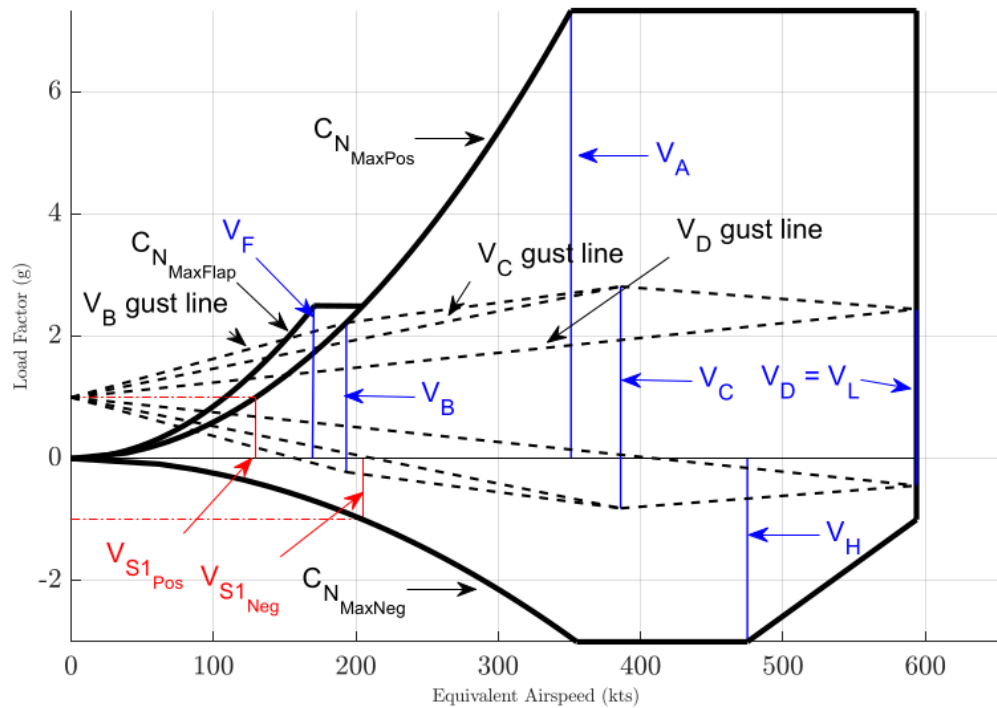


Fig. 50 Combined Military and FAR-25 V-N Diagram at Fight Design Gross Weight

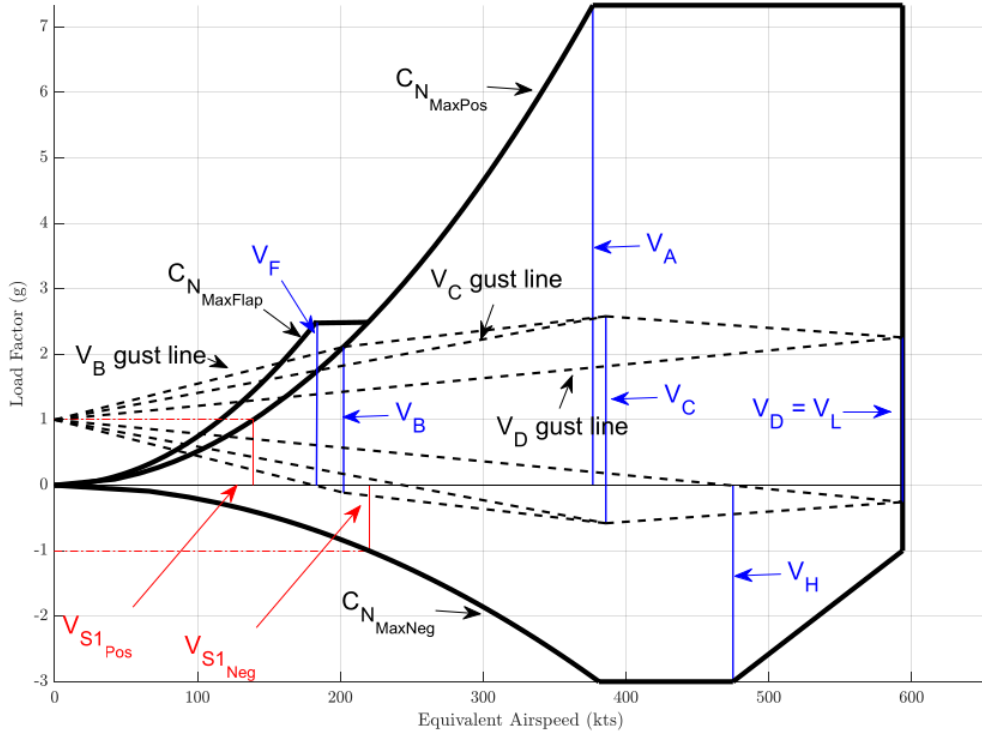


Fig. 51 Combined Military and FAR-25 V-N Diagram at Maximum Design Gross Weight

2. Maneuverability and Load

The maneuverability of proposed design is characterized using energy maneuverability theory by Boyd and Christie [21]. The method describes kinetic and potential energies of aircraft using their relationship with design parameters such as weight, thrust, drag and wing area. This study is conducted using the framework constructed by Nordlund [22]. Comparison between the maneuverability of proposed design and some seed aircraft in the initial sizing process are shown in Figure 52. The line in the middle of the envelope for each design represents threshold for constant turn conditions, below which the designs are capable of maneuvering with no loss in specific excess power. It was observed that Spyro, though having a smaller maneuvering envelope in the low-speed regime compared to seed aircraft, does have a better maneuverability in middle to high velocity flight condition. This is characterized by zero specific excess power contour of Spyro, marked in blue, is significantly larger than that of L-39, marked in black.

To better characterize maneuverability of Spyro, an energy maneuverability plot of the design at maximum ramp weight and designed loiter condition is shown in Figure 53. The figure is also annotated for clarity.

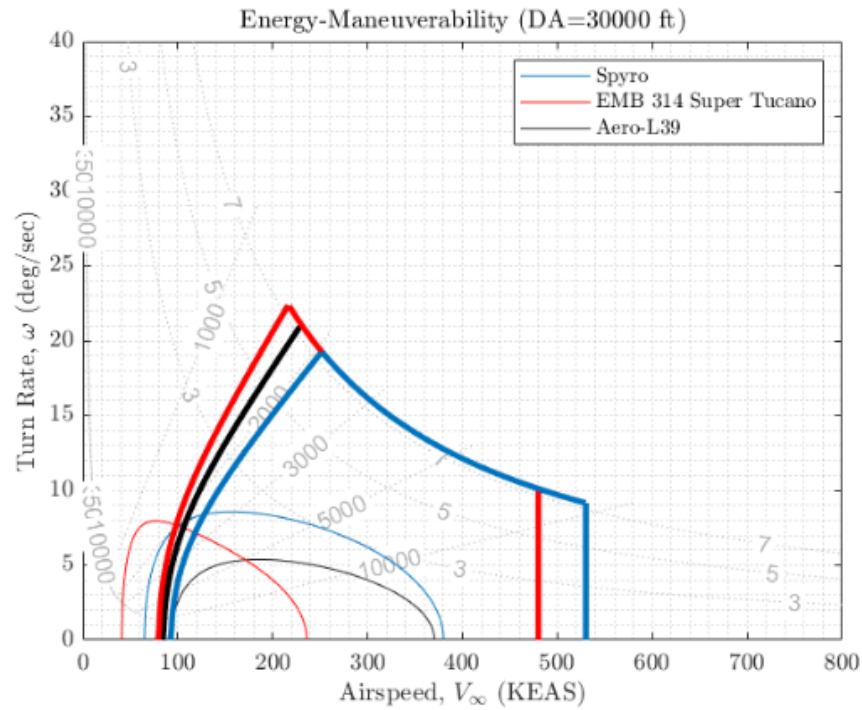


Fig. 52 Energy Maneuverability of Spyro, Aero-L39, and EMB-314

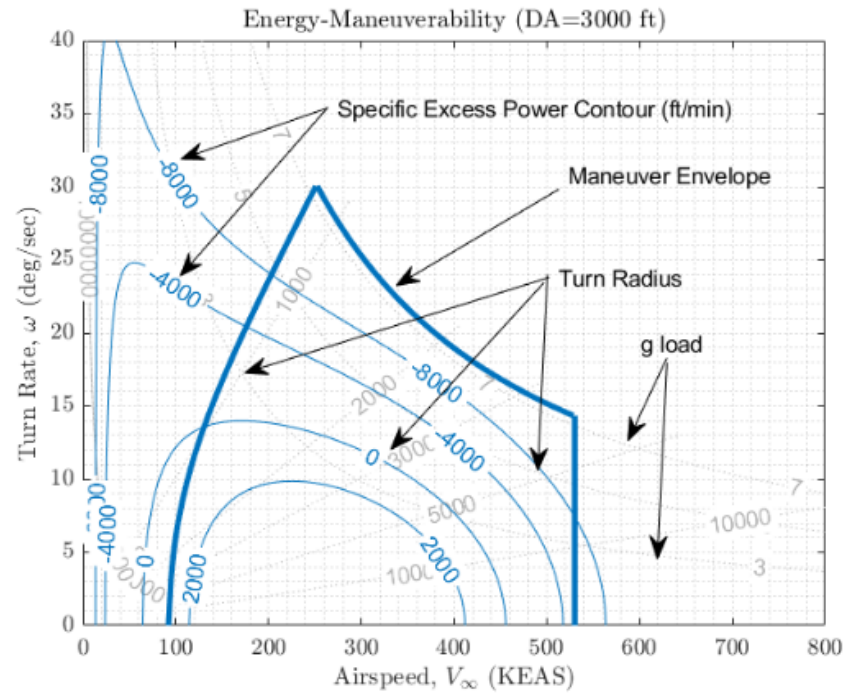


Fig. 53 Energy Maneuverability of Spyro at MTOW, Loiter Condition

3. Load Cases and Load Paths

Two load cases are considered for load estimation of the design. Figure 54 presents a simplified case for loading of aircraft at static condition, and a more demanding case of the aircraft performing high lift maneuver on the boundary of the allowed flight shown in the V-n diagram in Section IX.A.1. The latter case was used for determining maximum load experienced by the airplane, which serves as an objective in structural design and optimization detailed in Section IX.B, and the wing loading estimation of the specific case of interest is presented in Section IX.D.1. Load paths are drawn such that loads are exerted on the aircraft skin, which is carried to wing-fuselage junction via internal reinforcement such as ribs, spars, bulkheads, etc.. Load paths are shown in Figure 54, and a visual representation of the load paths are shown in Figure 55. Pressurization will be applied to the cockpit only using bleed air from the engine compressor. The maximum pressure difference at 23,000 ft cruise condition will be 8.26 psi, assuming an interior pressure of 10.92 psi identical to absolute pressure at 8,000 ft. Above the mentioned altitude, a pressure difference of 5 psi will be implemented for safety measures. Pressurization forces travel from the cockpit to stingers and longerons via inner skin and canopy.

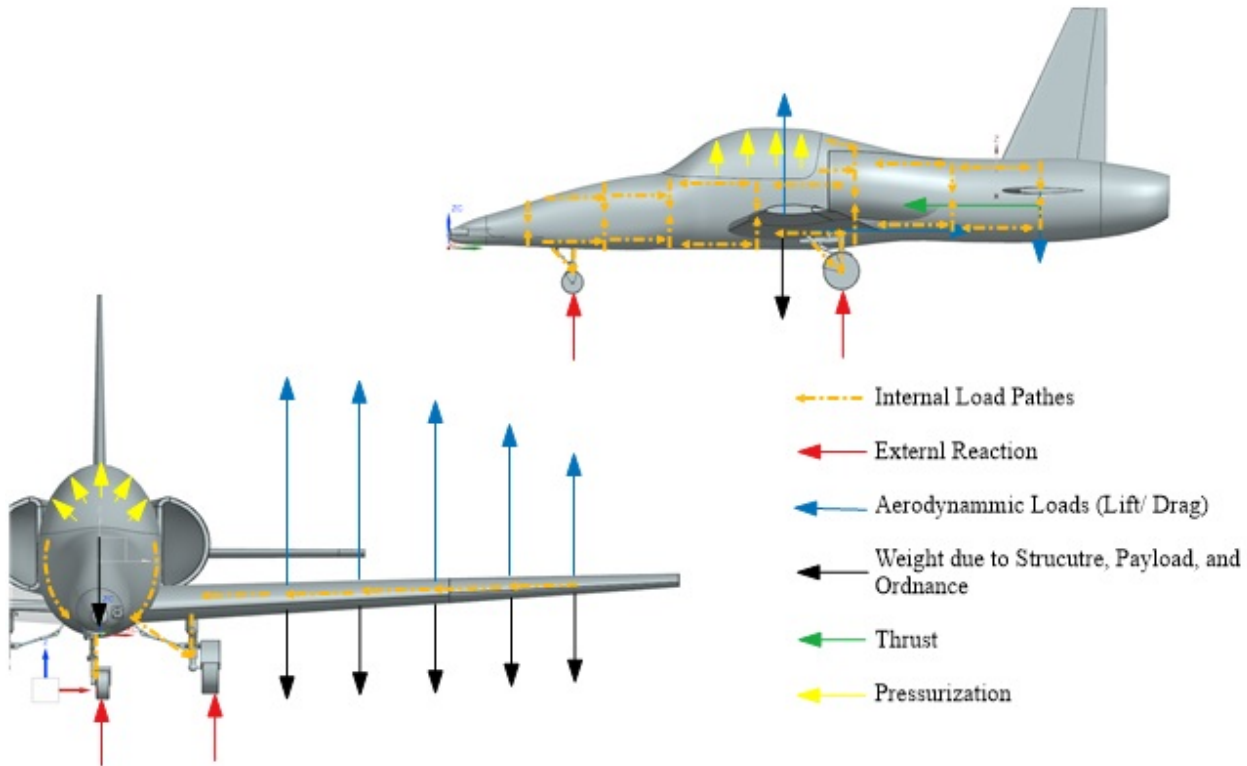


Fig. 54 Load Paths of Aircraft in Static Condition

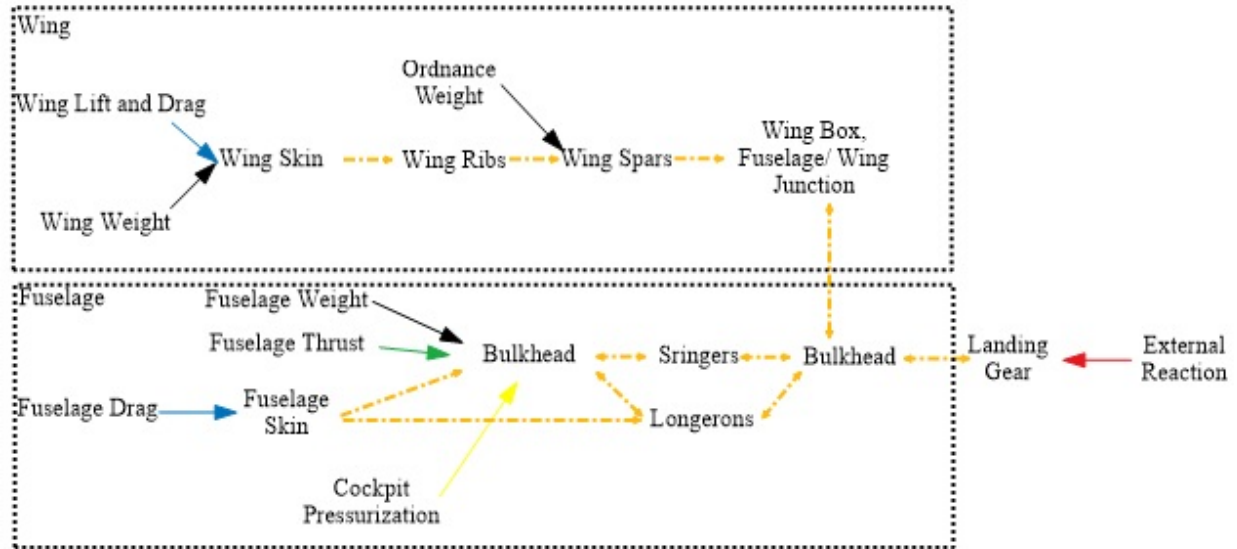


Fig. 55 Block Diagram of Load Transfer

The qualitative analysis presented in Figure 54 and Figure 55 suggests that heavier reinforcement has to be placed around wing box and landing gear as all weight related loads traverse these structures. Larger stringers and longerons should also be implemented above the wing box at the rear side of canopy to prevent bending caused by heavy components placed at the rear of the aircraft such as engines, fuel system and stabilizers.

To further understand the stress concentration along the structures of Spyro, a finite element analysis is conducted using ANSYS Mechanical with weight specification detailed in Section X. and landing gear placement explained in Section IV. B. For this particular study, a solid fuselage is used while various loads are modeled as forces in respective positions, and landing gear placement as well as respective wing boxes are modeled as fixed supports. A visualization of the problem set up is shown as in Figure 56. Solution of the problem of interest is presented in terms of stress, as in Figure 57.

It is observed that stress concentration occurs at the rear of the fuselage, mainly due to engine and stabilizer weight. The result of this study, accompanied with discussion of load paths at the start of this subsection, suggests that thicker reinforcement should be placed at the wing-fuselage junction, as well as before engine placement to prevent tail bending under static conditions. The result also suggest the use of elliptical bulkheads in an attempt to reduce bending cost effectively. From the locations of stress concentration, longeron and stringer placement, can be determined such that denser placement of longitudinal support is required on the top and bottom surfaces of the fuselage. Lastly, it is encouraging to observe that the maximum stress is far below the maximum tensile strength of the chosen material, which will be discussed in section IX. B, thus further validating the result of trade study.

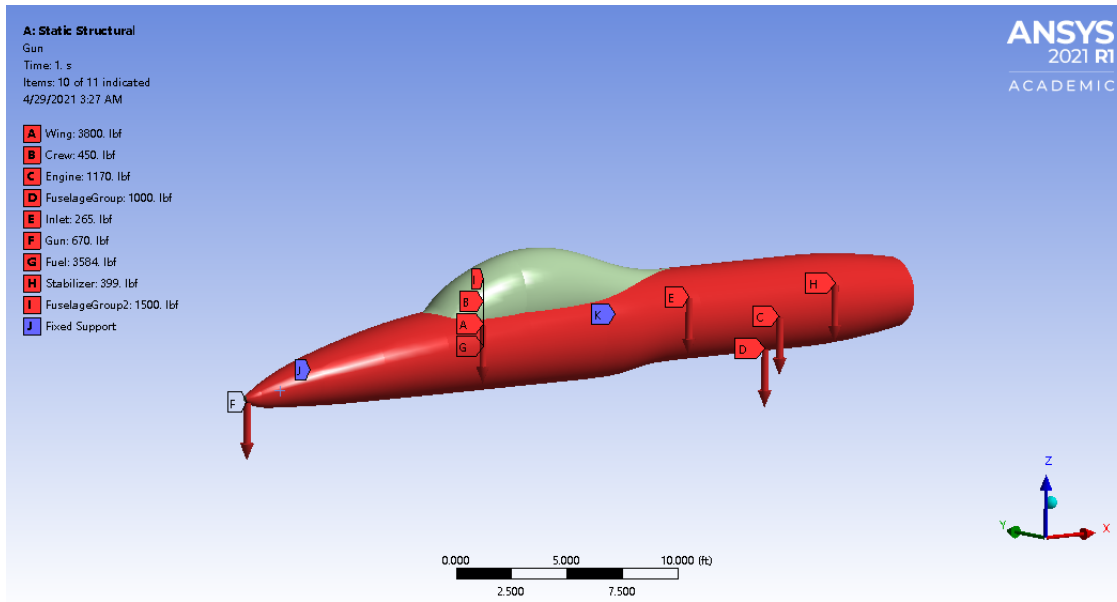


Fig. 56 Problem Setup of Investigation of Stress Concentration Along Fuselage

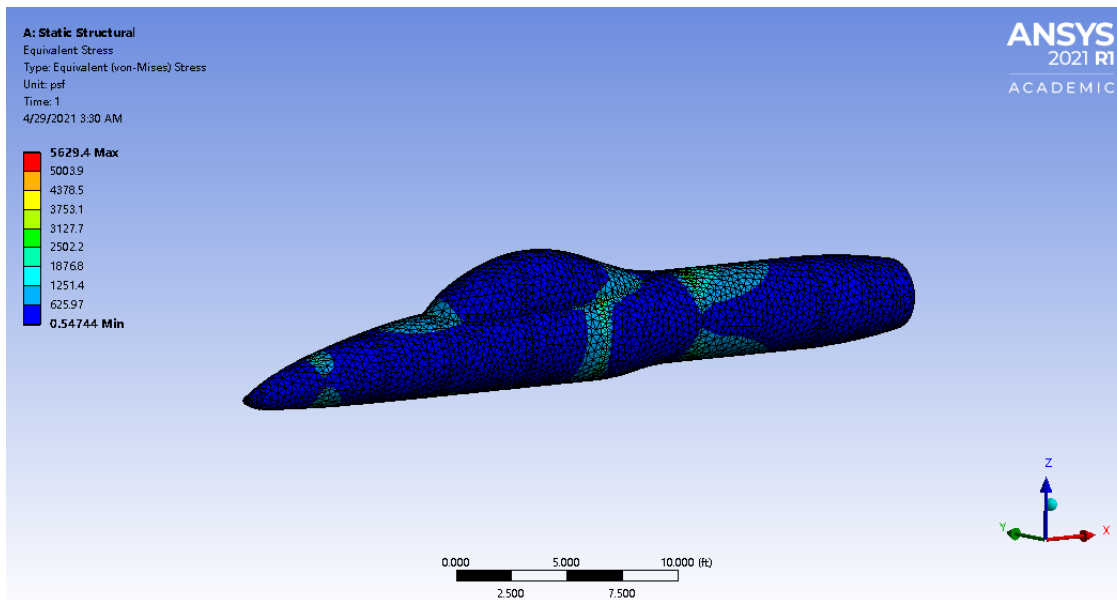


Fig. 57 Stress Concentration Along Fuselage

B. Structural Arrangement

A high level overview of the internal structural arrangement within Spyro is as follows:

- 1) Wing
 - 1) 4 main spars with additional stiffeners
 - 2) 20 ribs with lightening holes and tank cutouts [23]

- 3) Torsion box construction with full length spar caps
- 2) Fuselage
 - 1) 16 radially spaced primary longerons
 - 2) 18 primary frames, spaced based on 50% of the maximum structural depth
 - 3) Fore and Aft pressure bulkheads bounding the cabin

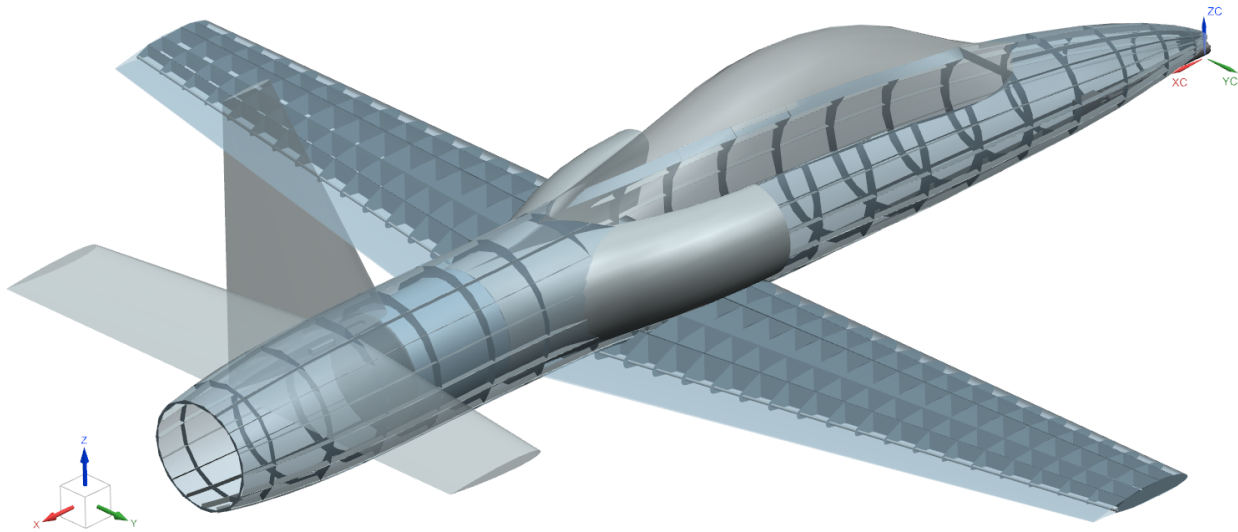


Fig. 58 View of the internal structures of Spyro, with skin transparency

C. Material Selection

Given the requirement for operation from short, austere fields near the front lines, the aircraft must be robust and easily repaired in the field [1]. Therefore the mission critical structural components of the aircraft must be composed of materials that are amenable to repair and maintenance in such austere environments and forward operating bases. Below in Table 33 are listed various attributes of material classes considered, and how they will interact with mission requirements.

From the decision matrix in Table 32, it can be determined that the primary structures of the aircraft should be made of metal, largely due to the greatly improved maintenance and repair characteristics of metals when compared to composites. As to which metallic elements and alloys will be chosen, a similar analysis involving repairability, cost, and material properties is found below where 3 is the highest score and 1 is the lowest score to be achieved in any given category.

A few aluminum alloys are listed in Table 31 for consideration. While the final design will not be constrained by the materials listed, current requirements for material selection as well as requirements for the design to be durable and economic would point to the choice of AL 6061, 7050, and 7068 [24] [25]. A trade study will be conducted to

determine the optimal portion and distribution of these materials within the aircraft.

Table 31 List of Aluminum Alloys Considered

Alloy	Density [lb/ft ³]	Young's Modulus [Msi]	UTS [ksi]	Note
AL 2014	175	11	70	Difficult to weld, corrosion resistance poor
AL 5052-H32	167	10.15	37	Non heat-treatable
AL 6061	169	9.86	42	Popular in light aircraft
AL 7050	175	11.6	75	Usually used on wing skin
AL 7068	178	10.6	93	Strongest known for low mass
AL 7075	175	10.4	83	Popular in WWII war planes

Given the requirement for operation from short, austere fields near the front lines, the aircraft must be robust and easily repaired in the field [1]. Punctures to the aircraft skin should not severely compromise the structural integrity of the aircraft, which discounts the use of a carbon or glass fiber composite skin. This also improves the repairability of the aircraft, given that fabrication of metal replacement parts requires significantly fewer specialized machine tools and processes than composite part fabrication requires. Additionally the choice of riveted metal skin improves access to the internal systems, further improving serviceability in the field.

Table 32 Metal Selection Figures of Merit

Attribute	Aluminum	Steel	Titanium
Structural Weight	2	1	3
Cost	3	3	1
Repairability	3	3	1
Availability	3	3	1
Score	11	10	6

Table 33 Material Selection Figures of Merit

Requirement	Metal	Composite
Damage Resistance	✓	
Structural Weight		✓
Aerodynamics		✓
Repair Cleanliness	✓	
Material Cost	✓	
Availability	✓	
Repair Cost	✓	
Repair Strength	✓	
Score	6	2

D. Structural Component Sizing

1. Wing

Knowing the maximum ramp weight and maximum load factor and the limits of the flight envelope, the main wing spar can be sized accordingly based on the shear forces, bending moments, and torsional forces experienced on it during maximum loading conditions. During a representative maximum acceleration turn, aerodynamic loads on the wing can be calculated by way of a discrete lifting line method, and then integrated to produce force and moment diagrams.

The wing planform was fed into the calculation, and a discrete horseshoe vortex method was run to calculate the total aerodynamic lift loads on the wing. Above in Figure 59 is a visualization of the maximum load case, and the lift forces acting on the wing.

The lift forces on the wing were lumped by spanwise coordinate, and used to produce a measure of local lift force per unit span as seen above in Figure 60 to be used in calculating the shear forces and bending moments present in the wing structure. Shear forces that must be reacted against inside the structure were calculated from the lift per span distribution.

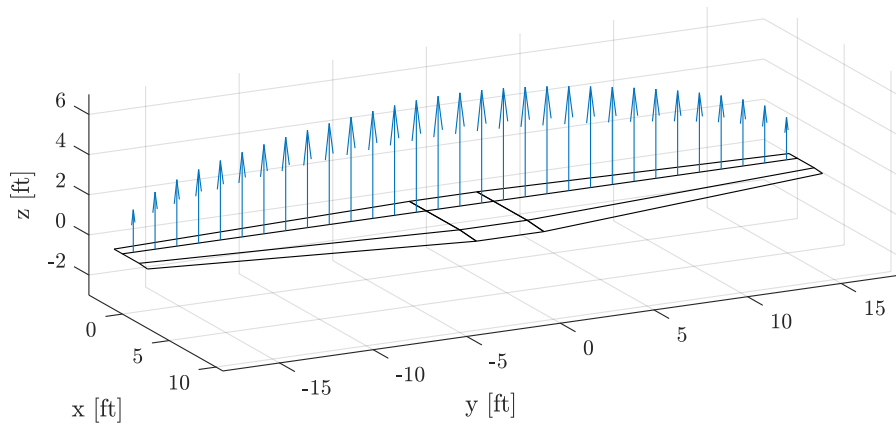


Fig. 59 Visualization of the calculated lift distribution at maximum total load

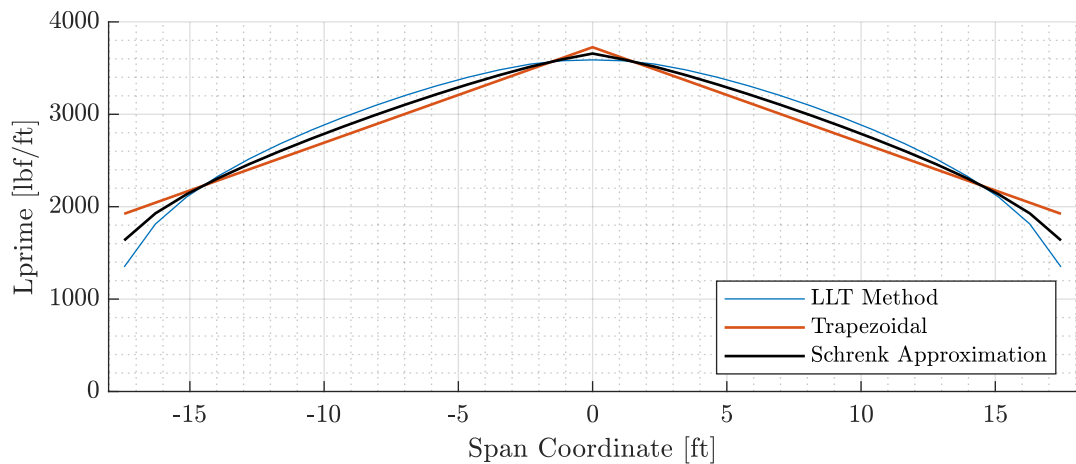


Fig. 60 Lift-per-unit-span along the wing

The bending moment due to the effect of lifting forces along the wingspan is in turn calculated by integrating the shear forces in the wing over the span, producing the bending torque that must be reacted against by the structure.

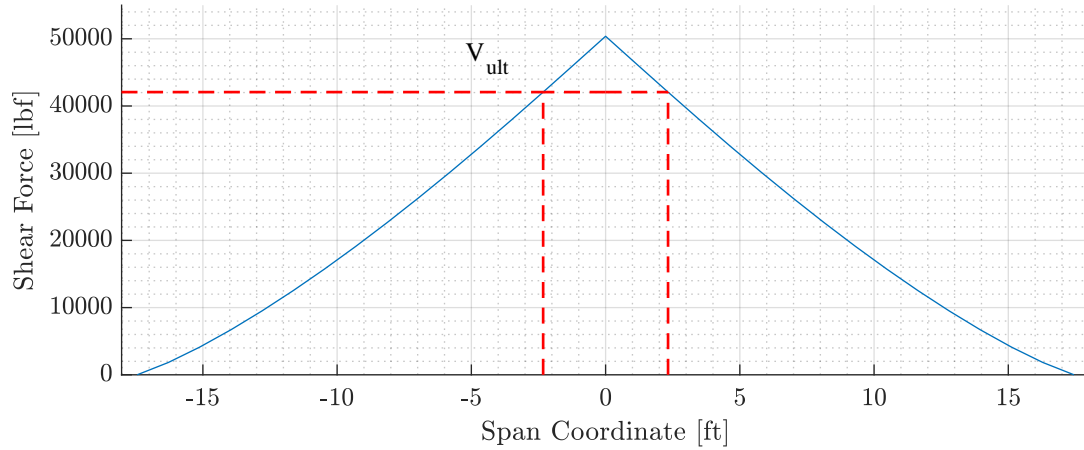


Fig. 61 Shear forces inside the wing structure

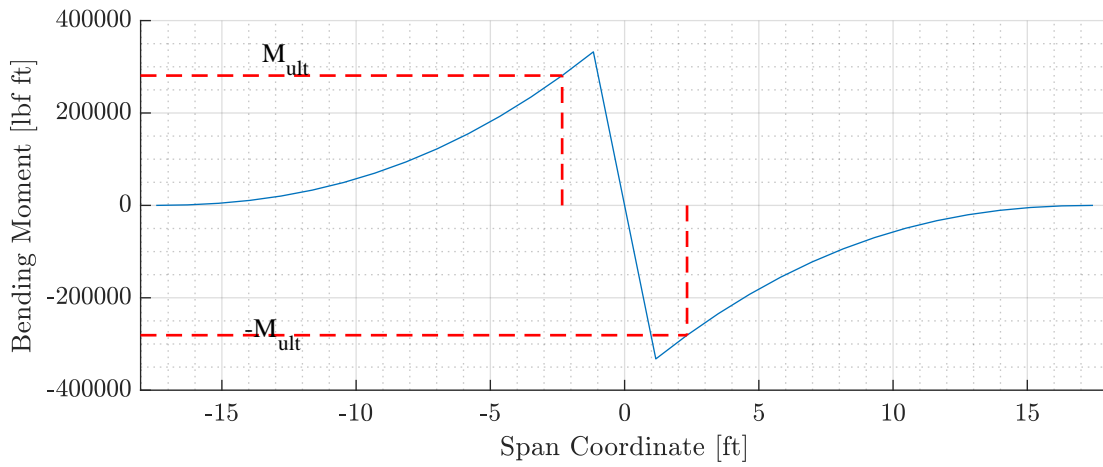


Fig. 62 Bending moments inside the wing structure

After the shear force and bending moment calculations are performed, initial wing spar sizing is possible. To close the problem, several assumptions must be made about which structural components carry certain types of stresses and how the aerodynamic loads are transferred to the spar, they are listed below and described in Howe [23]:

- Shear loads are carried by the spar webs
- Bending loads are carried by the spar caps
- Shear web height is determined by airfoil thickness
- Structural members have negligible sheet thickness

In order to calculate material thicknesses and dimensions required for each component of the wing spar, a maximum stress threshold must be chosen. Assuming a 40 ksi maximum strength in accordance with fatigue life information from [26] for Aluminum 7068, the load cases displayed in Figures 61 and 62, and the load path assumptions given immediately above, the wing spar weight can be calculated. The main shear web height was calculated based on the wing platform geometry and airfoil section height, from which a height of 12.84 in at the virtual wing root (platform centerline) and 4.94 in at the wingtips was determined.

Following the determination of the spar height, the minimal thickness distribution along the span was calculated from the maximum allowable stress and a structural safety factor of 15% on top of the maximum load case. Minimal shear web thicknesses at the virtual root and tip were determined to be 0.114 in and 0.03 in respectively, with additional stiffening present to account for buckling limits. Spar cap area was determined in a similar manner, by calculating the forces required to react against the bending moments present along the span of the wing given the structural thickness along the span. Assuming the width of each spar cap is half of the local wing spar thickness, the spar cap dimensions can be determined. This results in cap widths of 6.47 in at the virtual root and 2.47 in at the wingtips, along with thicknesses of 1.71 in at the virtual root and 0.08 in at the tips. The use of sandwich panel stiffening is suggested for the wingtips to reduce buckling risks due to the thin predicted structural thickness. The wing spar weight can be calculated by integrating the web and cap cross sectional thicknesses along the span, and multiplying by a material density of 168.6 lbm/ft³. A calculated spar weight of 358.1 lb is required to support the aircraft while performing a maximum load factor (7.33 g) turn at maximum takeoff weight.

2. *Empennage*

Similar calculations were performed for the horizontal tail, given the download required at the maximum forward-CG position to produce a counterbalancing moment to that which is created by the wing in the maximum load condition. Given a moment arm ratio of $\frac{3.42}{156.6}$ of the wing and horizontal tail aerodynamic centers relative to the maximum forward position of the center of mass, the horizontal tail must be designed to produce at least $\frac{3.42}{156.6} \cdot MTOW \cdot 7.33 = 4,374 \text{ lbf}$ of download to achieve the lift loads mentioned in the previous section.

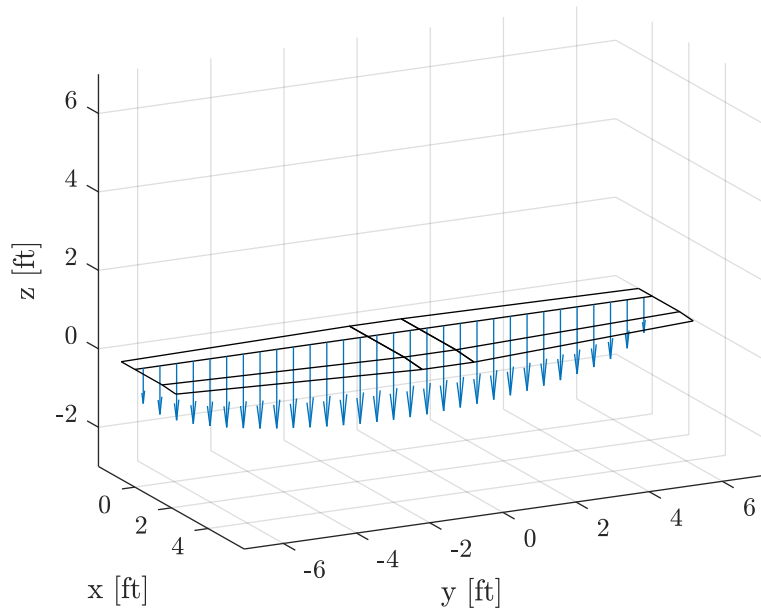


Fig. 63 Horizontal tail downloading in a max-load turn

An overall structural spar weight for the horizontal tail has been computed to be only 7.1 pounds, which suggests further finite element analysis will be needed to evaluate the plausibility of this value and correct it where needed.

3. Fuselage Forces

Now that the maximum wing lift and tail down-load forces are determined, a shear and bending analysis are also performed for the fuselage. Torsion loading due to roll is also analyzed.

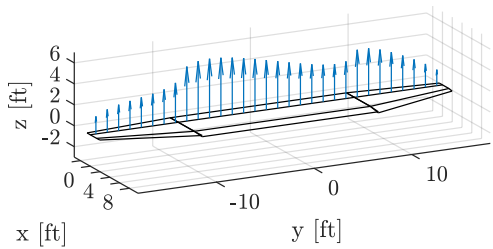


Fig. 64 Equilibrium 120°/s Roll-rate

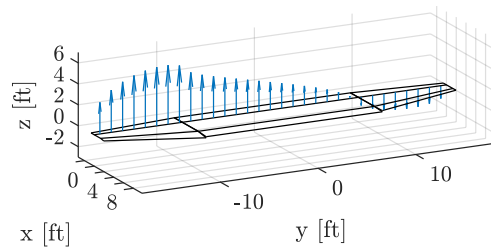


Fig. 65 Equilibrium roll with reversed controls

Producing a roll rate of 120 degrees per second at 300 knots requires a rolling moment on the wing of 79,600 lbf-ft, which if applied impulsively to the fuselage will produce a maximum torsional stress of near the same value at the wing-fuselage junction. If the reverse control input is applied to rapidly reverse the roll direction, while still rotating at the equilibrium rate of 120 degrees per second, the load limit is then doubled to 159,260 lbf-ft. The fuselage skin must be thick enough to withstand such a twisting load repeatedly, as the aircraft will be performing plenty of rapid rolls when involved in combat.

E. Wing Internal Structure

In an effort to increase structural redundancy, improving survivability in the event of severe battle damage to one of the spars, a four-spar torque box design was chosen. This is superior to the initial two-spar design in that the wing retains structural integrity even if one spar is completely split through at any span station. The local ribs will transmit the forces around the damaged area to the remaining three spars. The four spars have been located at the 0.15, 0.3, 0.5, and 0.65 chord stations, providing an even spatial distribution and maintaining the rear attachment points present in the original two-spar internal structure. In order to reduce spar cap buckling near the wing root, additional stiffening members have been installed at the 0.22 and 0.4 chord stations.

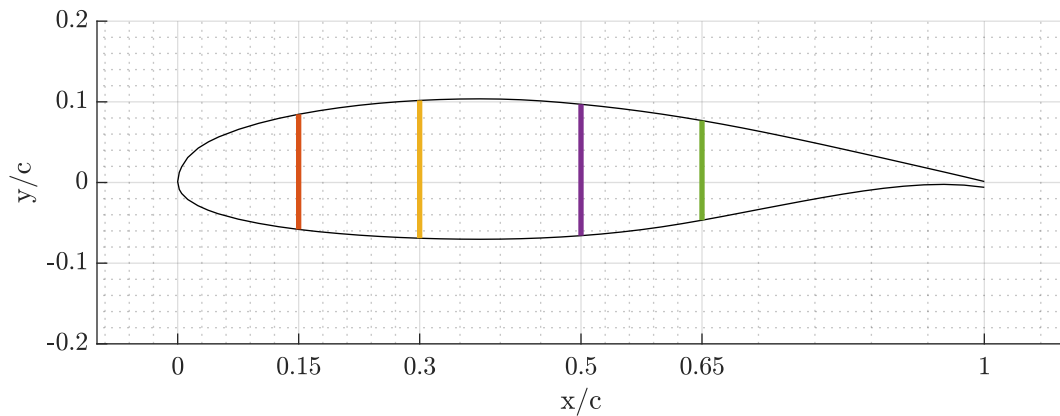


Fig. 66 Wing Spar Locations

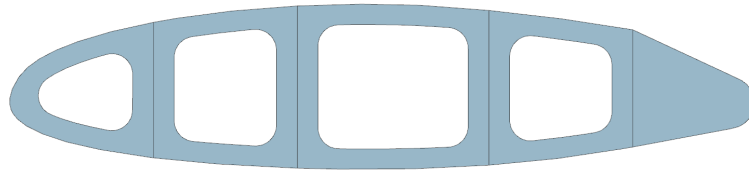


Fig. 67 Innermost Rib Outline with Tank Cutouts

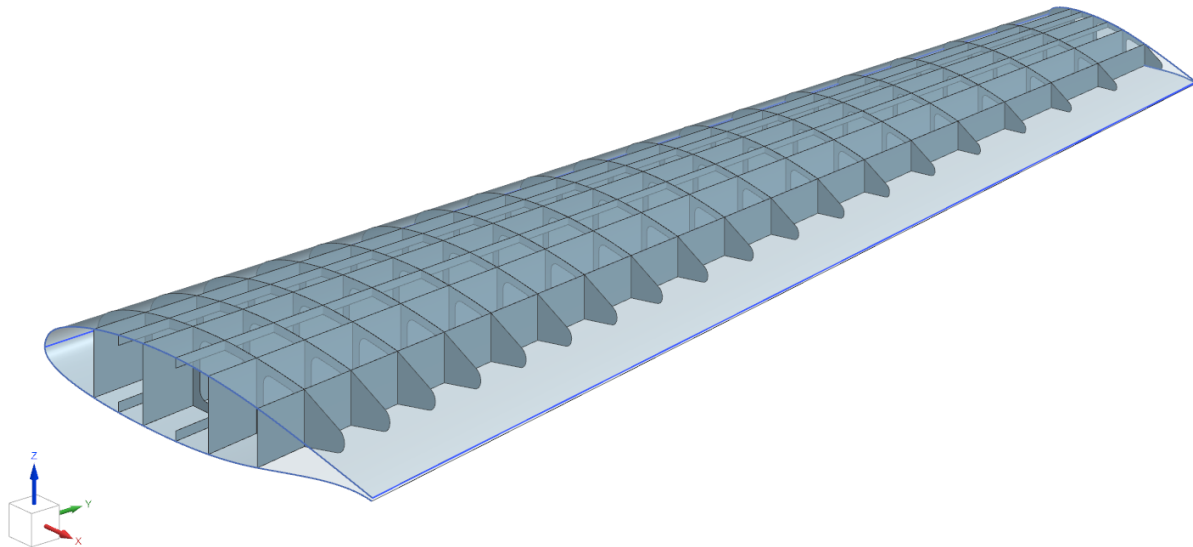


Fig. 68 Detailed Wing Structural Arrangement

F. Finite Element Analysis

With the limiting load conditions determined, and a detailed internal wing CAD model developed, finite element analysis can be performed to analyze the response of the wing structure to any given load case. In keeping with the aforementioned maximum loading case, the 7.33g turn, the loading to be applied to the structure model is as follows:

- 1) Mean Wing Loading: 460 lbf/ft²
- 2) Local LE Wing Loading: 920 lbf/ft²
- 3) Local TE Wing Loading: 0 lbf/ft²
- 4) Hingeline Load: 500 lbf on each rib extension

Skin wing loading was simulated as an outward normal pressure load on the upper surface, and hinge forces were distributed over each rib extension. The skin, spars, and stiffeners were given a fixed constraint at the wing root.

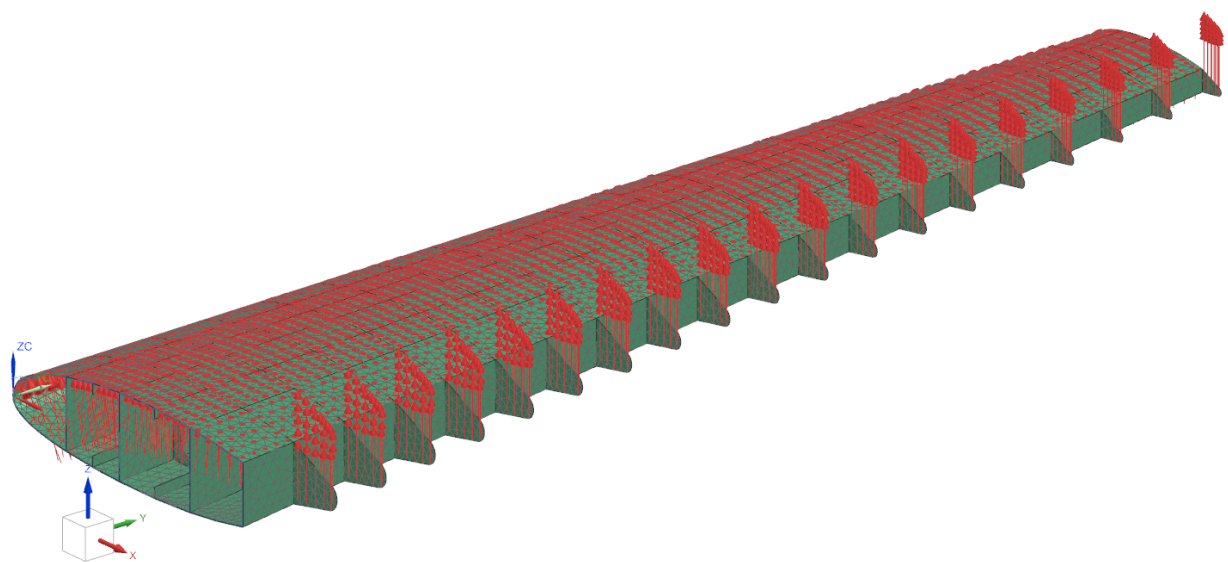


Fig. 69 Load Case used in the stress analysis

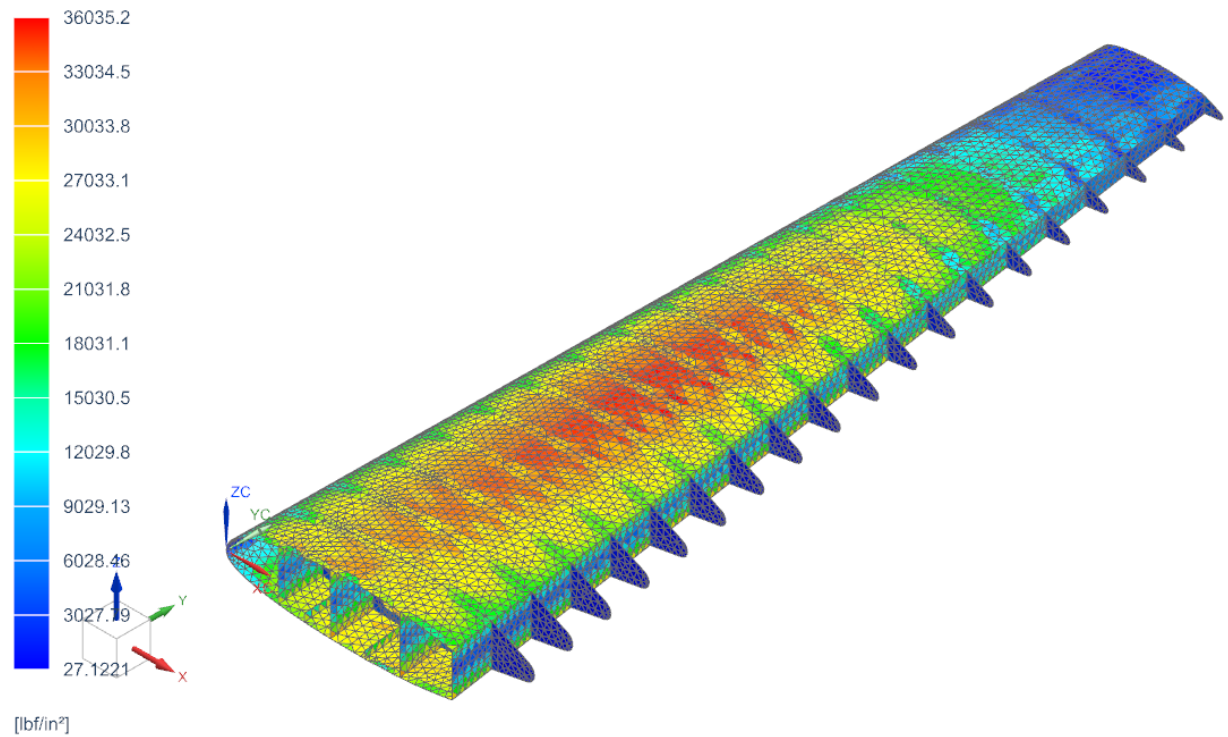


Fig. 70 Stress developed in the structure [psi]

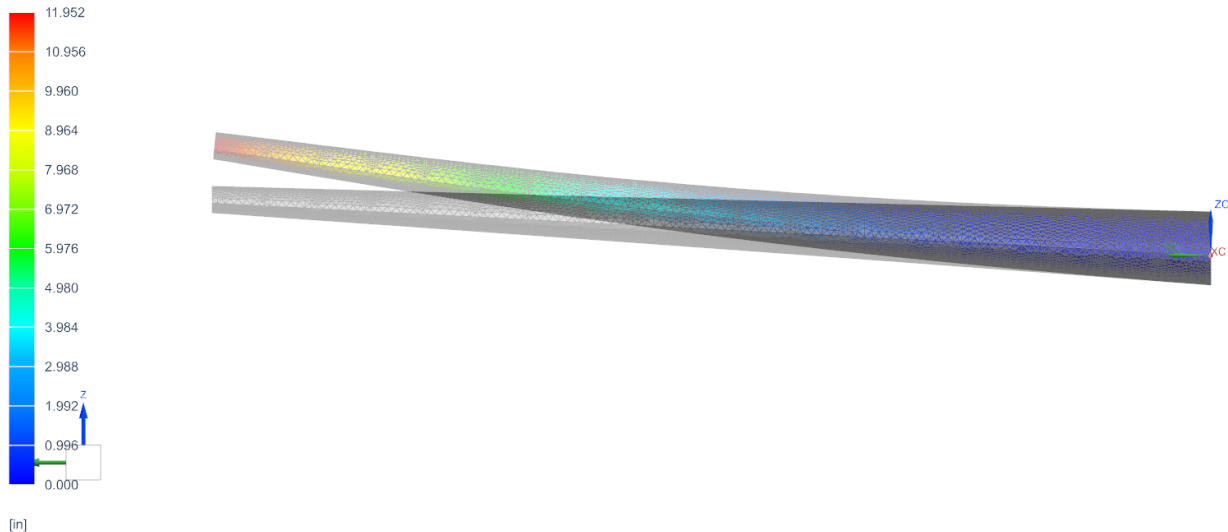


Fig. 71 Maximum Vertical Wingtip Displacement [in]

Several important conclusions can be drawn from the FEA results, chief among them being that the wing structure as-designed is capable of withstanding the forces applied to it during the maximum load case. The maximum stress developed in the structure is found on the upper spar cap as seen in Figure 70, and has a value of 36,000 psi, which is lower than the 40,000 psi limit assumed above in Section IX.C. Additionally, an approximation of the static aeroelastic properties of the wing structure can be inferred from the linear and angular displacements along the wing. The vertical displacement of the wing tip under maximum aerodynamic load is 11.9 in, which is not insignificant when taken alone. The maximum angular displacement at the wingtip is however very small, at only 0.3 degrees upward. This preliminary static aeroelastic analysis shows that divergence is not a matter of concern even in the most strenuous flight maneuver Spyro is capable of.

The calculated overall structural weight for both wings is 810 lb, which is used in mass properties, stability and control, and performance analyses of Spyro.

G. Pressurization Loads

Due to the high service ceiling Spyro is capable of, the cabin must be pressurized to provide a crew environment that is not only survivable, but conducive to crew effectiveness. Simply supplying supplemental oxygen is not enough. A provisional pressurization schedule is as follows [27]:

- Ambient altitude up to 8,000 ft
- Maintain 8,000 ft cabin altitude until 23,000 ft
- Maintain cabin altitude at 5 psi above ambient

X. Mass Properties

A. Weights

Given the dimensions derived from sizing analysis, the weights of the design can be approximated based on a detailed methodology as described in Raymer Chapter 15 [10]. A program is written to take in the dimensions of the aircraft and the mission specifications, then an optimizer is run to obtain the resulting weights and fuel burn of an aircraft of the selected dimensions and missions. While both ferry and design mission are considered, the design mission came out as more demanding and thus is used as the base for final result. According to Raymer Chapter 15, 15% of take off gross weight is used as budget for those components for the weight estimation and balancing practice.

Table 34 Weight Breakdown

Component Group	Total Weight [lb]	CG Location (x,y,z) [ft]	x-Moment [ft-lb]
Wing	810	(17.5,0,0.45)	14,205
Landing Gears	402	(19.42,0,-2.10)	7,807
Nose Gear	80	-	-
Main Gear	322	-	-
Empennage	399	(32.8,0,4.02)	13,071
Horizontal Tail	186	-	-
Vertical Tail	213	-	-
Fuselage Group	2,597	(16.7,0,0.45)	43,237
Fuselage Structure	1270	-	-
Flight Control	193	-	-
Hydraulics & Pneumatic	256	-	-
Electric System	394	-	-
Avionics & Instrument	181	-	-
Air Conditioning, Anti-ice Pressurization System	303	-	-
Power Plant	1,170	(27.4,0,1.91)	31,997
Engine	900	-	-
Fuel System	220	-	-
ECU	50	-	-
Integrated Gun (M61A2)	683	(8.7,0,0.5)	5,907
Gun	202	-	-
Feed System	249	-	-
Full Ammunition (600 rounds)	323	-	-
Inlet Duct	266	(21.2,0,2.52)	5,641
Crew	450	(16.0,0,2.62)	7,207
Operating Empty Weight	6,777	-	-
Payload	3,000	(20.2,0,-1.26)	60,624
Maximum Fuel Capacity	3,585	(20.0,0,0.52)	70,168
Max Take Off Weight	13,362	-	-

B. Center of Gravity and Balance

A trade study is performed on wing placement vs. horizontal stabilizer sizing as shown in the Figures 72-74. The goal is to minimize CG travel during mission and to ensure stability and maneuverability in the extreme CG load out given the tail sizing. The plots present a nose-heavy and tail-heavy wing placement on the left and right side and a neutral design in the middle. While the CG travel remains consistent throughout the displacement, the neutral design represents the smallest possible tail size required to accommodate both the most fore and aft CG positions. In addition, with the constraints stated above, it is ideal to leave a static margin of at least 5% for longitude stability as stated by Raymer [10], which is a standard minimum to this category of aircraft. Spyro achieved a 13.4% static margin for high stability in cruise. Note that the datum plane lies on nose cone of the aircraft with positive direction pointing towards the tail of the aircraft while the reference point for the wing is fixed to the leading edge at the root chord.

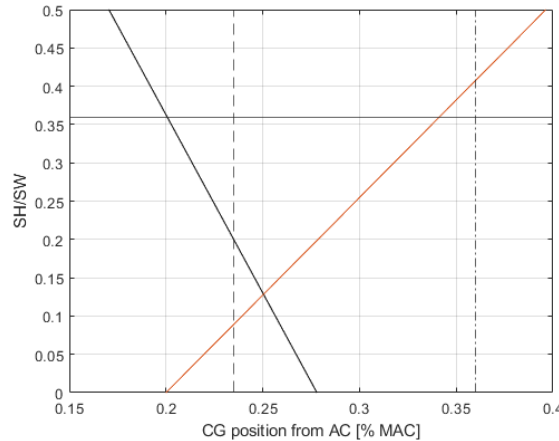


Fig. 72 Wing Placed at 17.35 ft

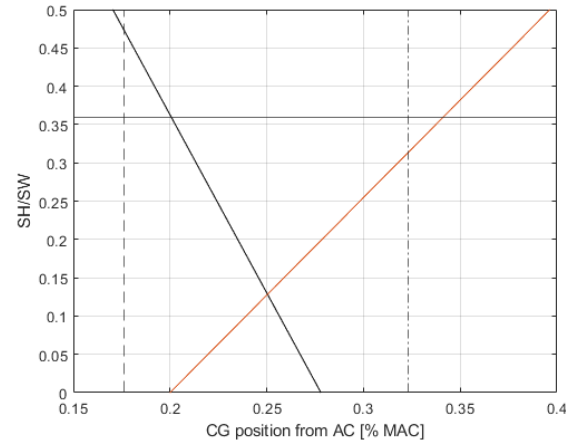


Fig. 73 Wing Placed at 17.75 ft

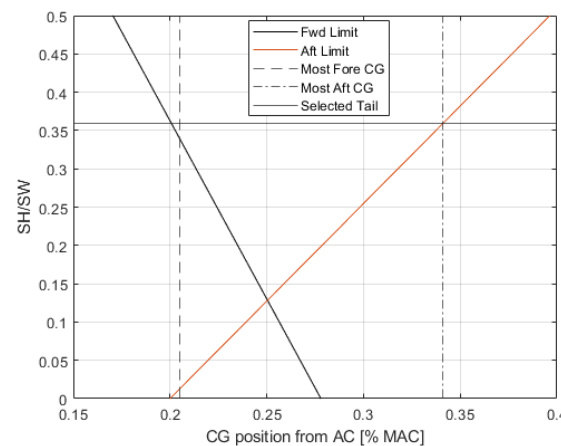


Fig. 74 Wing Placed at 17.55 ft

CG travel is plotted for every possible loading configuration in both longitudinal and lateral direction in Figures 75 and 76. With the optimized wing placement, Spyro achieved 13.6% MAC CG travel across the configurations in longitudinal direction. The lateral CG movement is caused by drop of stores, fuel burn and fuel loss due to potential fuel tank damage during combat.

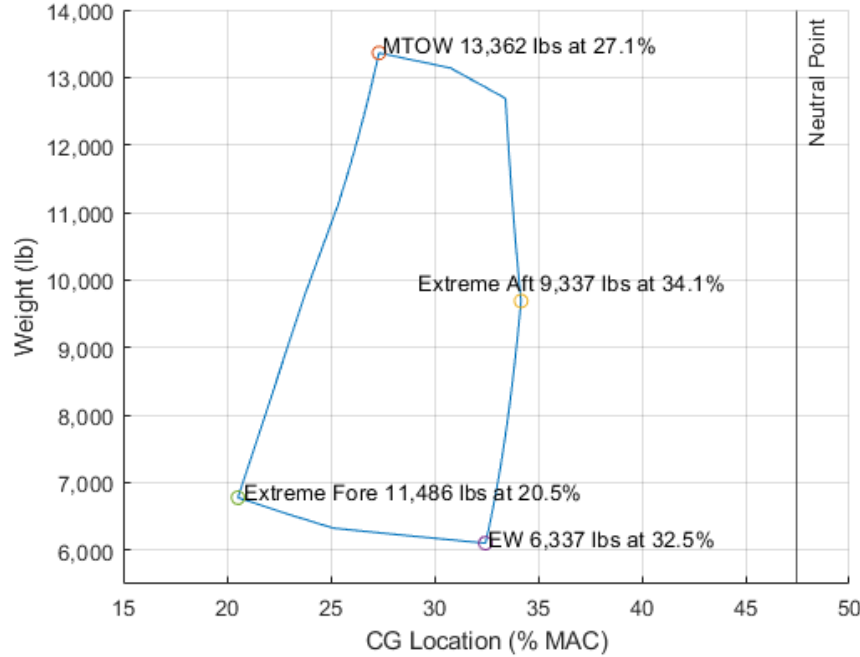


Fig. 75 Longitudinal CG Travel

During the design mission, as specified by RFP, with no store dropped the CG travel of the aircraft was entirely dictated by the fuel burn. Figure 77 illustrates the CG travel of the aircraft in both the design and ferry mission. The CG travel is kept at 0.60% MAC for both design and ferry mission. The numbers that are labeled on the curves represents the fuel weight and CG at the end of segments specified as 2 and 3.

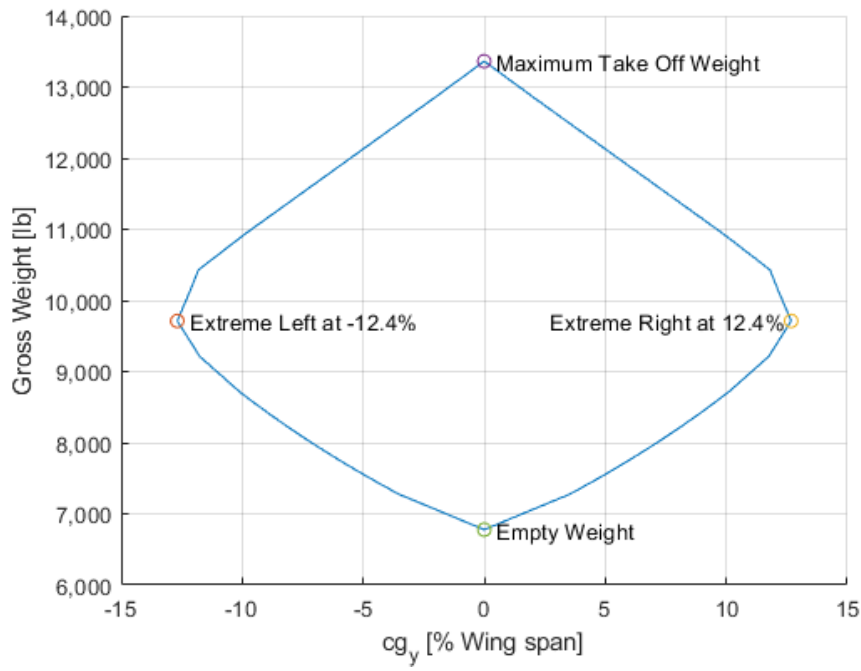


Fig. 76 Lateral CG Travel

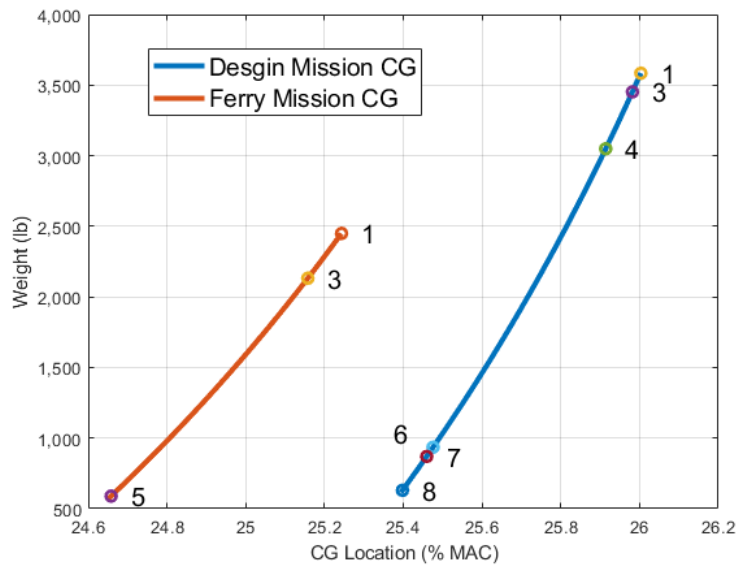


Fig. 77 Fuel Weight and CG Travel During Mission

XI. Auxiliary Systems

A. Flight Controls

Flight controls involve pilot and aircraft control inputs, and the transmission to and execution by the flight control surfaces. For Spyro, a fly-by-wire (FBW) system is implemented. Sutherland [28] explained eleven advantages for FBW systems over conventional mechanical cable systems used in older aircraft. The six primary advantages include: weight savings, design and installation savings, volume savings, increased control reliability, reduction in maintenance hours, and improved handling abilities. Further benefits are also outlined by Fielding [29] such as reduced drag due to the ability to optimize trim settings on the fly. The chief disadvantage however of a fly-by-wire system is the increased initial system costs due to greater electronic complexity. In general, literature concludes that overall costs savings over the service lifetime of the aircraft justify up-front costs for customers [28–31]. This is further augmented by safety benefits that ensure the pilot remains in the flight envelope and can recover the aircraft in emergency situations. FBW architecture is extensively visualized by Collinson [32].

Redundancy ensures operational safety in the event of control system malfunction or failure. This is especially relevant for CAS aircraft that will be taking sustained combat damage. A mechanical cable system was considered, but ultimately not chosen as a fail-safe system. One of the reasons FBW was chosen in the first place was to save much of the weight and volume that is required for all-mechanical systems. If a mechanical system was included as a backup, those benefits would be rendered moot. Similar aircraft that have used a FBW system include the AT-6 Wolverine, which was the finalist for the LAAR program.

Although a backup cable system is not included, redundancy is introduced in the system by way of the data processing computers. Two flight computers will be on board: one for pilot input, and the other for aircraft sensors. Should either of the computers fail, the other computing system is powerful enough to take on the full processing load. Each control surface - flaps, ailerons, rudder, and elevator - is controlled by two actuators. Although instructions for the operation of the control is given by the electronic control system, the hydraulic system is actually used to effect those adjustments. The hydraulic system is detailed later on in this section. The flight controls will also feature a disconnect system, in the event of control surface jamming. For example, if the left aileron were to jam, the disconnect will allow the pilot to separately control the right aileron to maintain partial roll control authority. Pilots are able to select a switch on their control panel that closes all the valves channeling hydraulic fluid to either the port or starboard side of the aircraft.

B. Engine Controls

Engine control systems ensure that the engine selected, the Honeywell TFE731-40, operates at maximum efficiency for any given flight condition. Engine controls on Spyro will be governed by a Full Authority Digital Engine Control (FADEC) system and supplementary Engine Indicating and Crew Alerting system (EICAS). A FADEC is a electronic system that controls all aspects of engine performance. Both of these systems are common on modern aircraft and have

been implemented on the Super Tucano and IA-63 Pampa.

FADEC systems are primarily governed by an on-board electronic engine controller (EEC), sometimes called the engine control unit (ECU). To ensure redundancy, the EEC is separated into two channels, both capable of performing engine control duties independently in case any of the data channels fails or malfunctions. While both channels are operating, cross-talk logic compares data to determine which data stream to use. At any point in flight, if cross-talk logic finds that the secondary channel is controlling engine output better, the computer automatically switches it to be the primary channel. At a higher level, the EICAS will warn pilots of flight critical engine malfunctions that are relayed to the pilots via warning lights or alarms.

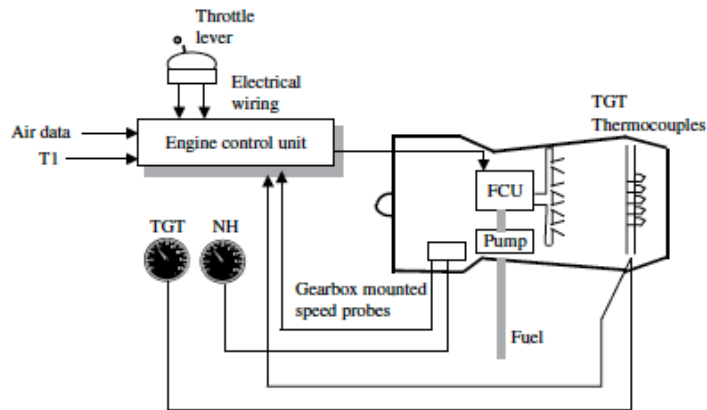


Fig. 78 Engine Control Architecture

Figure 78 shows the engine control architecture as outlined by Moir and Seabridge [33]. The ECU input signals include throttle position, air data, engine temperature data from thermocouples, engine speed, and fuel flow. Fuel flow control and air flow control are the primary output signals. Turbine gas temperature (TGT) and engine shaft rotation speed (NH) are shown as key monitors to ensure that the engine operates safely. Note that T1 is external air temperature data fed to the ECU. The FADEC will be manufactured by Honeywell to guarantee compatibility and seamless integration with the engine.

C. Fuel System (RH)

A block diagram of Spyro's fuel system is presented below in Figure 79. Spyro uses Type-A jet fuel, which is the fuel type most commonly used in the United States. Type-A fuel has a density of 51.17 lb/ft^3 and, with Spyro requiring 3,584 lb of fuel to perform its missions, this amount of fuel takes up 70 cubic feet of space (plus 10% more space in the wings due to the self-sealing bladder tanks [10]).

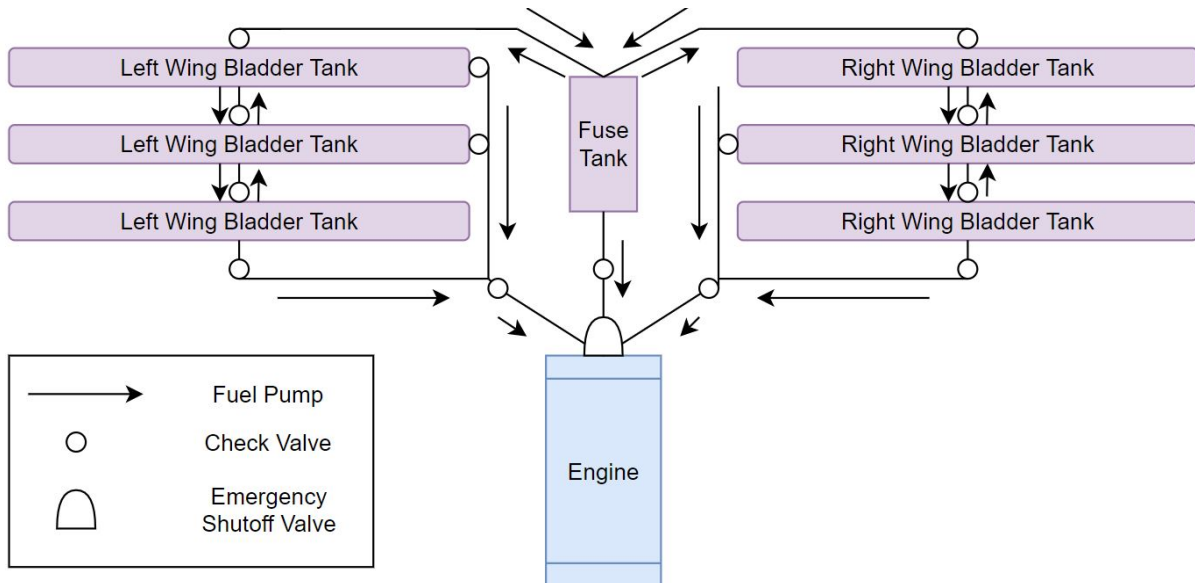


Fig. 79 Fuel System Block Diagram

As can be seen in the diagram, there are three fuel tanks in each wing as well as one tank in the fuselage. The six tanks in the wings are self-sealing bladder tanks which prevent permanent punctures from occurring in them. The seven tanks are able to pump fuel between one another in case of the event that a large enough puncture is inflicted and the self-sealing tanks cannot function properly. With fuel able to be pumped between tanks, this allows for proper fuel dumping should Spyro have to make a premature landing. Having a high number of tanks creates redundancy and minimizes the amount of fuel lost in the case of a large puncture. Each tank also individually feeds into the engine to create even more redundancy. On every fuel line, there is also a check valve which can be immediately shut by the pilot in the event of any fuel leakage. There is also an emergency shut off valve that prevents any fuel from going into the engine in the case of engine or fuel tank ignition. Finally, each tank is lined with anti-explosive foam in case of catastrophic failure.

D. Hydraulic System

As the FBW system has been outlined previously, hydraulic systems are responsible for control surface actuation, landing gear brakes, and steering. There will be two hydraulic reservoirs accompanied by individual pumps located in separate parts of the fuselage. Two separate reservoirs are used for redundancy in case one is damaged in combat. The forward reservoir will control relevant vehicle components on the port side of the vehicle while the aft reservoir is responsible for the components on the starboard side. Hydraulic pumps are 3,000 psi piston pumps. Although higher pressure pumps have been developed, 3,000 psi pumps are currently standard and satisfy MILSPEC, which reduces manufacturing and maintenance cost. Further, higher pressure pumps have not yet been fully optimized. The hydraulic

lines themselves are on separate areas of the aircraft to reduce probability of total system failure or damage from combat.

Note that either reservoir is not solely responsible for control surfaces on its associated side. During operation, both systems will be used in tandem. Hydraulic connections are designed such that, in the event that a reservoir or pump malfunctions, the other is still able to power necessary control components. Note that in the event of single pump failure, because there is now only one pump driving the hydraulic fluid, actuators on the control surfaces will act in a limited manner, but pilots will still have control over the vehicle. In the event of dual pump failure, an electro-hydraulic pump powered by the onboard batteries described in the next section provides hydraulic power for a limited duration after which the main pumps are restarted. Full hydraulic system architecture is given by Figure 80.

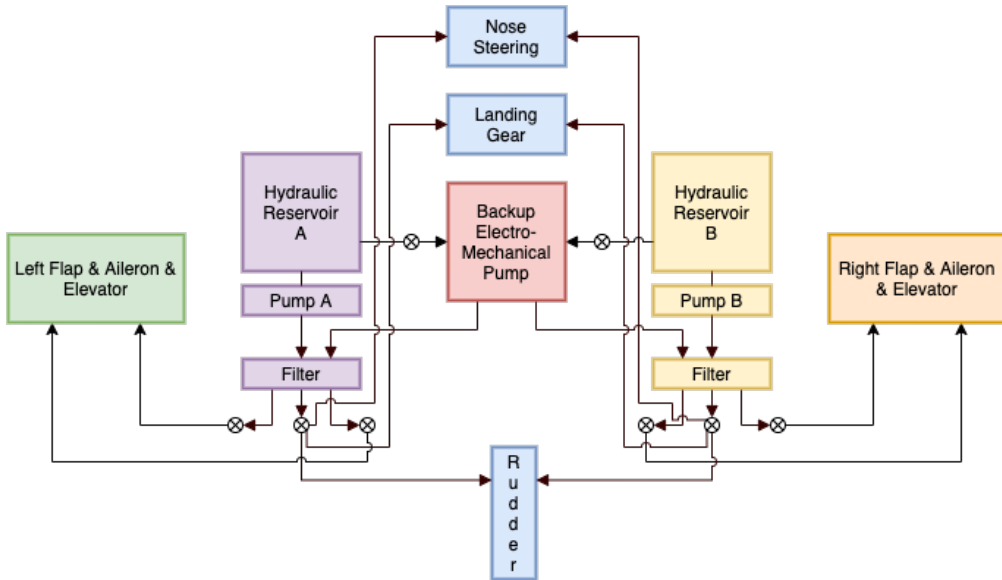


Fig. 80 Hydraulic System Architecture

E. Electric System

Spyro's electrical system provides 28 V DC power and 115 V three phase, 400 Hz power per MIL-STD-516C [6]. DC power comes from a engine-driven starter-generator and one 24V 23Ah Lithium ion battery. The vehicle is also capable of receiving DC power from a ground power unit (GPU) when the engine is not in operation but electric systems are required on the ground. DC power is responsible for avionics, de-icing, and cockpit climate control for pilot comfort.

The DC power has three buses: one primary, one secondary, and one essential. The batteries are connected to the primary bus while the generator is connected to the secondary bus so that DC power is appropriately distributed throughout Spyro. The essential bus is connected both the primary and secondary busses and can also be energized by them. By default, it is attached to the primary bus. The essential bus is to be utilized in emergencies in case of battery or generator failure. Having both a battery and a generator also ensures that in the event that either malfunctions, the

other source is still providing DC power. Note that 270 V DC batteries were considered. However, optimized systems would not be developed in time for 2025 service entry.

115 V AC power is sourced from two static inverters. There is a primary inverter, connected to the primary DC bus. The second inverter is for backup in case of failure and is connected to the secondary and essential DC bus. The primary inverter is used to provide continuous normal AC power but is automatically disconnected and the standby inverter is connected in case of malfunction. Pilots have battery warning lights and DC voltmeters on the flight deck for monitoring.

In the case that the DC starter-generator fails, the batteries will be able to provide essential power to the aircraft instruments and hydraulic pumps while the restart procedure is enacted by the crew. Lithium ion batteries were chosen as they are lightweight compared to Ni-Cd batteries and are more efficient. An Electro-Mechanical Expulsion Deicing (EMEDS) system detects ice via a sensor and when ice starts to accumulate, coils behind the leading edge vibrate causing the ice to break off. EMEDS was chosen because it has low power requirements and does not modify the airfoil surface. A diagram of the EMEDS system can be found in Goraj [34] and is reproduced below.

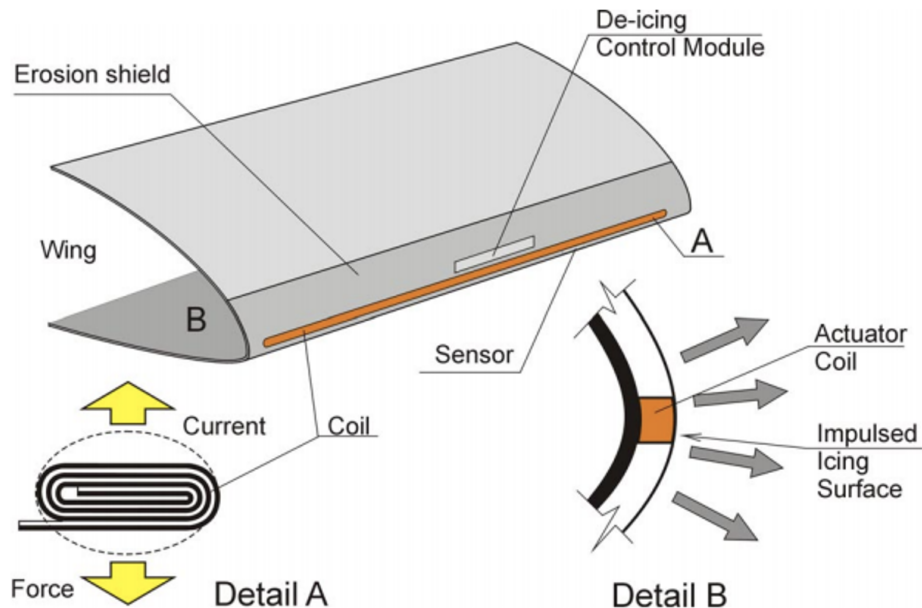


Fig. 81 EMEDS system

F. Pneumatic and Environmental Control System

The pneumatic system takes bleed air from the engine compressor and distributes it to various parts of the aircraft. The bleed air is used for flight deck pressurization, air conditioning, hydraulic system reservoir pressurization, equipment cooling, anti-icing, and canopy demist. A simplified diagram of the pneumatic and environment control system (ECS) is in Figure 82.

To protect against chemical and biological threats, emergency air/oxygen is provided by way of respirators. An on-board oxygen generation system (OBOGS) takes pre-conditioned air which is reduced to a pressure of approximately 35 psig through a pressure reducing valve. The oxygen concentrator uses zeolite beds to produce oxygen-rich gas. There is a controller that electronically monitors the oxygen concentration of the flight deck and adjusts based on flight altitude [35]. Using an OBOGS as the primary oxygen source is more advantageous than traditional cylinder or liquid oxygen bottles that limit sortie duration, are heavier, and need bottle replacement frequently or significant ground infrastructure [33]. Because the OBOGS is reliant on the ECS, should the ECS fail, the OBOGS would also be rendered useless. As such, a liquid oxygen bottle will also be on board as a standby means for emergency oxygen while the crew can descend to a lower altitude and return to base.

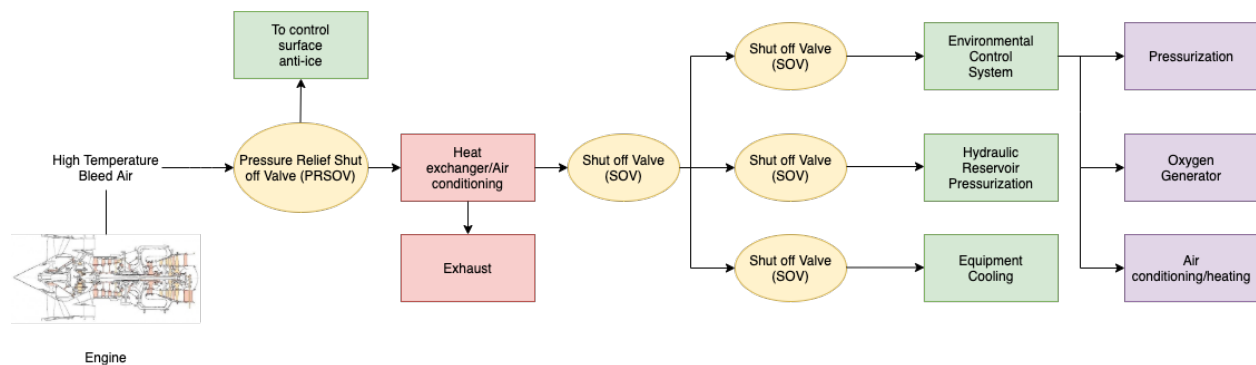


Fig. 82 Pneumatic and ECS architecture

G. Emergency Systems

Emergency systems are the last line of defense in the event of vehicle malfunction or failure. At the most basic level, pilots must be aware of system failures in order to take corrective action. Spyro will feature a central warning panel that will then alert the pilot audibly in their headset, and through a flashing light or alarm which the pilot will have to silence and then rectify the situation. For example, in the unlikely event that there is a fire on board, the crew will be first notified of the increased temperature. This is most likely to occur at or near the engine. From the cockpit, they can then depress a button or flip a switch that releases Halon 1211 or another similar halocarbon fluid to extinguish the fire.

The RFP [1] specifically outlines the need for zero-zero ejection seats which will allow the crew to abandon the aircraft at any flight condition due to catastrophic failure. A Martin Baker Mk16 ejection seat will be fitted for both pilots and there will be an entirely automatic system for ejection system timing. The ejection seat is provided with a full harness, restraints to avoid limb flailing, parachute, dinghy, oxygen supply, and location beacon. The Mk16 satisfies RFP requirements and has been used to aircraft such as the T-6 Texan II. The canopy will be shattered just prior to seat ejection by a pattern of miniature cords embedded in the canopy.

Two key elements of the emergency systems are relevant in the case of a crash. Particularly for the CAS mission

profiles of Spyro, the aircraft may have to be landed in dangerous conditions with wheels up or wheels down. The crew will then have to quickly yet safely exit the aircraft. As such, a crash switch is on the flight deck which shuts down the engine, closes fuel valves, disconnects the aircraft battery, and discharges the fire extinguishing bottle into the engine bay. Per MIL-STD-516C, Spyro also carries a cockpit voice recorder and flight data recorder as it may have to fly in civilian airspace [6].

Spyro has an arrestor hook for engaging rotary hydraulic arresting gear (RHAG) that is common in military airfields. Compatibility with arrestor systems is important in the event of system failures leading to an aborted takeoff or an emergency landing. Backup and redundant systems for the previously discussed auxiliary systems are within their respective sections. All wiring throughout the plane is jacketed to mitigate the effects of electrical wiring interconnect system (EWIS) interference.

H. Systems Integration and Inboard Profile

Placement of auxiliary systems within the aircraft are key in increasing the survivability of Spyro. Full internal configuration of the described systems is given by Figure 83.

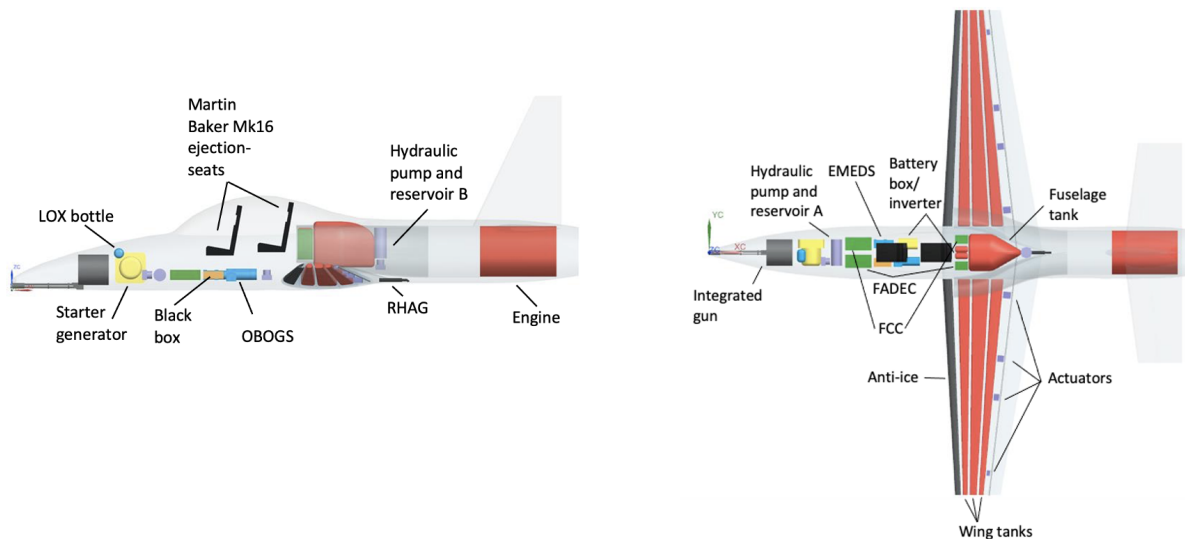


Fig. 83 Inboard profile

Figure 83 shows that all of the required systems can be fit within the structure of the vehicle. To increase survivability and ensure that systems are truly redundant, individual components within a system classification are split between the forward and rear systems compartments. The forward compartment is underneath and in front of the flight deck, while the rear compartment is behind the flight deck. For example, hydraulic reservoir A and B are separated between the forward and rear. This is also done for electrical systems, and flight and engine computer systems. Should the aircraft sustain damage behind the engine, systems located in the forward systems bay are capable of supporting the aircraft.

The benefits of splitting the system bays in regards to maintenance have also been outlined in Section IX.B.

I. Avionics

The avionics will mainly be selected from the Cockpit 4000 bundle. This gives all of the proper equipment for the system. One benefit of this system is that it is modular for many different classes of aircraft and allows a multitude of sensors to be equipped. There will be communications links such as Datalink 11 and 22 along with UHF and VHF communications. There will also be a Data Transfer System (DTS) to upload mission and map data along with maintaining an aircraft data log. The sensors included will be a laser target designator (LTG) and a forward looking infrared sensor (FLIR) which should help ordnance performance.

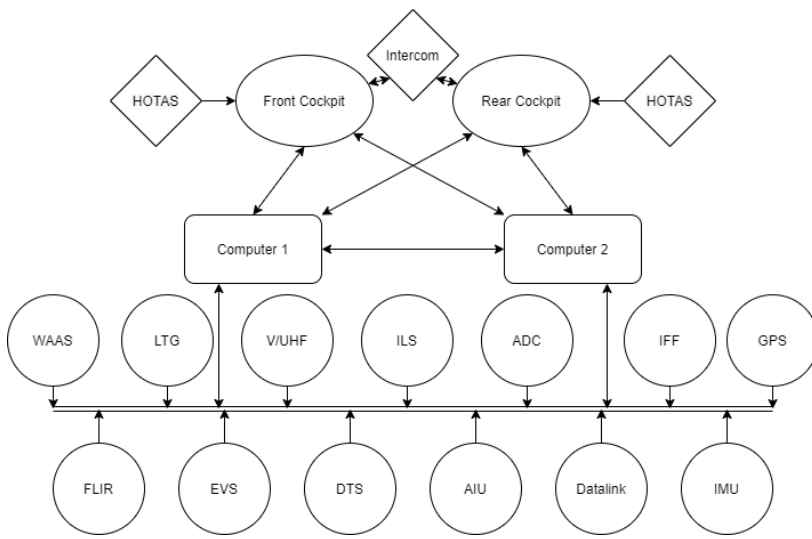


Fig. 84 Avionics Layout

The guidance system will be a Global Positioning System (GPS) and will further include a Wide Area Augmentation System (WAAS) which improves the accuracy of the GPS system. There will be redundant wiring between these sensors and the main data bus in the case of fire or battle damage. These computers have the ability to show various layouts depending on the current state of the aircraft which can be advantageous as the data layout to the pilot can be customized depending on the specific mission requirements and armament configuration.

An Armament Interface Unit (AIU) will be used to control the release payloads and ordnance. The aircraft will also need a Identification Friend or Foe (IFF) system because of the general mission profile will most likely involve cooperation between several aircraft. Some sensors used to ease flight are the Enhanced Flight Vision System (EVS) which could help increase pilot visibility under the aircraft, and an Instrument Landing System (ILS) to allow for take-off and landing in non-optimal weather conditions. Finally an Air Data Computer (ADC) will calculate the airspeed of the aircraft via a pitot static system. One benefit of the fly-by-wire system is the ability to easily implement a side stick with Hands on Throttle-and-Stick (HOTAS) allowing the pilot to adjust settings of the aircraft without needing to remove their

hands from the controls. A system that was not chosen but was considered is a Directional Infrared Counter Measure (DIRCM) system because of the fact that currently it is not known if this newer technology will become affordable enough to justify the acquirement and maintenance costs of the system. However, the Cockpit 4000 system selected runs various communication methods that and will most likely be compatible with a DIRCM system developed in the future.

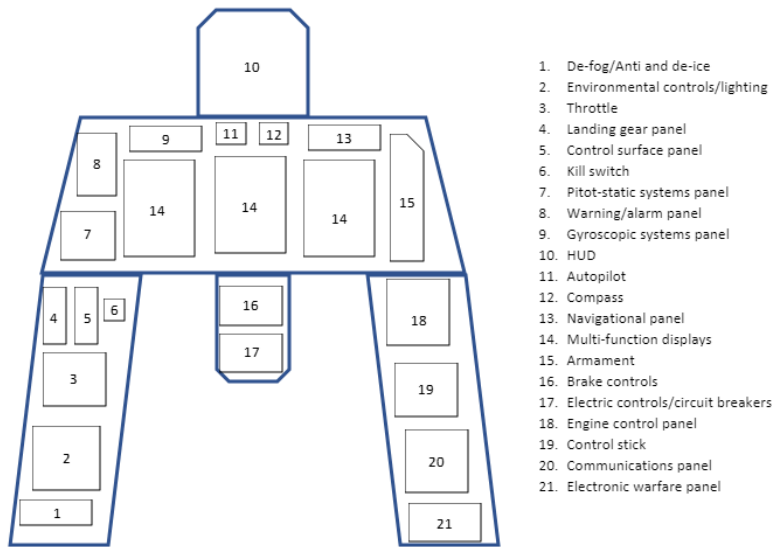


Fig. 85 Cockpit Layout

The cockpit layout is shown in Figure 85 and will take advantage of the multi-function displays in order to allow the pilots to properly select whichever display setup is most advantageous at that time. This system, along with a HOTAS configuration, will allow both front and rear pilots to easily control all of the aircraft quickly and easily. The cockpit layout is identical for the front and rear pilots in case one pilot is incapacitated and the other must take full control of Sypro.

XII. Ordnance

A. Desired Characteristics

As mentioned in the RFP the main requirement is 3,000 lbs of armament which gives a rough size of the ordnance capabilities in order for the aircraft to achieve this requirement. The next requirement for ordnance selection comes from the class of aircraft. A light attack aircraft will have to be equipped with mainly air to ground ordnance that can also be equipped on similar missions for attack helicopters. It is important to note the provisions for carrying a variety of weapons including rail-launched missiles, rockets, and bombs up to a maximum 500 lbs. A general list can be configured of common ordnance falling under these constraints which can be further refined later. It is desired to design the aircraft with the capability of ordnance flexibility so that the customer may utilize the ordnance of their choice.

Therefore, the discussion of commonly used general purpose bombs and missiles will be done to ensure this ability.

B. Ordnance Selection

Considering the large amount of options to place in the armament payload, a trade study of generally used bombs and missiles was done as followed [36–44]. Studying a large range of ordnances and their dimensions and launching mechanisms will provide insight in layout suggestions. Further satisfaction of the RFP requirements will allow the load out of different arrangements of the studied ordnances to provide air to air and air to ground mission capabilities.

Table 35 Ordnance Trade Study

Name	Weight [lb]	Length [in]	Launcher	Notes
Unguided Missiles/Rockets				
Hydra 70	13.6	41	MK260/MK261	7- Tube/19-Tube
CRV7	14.5	41	SUU-5003/LAU 5002	4-Tube and Bomb Capability
SNEB	11	48	Matra 155 Launching Pod	Custom 36-Tube Pod
Air to Ground Missiles- Guided				
AGM65-D Maverick	485	98	LAU-117	Electro-optical/Laser/IR guided
AGM 114 Hellfire	100	72	M272/M299	Laser Guided
AGM-179 JAGM	108	72	M272/M299	Radar Guided, Developing
Air to Air Rail Launched Missiles- Guided				
AIM-9 Sidewinder	190	114	LAU-7	Wingtip, IR Homing
AIM-120 AMRAAM	335	144	LAU127/128/129	Medium Range, Radar Guided
ASRAAM AIM-132	194	114	LAU127/128/129	Close Combat, IR Homing
General Purpose Bombs				
Mk82	500	87.4	BRU32/33	Unguided, Many Variations
GBU-39 (SDB I)	285	70.8	BRU32/33	GPS/Internal Navigation System
GBU-53 (SDB II)	204	69	BRU32/33	Radar/Laser/IR Homing/GPS

After the collection of the shown data, the ordnance selection can follow by first selecting reliable weaponry for short range and close air support missions. Ordnance such as the AIM-120 AMRAAM will be unnecessary first due to the medium range usage, and also the radar guided navigation system implementation. Although radar offers more

advanced precision guided missiles, radar is unnecessary on this aircraft as the desired weaponry systems will contain their own implemented navigation system and will generally not need radar guidance for short range combat. Therefore, ordnance that offers wide-use among popular aircraft and launching mechanisms as well as satisfy the short range air to ground combat requirements were selected for sample layouts.

C. Gun Selection

In a similar fashion, the required integrated gun will be implemented by first conducting a trade study of possible cannons, Gatling guns, and mini guns that are traditionally operated on light attack aircraft and attack helicopters. The ultimate gun selection is driven by weight distribution and stability, affordability, similarity analysis, and combat performance of the integrated gun [44–48].

Table 36 Gun Selection

Name	Platform	Weight [lb]	Length [in]	Caliber [mm]
DEFA Cannon 554	IA63/ C101	187	65	30
GIAT 30	Dassault Rafale	260	94	30
M230 Chain Gun	Apache	130	85.9	30
Mauser BK-27	Alpha Jet/ Typhoon	220	91	27
GAU-12	AV-8 Harrier	270	83.2	25
GAU-22	F-35	230	83.2	25
M-61A1 Vulcan	F105/ F-4/ USAF	202	72	20
M-197	AH-1/ OV-10 Bronco	132	-	20

It was determined by the team to ultimately implement the M-61A1 integrated gun in the nose of the aircraft with 600 rounds of ammunition. This selection was determined due to the reliability and large use of the M61 Vulcan in US Air Force vehicles in modern aircraft. The M-61 Vulcan also provides a fire rate of 6,000 shots per minute while limiting recoil and weight distribution due to its light weight configuration [46]. The Vulcan provides strong maintainability over a 25 year service life and is manufactured for air to ground purposes thus satisfying the requirements of the RFP [1]. It ultimately offers the greatest flexibility in terms of driving systems, overall size, and combat performance out of the studied options. The ammunition selection is done in cooperation with mass properties when selecting an ammunition amount that balances the travel of the center of gravity with the needed survivability of the integrated gun. A further investigation into the center of gravity is described in Section X.B. The draw backs of this selection will be first the strength, as a 20 mm caliber gun may prove inferior to a larger and more forceful cannon. Although this is true,

computations done by mass properties and structures prove the need for weight conservation towards the front of the aircraft as a larger system may shift the weight distribution and exceed the available weight capacity for stability. The ultimate reliability of the M61 Vulcan along with the flexibility of load outs on the wing hard points will suggest the direction in gun selection.

D. Ordnance Load Out

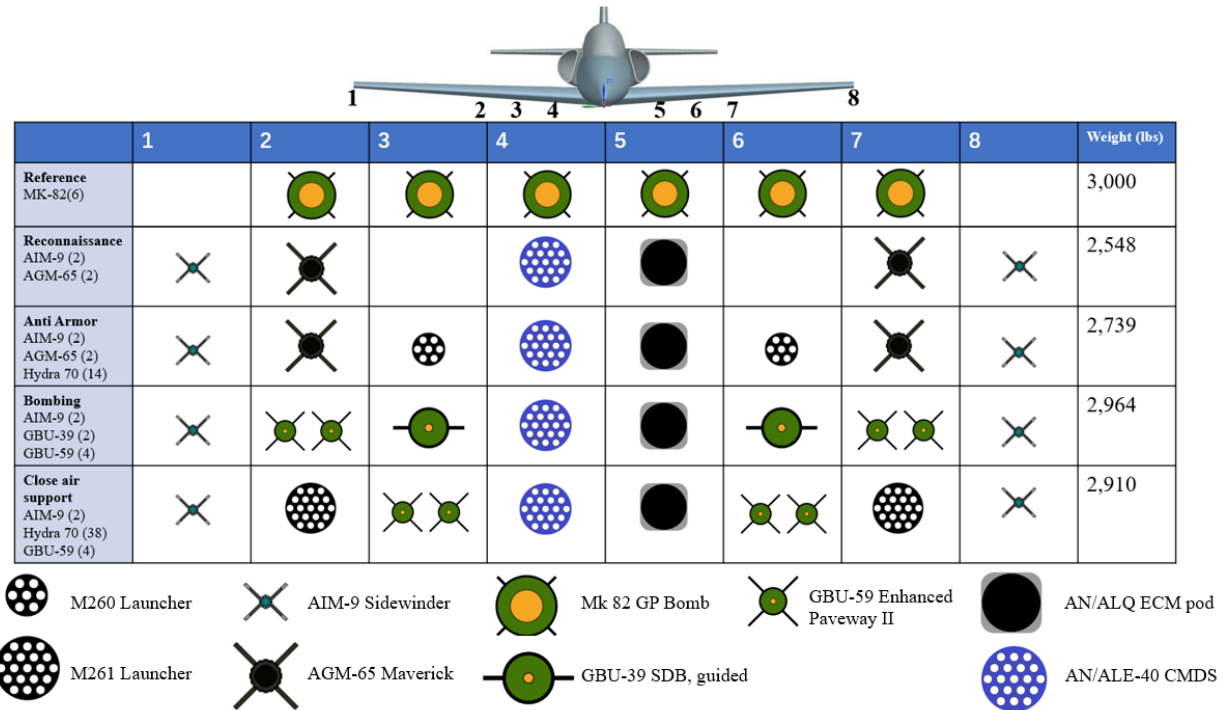


Fig. 86 Ordnance Load Out Chart

The shown chart in Figure 86 provides a variety of different loadout capabilities for Spyro. It should be noted that the reference load out consisting of 6 MK-82 unguided general purpose bombs will be utilized for the aerodynamic simulations and design mission simulation as this will provide a simple example that will also serve as the maximum drag configuration for the aircraft. These missions will satisfy the capability to hold 3,000 lb of ordnance and a capability for various air to ground, air to air, and bombing combat. Each ordnance selection will be externally stored as shown on their respective hard point. Standard SUU-63A pylons, similar to their use on the F-18, will be used for simplicity to connect each weapon to their respective launching mechanism except for the wingtip installations [49]. The mentioned pylons will attach on designated mounting points on the aircraft and will allow the mounting of various stores as well as dismounting of the pylon for a clean ordnance layout. Wingtip ordnance implementation will be possible using a LAU-7 pylon capable of rail launching a single AIM-9 Sidewinder missile as shown [44]. Each bomb selection's hard point will be limited by the capacity of its BRU-32 bomb rack that can hold up to 2,000 lb of ordnance. Additionally, the used

MK261 launcher for Hydra rockets is capable of carrying 300 lbs and the LAU-117, used for carrying a single Maverick missile, is a rail-guided launcher capable of carrying 500 lb of weaponry [44].

Guided weapons that are required by the provided load out chart are selected due to their internal navigation system and their infrared capabilities. Therefore, as discussed in avionics, there is no need for radar implementation for ordnance purposes although a MX-15Di sensor can be installed on the belly of Spyro's fuselage for high-definition target tracking, GPS, laser tracking, and infrared support [50]. This sensor along with the internal navigation stated in Table 33 for each weapon, will provide the needed homing devices for close air support combat in short range battle. Further survivability can be supported by the shown AN/ALQ ECM pod in regard to radar jamming opposing threats as needed. Additionally, the implemented AN/ALE-40 countermeasure pod will supply chaff and flares to distract opposing infrared tracking systems for improved survivability [44].

E. Safety Considerations

It is key to assess the safety considerations when implementing the various ordnance systems as described. The first consideration is due to the launching mechanism for the weaponry. AIM-9 Sidewinders will be rail-launched from the wingtips after its internal explosive motor slides the missile free from the LAU-7 system. To provide safety for this systems and included fragmented warheads, its internal arming system requires a minimum 20 g acceleration for 5 seconds before arming [40]. Similar safety features are implemented into systems such as the used BRU-32 bomb racks which consist of sway resisting bracers and interlock systems to prevent from ejection when under infeasible conditions such as unstable swaying of the bombs and unreasonably high speeds. This feature will prevent from Spyro damaging itself with self-dropped stores [44]. It should be noted that all implemented guided weaponry in the ordnance load out internally implement nitrogen cooling systems for tracking devices. Further, the dropping of stores and individual ejection of weaponry will be controlled by the pilot flight computer, with a probability of manual over ride, as described in Section XI.

XIII. Acoustics, Observability, Emissions

A. Survivability Aspects

Survivability have been discussed throughout the previous sections to address the CAS nature of Spyro. One specific consideration is covered in Section XI.C, which mentions redundancies in the number of fuel tanks as well as the implementation of self-sealing fuel tanks to prevent puncture.

Another major consideration is infrared signature reduction, especially around the engine exhaust. Infrared suppression systems (IRSS) come in many forms on several military aircraft. This is an important addition because infrared targeting systems are commonplace on the battlefield in the form of SAM turrets or other infrared-guided missiles. An infrared suppression design that minimizes increased drag and thrust loss in chevrons within the exhaust

duct. These chevrons absorb heat and reduce thermal signatures significantly. A notable aircraft that implements this design is the F/A-18 Hornet. Spyro also features an AN/ALQ ECM pod as well as an AN/ALE-40 CMDS pod. The AN/ALQ ECM pod is able to jam radars to prevent detection and the AN/ALE-40 CMDS pod fires chafes and flares to further prevent missile lock-on.

To further reduced infrared detection, a study was performed to determine a paint to use which minimizes infrared emissivity [51]. Figure 87a [51] compares the emissivity of different paints, The AMSS 36375 paint is a conventional topcoat for military aircraft and, as shown, it was very high emissivity. On the other hand, LE AMSS 36375 paint has very low emissivity in comparison. Therefore, LE AMSS 36375 paint was chosen for Spyro to decrease infrared signature detection.

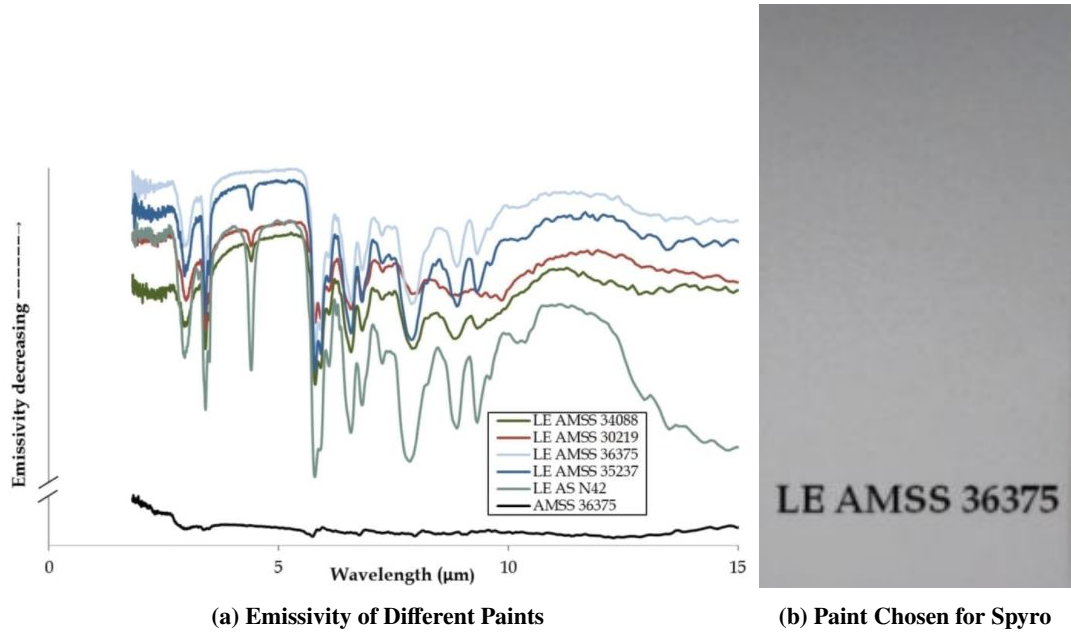


Fig. 87 Figures for Choosing a Paint for Spyro

Finally, Spyro could be optioned with titanium armor plates as presented visually in Figures 88a and 88b. With the option, pilots are protected by a 0.5 inch thick Ti-6-4 titanium armor tub around side and bottom. Compared to the armor plates that are fixed to the outside of the aircraft such as A-29 Super Tucano, this design benefits from a more comprehensive protection with less material involved. In addition, since the armor is placed inside, the aircraft benefits from better aerodynamics and uncompromising invisibility. While the whole package weights 460 lb, pilots and engine are given higher chance of survival against incoming projectiles. The similar design could be realized with fabric or composite material to further enhance survivability against armour piercing projectiles.

Table 37 Material Properties of Armor

Material	Density [g/cm ³]	Tensile Strength	Hardness	Elongation
TI-6AL-4V	4.45	>896 Mpa	302-364HB	>10%

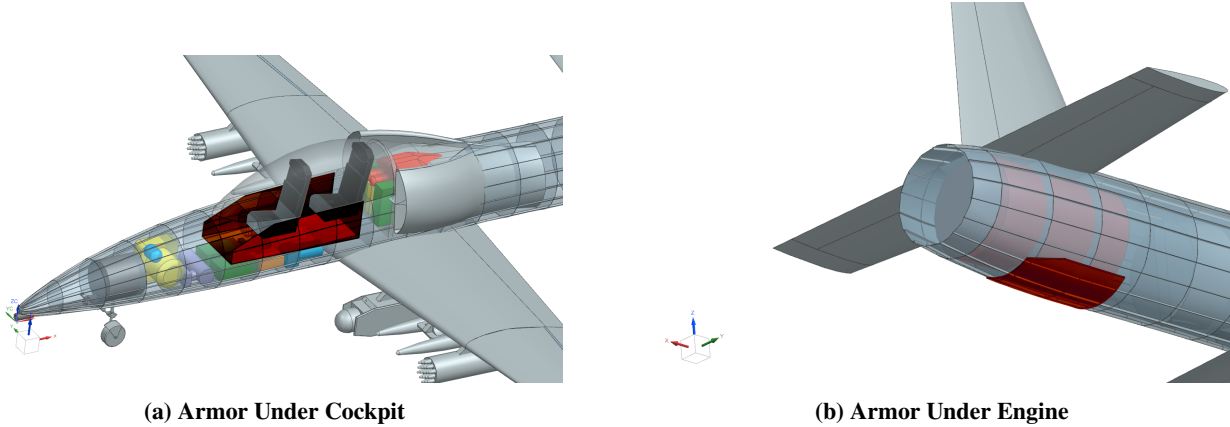


Fig. 88 Armor Plate Locations

B. Acoustics & Emissions

While there is no acoustic requirement listed in the RFP [1], it can still be useful to look at acoustic properties for survivability considerations. The acoustic properties of the TFE-731-40 engine, specifically, are not readily available. Instead, a generalization based on acoustic studies of turbofan engines equipped with chevrons was made. A typical turbofan engine equipped with chevrons emits 97.71 decibels during idle thrust [52]. This is on par with other military aircraft.

Currently, the aircraft industry is actively looking towards leaving less of a carbon footprint. Therefore, it is important to take note of the emissions data for this aircraft. Spyro uses Type-A jet fuel, the fuel type most commonly used by American aircraft, which emits 3,000-3,125 grams of CO₂ per kilogram of fuel burned [53].

XIV. Cost Analysis

A. Life Cycle Cost Estimation

The Life Cycle Cost (LCC) is defined as the comprehensive cost of developing, producing, deploying, maintaining, operating and disposing of a system over its entire lifespan. The LCC estimation of Spyro consists of four major categories: Research Development Test and Engineering cost (RDTE) cost, Operating cost, Acquisition cost and Disposal cost. The LCC model is analyzed under the guidance of Roskam [11] cost estimation. To adjust for inflation, Bureau of Labor Statistics inflation calculator is used for manufacturing raw materials and labor involved. Therefore, all

monetary value in presented as of year 2021.

During the RDTE phase of the life cycle, 4 areas contribute to the spending: Air frame Engineering and Design, Development Support and Test, Flight Test Airplanes, and Test and Simulation Facilities. To test and verify our design, 5 fully equipped prototypes will be produced with 2 static test aircraft. Development, tooling, manufacturing, and test flight operation contribute to the laboring hours which adds up to a total of 26,036,000 hours and the labor rate for engineering, tooling, and manufacturing are \$120, \$120, \$70, based on [11]. This rate will be assumed consistent through out the acquisition phase of the program life cycle. Note that due to the aid of program assisted design that accelerates the design iteration, a factor of 0.8 is applied to the engineering and design cost.

Table 38 Research Test Development Engineering Cost

Category	Cost [USD]
Air frame Engineering and Design	\$101,610,000
Development Support and Test	\$37,667,000
Flight Test Airplanes	\$242,250,000
Flight Test Operation	\$9,978,600
Test and Simulation Facilities	\$130,500,000
Profit over Flight Test Airplanes	\$65,251,000
Finance of Flight Test Airplanes	\$65,251,000
RDTE Cost	\$652,510,000

The acquisition phase refers to the production and delivery stage of the program. As required by the RFP [1], a fleet of 50 Spyro will be produced. Airframe Engineering and Design, Engine & Avionics, Manufacturing, Material, Tooling, Quality Control, Flight Test, Financing are the main spending in this phase. A total of 6,357,200 hours of labor is involved with labor hours stated above. Please note that the model is prevalent to a few decades ago whereas production nowadays is more automated therefore the final cost presented is considered as a conservative estimation. With RDTE and Acquisition Cost calculated, the unit cost of Spyro arrives at **\$25,275,000**. Spyro offers a significant lower price tag compared to currently in-service fighter jets while providing equal capability in completing mission as specified as RFP. With higher numbers of production the aircraft is competitive to propeller powered light attack aircraft such as A-29 Super Tucano.

Category	Cost [USD]
Airframe Engineering and Design Cost	\$53,249,000
Engine & Avionics Cost	\$144,930,000
Manufacturing Cost	\$129,140,000
Material Cost	\$80,512,000
Tooling Cost	\$56,231,000
Quality Control Cost	\$16,788,000
Subtotal: Airplane Production Cost	\$480,850,000
Cost of Flight Test & Operation	\$19,259,000
Manufacturing Financing Cost	\$55,568,000
Subtotal: Program Manufacturing Cost	\$555,570,000
Profit over Manufacturing Phase	\$55,680,000
Acquisition Cost	\$611,250,000

The operating phase is the highest of all the spending in the life cycle of the Spyro program. Fuel & Oil & Lubricant, Direct Personnel, Indirect Personnel, Consumable Material (such as tires), Spares and Miscellaneous contribute to the spending at this phase. A 1,200 flight hours per year is requested for Spyro that are in service. An fuel burn of 600 lb / hr is estimated with an fuel price of \$2.58 suggested by Secretary of Defense for JA1. Note that the crew is paid at \$46,068 per year based on CPI adjusted value from [11].

Due to low take off gross weight compared to other turbofan powered jet trainer and attack aircraft, the development and manufacturing cost is reduced. Another benefit that comes with low weight is a better fuel economy overall. When paired with the TFE731 engine introduced in Section V, the aircraft achieved a competitive hourly operating cost. The other aspect of the benefit of using this engine is discussed in next subsection. In the chart below, Spyro's operating cost per flight hour is found to be comparable to T-45C, a jet trainer with almost identical dimensions and a similar take off weight of 13,500 lbs, whose direct operating cost (DOC) is \$5,508.

Category	Cost [USD]
Fuel & Oil & Lubricant	113,350,000
Direct Personnel	8,848,600,000
Indirect Personnel	1,219,700,000
Consumable Material	1,202,300,000
Spares	609,840,000
Depot	731,820,000
Miscellaneous	487,880,000
Operating Cost	6,098,500,000

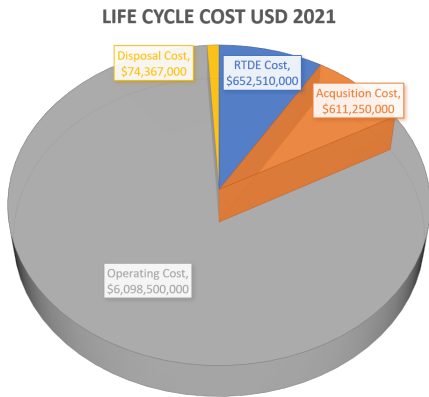


Fig. 89 LCC Break Down

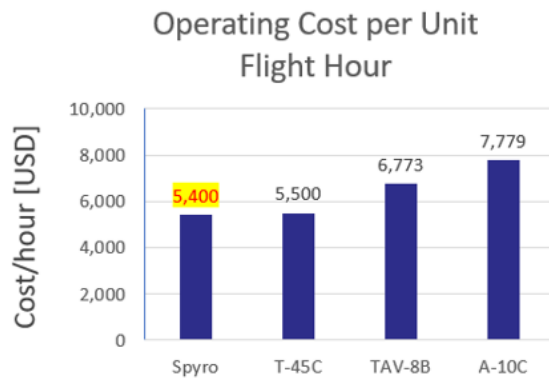


Fig. 90 Cost per Unit Flight Hour [USD]

B. Cost Savings

Cost saving is the one primary driving force for the design of Spyro. The aircraft's performance is optimized for a conventional structure made of Aluminum as described in Section IX which is widely applied in all variation of aviation. The conventional choice allows manufacturing with ease, effectively reducing manufacturing complexity and human labor involved in the development and production of the aircraft. The engine of Spyro is selected to be the TFE731-40. Other engines are available that could potentially offer higher thrust for similar weight and size. However, the TFE731 family is widely used in both military and commercial market, minimizing the operating and maintenance cost of the engine by reducing the personnel training cost. Further, spare parts are easier to source and access.

XV. Conclusion

The requirements outlined by the RFP have been met by the current design iteration at the current level of fidelity. RFP requirements along with the capabilities of Spyro are listed below:

Table 39 RFP Requirement Summary

Criteria	Requirement	Spyro	Section
Payload (aramament)	3,000 lb	3,000 lb ✓	XII
Integrated gun	Any	M-61A Vulcan ✓	XII
Service ceiling	30,000 ft	30,646 ft ✓	VII
Zero-zero ejection seats	Any	Martin Baker Mk16 ✓	XI.G
Takeoff field length	$\leq 4,000 \text{ ft over } 50 \text{ ft obstacle}$ at density altitude $\leq 6,000 \text{ ft}$ with CBR = 5	3,836 ft with $\mu_g = 0.1$ ✓	VII
Landing field length	$\leq 4,000 \text{ ft over } 50 \text{ ft obstacle}$ at density altitude $\leq 6,000 \text{ ft}$ with CBR = 5	3,939 ft with $\mu_g = 0.1$ ✓	VII
Certification	MIL-STD-516C	MIL-STD-516C ✓	Throughout
Crew	2	2 ✓	IV
Ferry range	900 nmi	1,033 nmi ✓	VII

Other key aspects of Spyro that are less easily quantified include a focus on survivability and serviceability in the field, due to an all metal internal structure, simplifying both component repair and replacement part sourcing. Infrared signature suppression is employed to reduce exhaust heat signature, taking the form of an environmentally cooled exhaust duct. Leading edge high lift devices are not present, as our analysis has not demonstrated a need for them. This simplifies the wing structural design, removes points of failure, and reduces the maintenance requirements of Spyro. Dual redundant hydraulic systems along with a tertiary battery-driven electric pump are employed to improve survivability and airframe recovery in the event that battle damage compromises the main hydraulic pumps. Self sealing fuel tanks additionally improve battle-worthiness. Spyro is a cost-competitive solution to the given RFP and satisfies the initial goals for the design process.

References

- [1] AIAA, “Request for Proposal: Austere Field Light Attack Aircraft,” 2020.
- [2] Hawkins, J., “Joint Tactics, Techniques, and Procedures for Close Air Support (CAS),” 2003.
- [3] Tittel, S., “Cost, Capability, and the Hunt for a Lightweight Ground Attack Aircraft,” Ph.D. thesis, Jun 2009.
- [4] Trimble, S., “Irregular warfare offers new role for propeller driven aircraft,” , Oct 2010. URL <https://www.flightglobal.com/irregular-warfare-offers-new-role-for-propeller-driven-aircraft/96497.article>.
- [5] Trevithick, J., “Here Are The Pentagon’s “Tough Choice” Cuts To Airpower As Part Of Its 2021 Budget,” , Feb 2020. URL <https://www.thedrive.com/the-war-zone/32147/here-are-the-pentagons-tough-choice-cuts-to-airpower-as-part-of-its-2021-budget>.
- [6] “MIL-HDBK-516C: Airworthiness Certification Criteria,” 2014. URL <https://daytonaero.com/wp-content/uploads/MIL-HDBK-516C-from-ASSIST.pdf>.
- [7] Jackson, P., Peacock, L. T., Munson, K., and Taylor, J. W. R., *Jane's all the world's aircraft, 1996-97*, Jane's Information Group, 1996.
- [8] Jackson, P. A., *Jane's all the world's aircraft 2010-2011*, IHS Jane's, 2010.
- [9] Munson, K., Taylor, J. W. R., and Taylor, M. J. H., *Jane's all the world's aircraft 1989-90*, Jane's Information Group, 1989.
- [10] Raymer, D. P., *Aircraft design: a conceptual approach*, AIAA education series, American Institute of Aeronautics and Astronautics, 1989.
- [11] Roskam, J., *Airplane design*, DAR Corporation, 1986.
- [12] Feagin, R. C., and Morrison, W. D., “Delta method, an empirical drag buildup technique,” 1978.
- [13] Michelin, “Aircraft tire: Engineering Data,” , 2021. URL https://www.jupiter.co.jp/pdf/michelin_aircraft.pdf.
- [14] Currey, N. S., *Aircraft Landing Gear: Principles and Practices*, AIAA, 1988.
- [15] “COCKPIT 4000, A modular, integrated glass cockpit for military trainers and light attack armed reconnaissance,” , ???? URL <https://cmcelectronics.ca/productsservices/cockpitsystemsintegration/cockpit4000.aspx>.
- [16] Meier, N., “Military Turbojet/Turbofan Specifications,” , 2005. URL <http://www.jet-engine.net/miltfspec.html>.
- [17] Nicolai, L., *Fundamentals of aircraft and airship design*, American Institute of Aeronautics and Astronautics, Reston, Va, 2010.
- [18] J., R., and E., C.-T., *Airplane aerodynamics and performance*, DARcorporation, 1997.
- [19] “Military Specification: Airplane Strength General Specification For MIL-A-8860B,” 1987.
- [20] “Military Specification: Airplane Strength and Rigidity Flight Loads MIL-A-8861B,” 1986.

- [21] Neufel, W. M., J., and D., C., *Technology and the Air Force: A Retrospective Assessment*, Air Force History and Museums Program, 1997.
- [22] Nordlund, R., “Energy-Maneuverability (E-M) Plot,” , 2021. URL <https://www.mathworks.com/matlabcentral/fileexchange/42632-energy-maneuverability-e-m-plot>.
- [23] Howe, D., *Aircraft Loading and Structural Layout*, The Aerospace Series, Professional Engineering Publishing, U.K., 2004.
- [24] “MatWeb Material Property Data, Overview of materials for 6000 Series Aluminum Alloy,” , 1996. URL <http://www.matweb.com/search/DataSheet.aspx?MatGUID=26d19f2d20654a489aefc0d9c247cebf>.
- [25] “MatWeb Material Property Data,” , 1996. URL <http://www.matweb.com/search/DataSheet.aspx?MatGUID=ab9706916818406b80c22b7f39db0c78>.
- [26] “Alloy 7068, A New Higher Strength, Light Weight Aluminum Replacement for Alloys 7075, 7050, 7049,” , 2016. URL https://online.kaiseraluminum.com/depot/PublicProductInformation/Document/1033/Kaiser_Aluminum_Alloy_7068_Brochure.pdf/.
- [27] “F/A-18 and E/A-18 Fleet Physiological Episodes,” , September 2017. URL [https://www.secnav.navy.mil/foia/readingroom/HotTopics/T-45%20Aircraft%20Goshawk%20PE%20Report/CRT%20PE%20Report%20%20\(Redacted\).pdf](https://www.secnav.navy.mil/foia/readingroom/HotTopics/T-45%20Aircraft%20Goshawk%20PE%20Report/CRT%20PE%20Report%20%20(Redacted).pdf).
- [28] Sutherland, J., “Fly-By-Wire Flight Control Systems,” Air Force Flight Dynamics Laboratory, 1968. URL <https://apps.dtic.mil/dtic/tr/fulltext/u2/679158.pdf>.
- [29] Fielding, C., “The design of fly-by-wire flight control systems,” *The Aeronautical Journal*, Vol. 105, No. 1051, 2001, p. 543–549. <https://doi.org/10.1017/S0001924000018005>.
- [30] Langer, D., Rauch, J., and Rößler, M., “Fly-by-wire systems for military high performance aircraft,” *Real-time systems engineering and applications*, 1992, pp. 369–395.
- [31] Seabridge, A. G., and Moir, I., *Design and development of aircraft systems*, second edition ed., Aerospace Series, Wiley, 2013.
- [32] Collinson, R., “Fly-by-wire flight control,” *Computing Control Engineering Journal*, Vol. 10, No. 4, 1999, p. 141–152. <https://doi.org/10.1049/cce:19990403>.
- [33] Moir, I., and Seabridge, A. G., *Aircraft systems: mechanical, electrical, and avionics subsystems integration*, 3rd ed., Aerospace series, Wiley, 2008.
- [34] Goraj, Z., “An overview of the deicing and anti-icing technologies with prospects for the future,” *24th international congress of the aeronautical sciences*, Vol. 29, 2004.
- [35] Moir, I., Seabridge, A. G., and Jukes, M., *Military avionics systems*, AIAA education series, John Wiley Sons, 2006.

- [36] Magazine, A. F., “Gallery of USAF Weapons,” 2013. URL <https://www.airforcemag.com/PDF/MagazineArchive/Magazine%20Documents/2013/May%202013/0513weapons.pdf>.
- [37] Dyanamics, G., “Hydra-70 Rocket Systems,” , 2020. URL <https://www.gd-ots.com/missiles-and-rockets/hydra-70-rocket-systems/>.
- [38] Andreas, P., “Raytheon AGM-65 Maverick,” , 2005. URL <https://www.designation-systems.net/dusrm/m-65.html>.
- [39] Advantage, M., “AGM-114 Hellfire,” , 2021. URL <https://www.military.com/equipment/agm-114-hellfire>.
- [40] Raytheon, “AIM-9X Sidewinder Missile | Raytheon Missiles Defense,” , 2021. URL <https://www.raytheonmissilesanddefense.com/capabilities/products/aim-9x-sidewinder-missile>.
- [41] Raytheon, “Home | Raytheon Missiles Defense,” , 2021. URL <https://www.raytheonmissilesanddefense.com/>.
- [42] Dynamics, G., “MK-80 General Purpose Bomb Bodies,” , 2021. URL <https://www.gd-ots.com/mk-80-series-bomb-hardware/>.
- [43] Aerospace, M., “CRV7 Rocket Weapon System,” , 2021. URL <https://magellan.aero/product/rockets/crv-7/>.
- [44] Robert, S., “Aircraft Equipment,” , Jan 2021. URL <https://fas.org/man/dod-101/sys/ac/equip/index.html>.
- [45] Aviation, D., “Dassault Aviation, a major player to aeronautics,” , 2021. URL <https://www.dassault-aviation.com/en/>.
- [46] Dynamics, G., “Aircraft Guns and Gun Systems - 20-30mm Gatling Gun Systems,” , 2021. URL <https://www.gd-ots.com/armaments/aircraft-guns-gun-systems/>.
- [47] Nexter, “OUR PRODUCTS | Nexter,” , 2021. URL <https://www.nexter-group.fr/en/nos-produits>.
- [48] Defence, R., “Rheinmetall Defence - Medium Calibre Cannons,” , 2021. URL https://www.rheinmetall-defence.com/en/rheinmetall_defence/systems_and_products/weapons_and_ammunition/direct_fire/medium_calibre/index.php.
- [49] Boeing, “Boeing: fa-18-super-hornet,” , 2021. URL <https://www.boeing.com/defense/fa-18-super-hornet/>.
- [50] L3Harris, “WESCAM MX-TM-15D, Airborne Targeting and Designating,” , 2021. URL <https://www.l3harris.com/all-capabilities/wescam-mx-15d-airborne-targeting-and-designating>.
- [51] Kelly, L. C., “Low-Emissivity Topcoats for the Reduction of Thermal Infrared Emissions from Military Planforms,” , ????. URL <https://www.paint.org/coatings-tech-magazine/articles/low-emissivity-topcoats-for-the-reduction-of-thermal-infrared-emissions-from-military-platforms/>.
- [52] Bartlett, D., “THE EFFECTS OF USING NOISE REDUCTION TURBOFAN ENGINE NOZZLE DESIGNS ON A TURBOJET ENGINE,” , 2016. URL <https://opensiuc.lib.siu.edu/cgi/viewcontent.cgi?article=1009&context=jasa>.
- [53] Gawron, T. J. A., Bartosz Bialecki, and Suchocki, T., “Combustion and Emissions Characteristics of the Turbine Engine Fueled with HEFA Blends from Different Feedstocks,” , 2020.